January 2020

Photometric Study Of Two Near-Earth Asteroids In The Sloan Digital Sky Survey Moving Objects Catalog

Christopher James Miko

PHOTOMETRIC STUDY OF TWO NEAR-EARTH ASTEROIDS IN THE SLOAN DIGITAL SKY SURVEY MOVING OBJECTS CATALOG

by

Christopher James Miko
Bachelor of Science, Valparaiso University, 2013

A Thesis
Submitted to the Graduate Faculty

of the

University of North Dakota

in partial fulfillment of the requirements

for the degree of
Master of Science

Grand Forks, North Dakota

August
2020

Name: Christopher J. Miko

Degree: Master of Science

This document, submitted in partial fulfillment of the requirements for the degree from the University of North Dakota, has been read by the Faculty Advisory Committee under whom the work has been done and is hereby approved.

DocuSigned by:
Dr. Ronald Fevig
9560495A5F4E435...
Dr. Ronald Fevig

DocuSigned by:
Dr. Mike Gaffey
B7394TEEE1BB4FD...
Dr. Michael Gaffey

DocuSigned by:
Wayne Barkhouse
2A58DE60820B413...
Dr. Wayne Barkhouse

DocuSigned by:
Dr. Vishnu Reddy
84C3C02DED864F3...
Dr. Vishnu Reddy

This document is being submitted by the appointed advisory committee as having met all the requirements of the School of Graduate Studies at the University of North Dakota and is hereby approved.

DocuSigned by:
Chris Nelson
2E0AF088C733403...
Chris Nelson
Dean of the School of Graduate Studies

7/23/2020
Date

PERMISSION

Title	Photometric Study of Two Near-Earth Asteroids in the Sloan Digital Sky Survey Moving Objects Catalog
Department	Space Studies
Degree	Master of Science

In presenting this thesis in partial fulfillment of the requirements for a graduate degree from the University of North Dakota, I agree that the library of this University shall make it freely available for inspection. I further agree that permission for extensive copying for scholarly purposes may be granted by the professor who supervised my thesis work or, in his absence, by the Chairperson of the department or the dean of the School of Graduate Studies. It is understood that any copying or publication or other use of this thesis or part thereof for financial gain shall not be allowed without my written permission. It is also understood that due recognition shall be given to me and to the University of North Dakota in any scholarly use which may be made of any material in my thesis.

Christopher J. Miko
July 29, 2020

TABLE OF CONTENTS

LIST OF FIGURES

LIST OF TABLES

ACKNOWLEDGEMENTS

I wish to express my sincere appreciation to my wife Julie, the members of my advisory committee, the professors in the Space Studies department, and Tyler Linder, for their support and guidance during my time at the University of North Dakota.

ABSTRACT

Classifying asteroids by color and spectral features is important for understanding their compositions, linkages to meteorite types, and formation and evolution of the Solar System in general. Large data collection efforts such as the Sloan Digital Sky Survey (SDSS) have allowed for more comprehensive studies of the asteroid population. However, the repeatability and therefore reliability of such observations comes into question, especially as Szabo et al. (2004) and Carvano et al. (2010) reported sizable fractions of asteroids observed by SDSS exhibiting taxonomic variability.

This research studied two near-Earth asteroids (NEAs) with just one observation each by SDSS: 2059 Baboquivari and 96744 (1999 OW3). Observations using the 1 m Yale/SMARTS telescope at Cerro-Tololo Inter-American Observatory (CTIO) were conducted in order to investigate whether g, r, i, and z spectrophotometry was consistent with spectrophotometry by SDSS.

2059 Baboquivari's root mean square z filter and z – i reflectance values did not show a statistically significant difference compared to those values from its SDSS observation. However, individual measurements of z filter and z – i reflectance values compared to those values from its SDSS observation varied up to the 3.8σ level, demonstrating a large dispersion in these z filter and z – i reflectance values. Using photometric spectra from these observations, 2059 Baboquivari could be classified as an S-/Q-type, C-complex, or P-/D-type asteroid. A rotational period could not be determined from the observations. However, 2059 Baboquivari's light curve appeared flat across observation runs, suggesting z filter variability is not due to

rotational effects. Comparing the brightness of bright stars not used in the calibration process during observations eliminated changing sky conditions as a cause of 2059 Baboquivari's photometric variability. A test of the Kron algorithm used for photometry eliminated the algorithm's significant contribution to observed z filter variability, which gives evidence that this variability is not due to the data analysis process. 2059 Baboquivari did not exhibit significant phase reddening of its i – g slope between phase angles of ~22 and ~45 – 50 degrees, but z – i 1 μm band depth generally decreased between phase angles of ~22 to ~45 – 50 degrees.

It was found that 96744 (1999 OW3) likely has a rotational period of ~2 hours or a multiple of ~2 hours. Observations in g, r, i, and z filters showed a repeating correlation between i – g spectral slope, z – i band depth, and C (clear) filter magnitude variation. This suggests that the composition of 96744 may vary across its surface. There were no clear relationships between spectral slope, band depth, and phase angle. However, i – g values showed a steeper visible spectral slope and z – i values showed a shallower 1 μm band depth for 8 Jan 2020 observations compared to those for 10 and 11 Jan 2020 observations.

In conclusion, although significant advances in the characterization of 2059 Baboquivari and 96744 (1999 OW3) were achieved, further study is needed to more precisely determine the properties of these two near-Earth asteroids.

CHAPTER I

INTRODUCTION

Solar System small bodies (SSSBs) are remnants of Solar System formation. They are useful to study for multiple reasons: they yield information on conditions and processes of Solar System formation and evolution, act as tracer particles of planetary migration and dynamics, may contain water and organic compounds, are viable targets for space resource utilization, and underscore the need for planetary defense capabilities. SSSBs largely reside in four stable reservoirs: the Main Belt, Kuiper Belt, Oort Cloud, and Trojans. SSSBs also reside in unstable and dynamically-evolving orbits. Comets and near-Earth objects (NEOs, which include both near-Earth comets (NECs) and near-Earth asteroids (NEAs)) are such members and are known to be destroyed on astronomically short timescales. Thus, they require resupply from one or more stable source regions, which is accomplished by both gravitational and non-gravitational forces (Bottke et al., 2002; DeMeo & Binzel, 2008).

Numerous data-collection efforts have been undertaken in order to study SSSBs. Although not its primary purpose, the Sloan Digital Sky Survey (SDSS) is one of them. SDSS began operating in 2000 utilizing the Apache Point Observatory 2.5 m telescope, taking photometric and spectral images of the northern sky. Photometric observations used u, g, r, i, and z filters with central wavelengths 0.3551, 0.4686, 0.6165, 0.7481, and 0.8931 μm, respectively (Ivezic et al., 2001). The Moving Objects Catalog (MOC) was created to aggregate photometric observations of known moving objects as well as undiscovered moving objects that were observed by SDSS. The fourth release – MOC4 – identified 471,569 moving objects. 220,101 observations were linked to 104,449 known asteroids, with many asteroids observed multiple times (Carry et al., 2016). Out of the observations, 353 of those corresponded to 228

NEOs. Given the large dataset comprising the MOC, the repeatability and thus reliability of these observations comes under scrutiny.

Szabo et al. (2004) utilized the earlier MOC3 and reported that asteroids displayed photometric variability between observations, but found no correlation between color variation and: diameter, absolute magnitude, taxonomy, family, velocity, apparent brightness, angle of opposition, and non-simultaneous observations. This suggests photometric variation is a manifestation of an inherent property for some asteroids. Carvano et al. (2010) developed a spectrophotometry-based taxonomic classification system using the MOC4 dataset (the subscript "p" denoted that the taxonomy was spectrophotometry-based, for example S_p, C_p, etc.). They found that 14,962 of 22,019 asteroids (67.9%) observed multiple times displayed taxonomic variations between observations. Most asteroids displaying variability exhibit it between similar taxonomic classes, but some show variability between dissimilar taxonomies.

Carvano and Davalos (2015) found a statistically significant correlation in which spectral slope depends on phase angle of observation for 75.6% of observations in the MOC4. 55.4% displayed a positive correlation and 20.2% displayed a negative correlation between slope and phase angle. This can affect the resulting taxonomic classification; thus, taxonomic variation is likely due to phase angle for many asteroids in the MOC4.

Rotational heterogeneities may also affect asteroid taxonomy. For example, Linder (2017) studied the asteroid 2453 Wabash, which in Carvano et al. (2010) displayed taxonomic variation between two dissimilar taxonomies: S_p and C_p. Although he found no correlation between spectral slope and phase angle, he found a possible correlation between 1 μm band depth and phase angle. He also obtained observations along Wabash's rotation period, but

differential photometry showed that a rotational cause for Wabash's taxonomic variation is not plausible.

From all these studies, it is concluded that repeated photometric observations of asteroids in the MOC4 often are not consistent with each other, and reasons for the variability are not yet fully known. It is also unknown if consistency and repeatability of SDSS observations vary between Main Belt asteroids and NEOs. NEOs are typically observed at higher phase angles, exhibit higher spectral slopes, and move at faster velocities than Main Belt asteroids (Luu & Jewitt, 1990; Sanchez et al., 2012).

Asteroids 2059 Baboquivari and 96744 (1999 OW3) are two such NEAs in the MOC4 that were observable from Cerro-Tololo Inter-American Observatory (CTIO) from October 2019 through February 2020. Both have just one observation each in the MOC4, and both display low reflectance in the z filter, indicating a possible 1 μm absorption feature. Other physical data available for these objects are their absolute magnitudes: 2059 Baboquivari at H = 16.0 and 96744 (1999 OW3) at H = 14.7, and 96744 (1999 OW3)'s taxonomy (V-type) from an analysis of MOC4 data (Carry et al., 2016).

This research will study the repeatability of photometry of these two NEAs found in the MOC4 by obtaining repeated, independent photometric observations of 2059 Baboquivari and 96744 (1999 OW3) and determining their consistency or inconsistency with observations found in the MOC4. If photometric data are found to be inconsistent with those in the MOC4 and/or exhibit photometric variability, attempts will be made to explain the inconsistencies and/or variability. To that end, rotational light curves of these two NEAs will be constructed to examine if their photometry varies with respect to rotation phase. Their spectrophotometric slopes and 1 μm band depths will also be compared with respect to phase angle of observation.

If this study discovers and explains asteroid photometric variability sufficiently, these results may aid in explaining why asteroid observations in the MOC4 exhibit such large photometric variability, and may have implications for observational studies of near-Earth asteroids.

CHAPTER II

PURPOSE

This study investigates whether SDSS observations of near-Earth asteroids are consistently repeatable, and thus if the MOC4 is a reliable source for near-Earth asteroid photometry. Two near-Earth asteroids (NEAs): 2059 Baboquivari and 96744 (1999 OW3), will be studied by performing repeated photometric observations in g, r, i, z, and C (clear) filters, performing photometry to determine absolute magnitudes in each filter, then converting photometry into normalized photometric spectra, thus attempting to replicate the data found in SDSS MOC4. These results will be compared to photometric data in the MOC4. The consistency or inconsistency between these observations and MOC4 data for these NEAs will either lend or retract support for SDSS being a reliable source of asteroid photometry. If photometric variability is discovered, attempts will be made to explain the reasons for variability. To that end, an attempt will be made to determine rotational light curves of 2059 Baboquivari and 96744 (1999 OW3) in order to examine if these NEAs' photometry changes with respect to their rotation. If this study discovers and explains asteroid photometric variations sufficiently, these results may aid in explaining why some asteroid observations in the MOC4 exhibit such large photometric variability.

CHAPTER III

STATEMENT OF THE PROBLEM

Is the photometry found in the SDSS MOC4 database for 2059 Baboquivari and 96744 (1999 OW3) consistently repeatable? If not repeatable, what are the reason(s) for their photometric variability?

CHAPTER IV

METHOD

Target Selection:

Since the SDSS MOC4 contains 220,101 observations linked to 104,449 known asteroids, and among those are 353 observations of 224 near-Earth asteroids, multiple targets should be observable within the timeframe for this thesis. In order to select which asteroids to observe, JPL Horizons was used to determine what asteroids would be observable from September 2019 through February 2020 at Cerro-Tololo Inter-American Observatory (CTIO). Observability criteria are: V magnitude of < 17.5 and less than 2 airmasses when observed. Other considerations include the phase and position of the Moon, whether the asteroid is in the galactic plane, and the velocity of the asteroid. The list of observable asteroids from JPL Horizons was cross-checked with the list of NEAs in the MOC4 and two NEAs were determined to be observable: 2059 Baboquivari and 96744 (1999 OW3).

The orbital elements of 2059 Baboquivari and 96744 (1999 OW3) are shown in Table 1. Also, photometric spectra based on SDSS observations of both asteroids are shown in Figure 1.

Object	Semi-major axis (AU)	Eccentricity	Inclination (degrees)	Perihelion (AU)	Aphelion (AU)	Jovian Tisserand Parameter	NEO Dynamical Class
2059 Baboquivari	2.644	0.531	11.014	1.240	4.048	3.154	Amor
96744 (1999 OW3)	2.092	0.780	34.945	0.460	3.724	3.138	Apollo

Table 1: Table of orbital elements for 2059 Baboquivari and 96744 (1999 OW3).

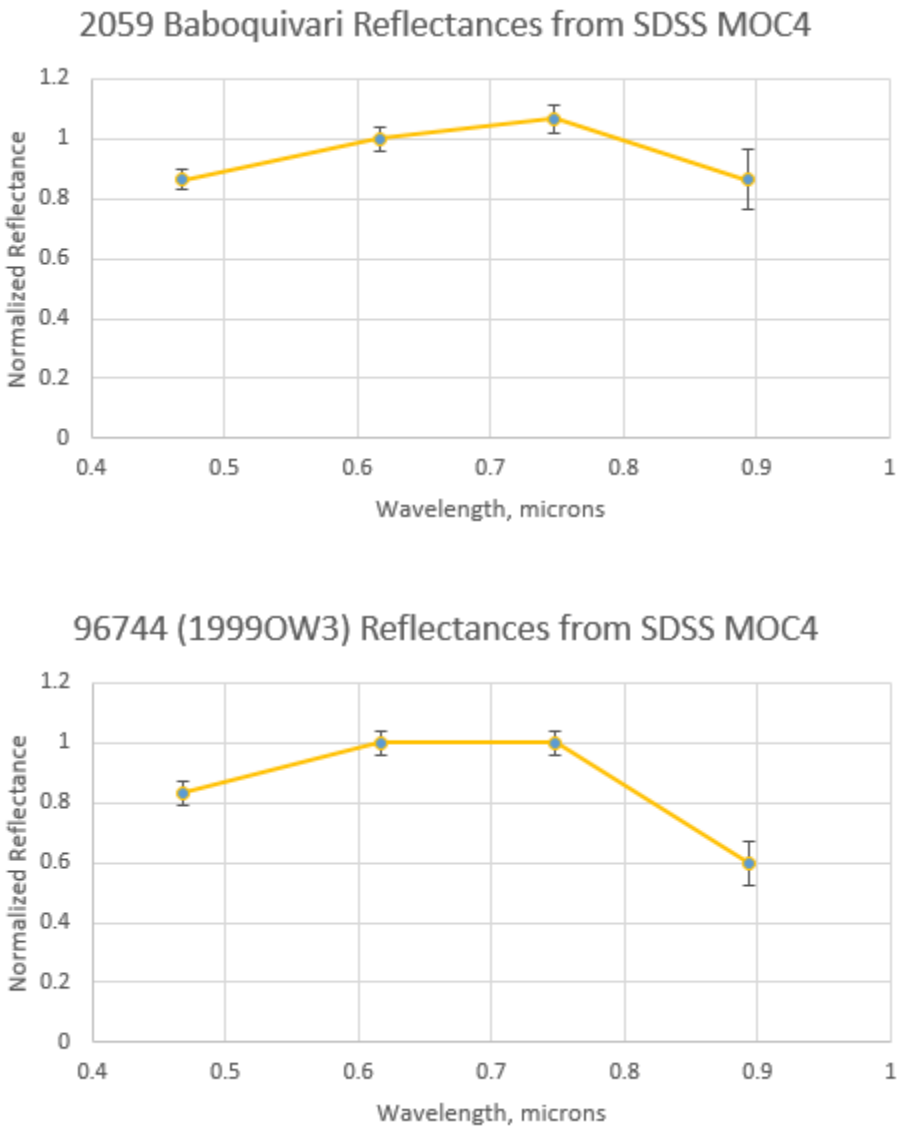

Figure 1: Photometric spectra for 2059 Baboquivari and 96744 (1999 OW3) from their observations in the SDSS MOC4 database.

Observations:

2059 Baboquivari and 96744 (1999 OW3) were observed using the Yale/SMARTS 1.0 m telescope at CTIO in October/November 2019 and January 2020, respectively. This telescope is a f/10.5 reflector. The 2048x2048 CCD used 4x4 binning (which means the CCD operates as

512x512), and at -30 degrees Celsius has dark current of 0.2 electrons/pixel/second. It has a scale of 1.05 arcseconds/pixel, and a 9'x9' field-of-view. Table 2 shows the observational data for each object.

Object	Date (Calendar)	Date (Julian)	Right Ascension	Declination	Sun-Object Distance (AU)	Earth-Object Distance (AU)	Phase Angle (degrees)	Airmass	Apparent V Magnitude
2059 Baboquivari	31 October 2019 / 00:53:12 UT	2458787.53694	22:02:09	-09:34:13	1.260	0.486	46.874	1.092	16.71
2059 Baboquivari	15 November 2019 / 00:42:14 UT	2458802.52933	22:49:46	-11:38:19	1.241	0.512	49.544	1.089	16.86
2059 Baboquivari	18 November 2019 / 00:39:39 UT	2458805.52753	23:00:17	-11:48:09	1.241	0.519	49.811	1.090	16.90
2059 Baboquivari	21 November 2019 / 00:42:28 UT	2458808.52949	23:11:01	-11:52:50	1.240	0.527	49.995	1.091	16.94
96744 (1999 OW3)	8 January 2020 / 4:00:56 UT	2458856.66731	08:07:18	-62:55:21	1.274	0.744	50.326	1.246	16.45
96744 (1999 OW3)	10 January 2020 / 1:25:07 UT	2458858.55911	08:03:50	-64:41:27	1.249	0.724	51.816	1.680	16.39
96744 (1999 OW3)	11 January 2020 / 1:07:46 UT	2458859.54706	08:01:41	-65:39:17	1.236	0.713	52.652	1.660	16.36

Table 2: Observational data for 2059 Baboquivari and 96744 (1999 OW3). All values were calculated at the time the observing runs began.

At the beginning of the night, biases, darks, and flat-field images were taken for data reduction purposes. Once it was time to take science images, the asteroid's RA, Dec, and rate of motion was used to position the telescope so that the observing run could be completed with minimal changes in the background star field. The aim was for ~ 2 – 3 hours of observing time with normal sidereal tracking so as to keep the same star field in the image.

Repeated observations were made in g, r, i, z, and C filters for both objects. In addition, observations of 2059 Baboquivari were obtained in B, V, R, and I. Observations were made in the following order: g, r, i, z, and C (then B, V, R, and I for 2059 Baboquivari only). Exposure times were 60 seconds for all filters except for z and B which both required 150 second exposure times to obtain signal-to-noise ratio (SNR) of > 100 (~10,000 counts from the asteroid). Once these images were obtained, biases, darks, and flats were applied to account for read-out noise, dark current, and pixel-to-pixel differences in sensitivity, respectively. The images are saved as Flexible Image Transport System (FITS) files. Now the images of 2059 Baboquivari and 96744 (1999 OW3) are ready for further analysis.

CHAPTER V

BACKGROUND

History of Asteroid Discoveries:

The word asteroid means "star-like." This is because when first discovered, these objects did not appear to be extended objects like planets, but appeared as point sources like stars. However, asteroids were observed to move as planets did. Interestingly, ordinary chondrite meteorites (which are believed to descend from asteroids) have solar abundances of elements, minus volatiles like hydrogen and helium (McSween, 1999).

At the dawn of the 19th Century, the Solar System was assumed to be an orderly place. There was the Sun, the four terrestrial planets, three gas giants Jupiter, Saturn, and Uranus, and a number of large moons. All of these planets had prograde orbits. Comets appeared occasionally and were perceived as distinct from the remainder of the Solar System objects (North, 2008). Furthermore, the planets seemed to follow a pattern with regard to their distances from the Sun. This was known as the Titius-Bode Law. If one follows the equation

$$a = 0.4 + 0.3*2^n$$

the semi-major axes of planets known at the time followed this pattern, with Mercury at $n = -\infty$ Venus at $n = 0$, Earth at $n = 1$, and so forth. When Uranus was discovered in 1781 by William Herschel, its semi-major axis followed the Titius-Bode Law as well (North, 2008), thus adding to the law's credibility. However, there was a gap where $n = 3$, between the orbits of Mars and Jupiter.

The first asteroid discovered – 1 Ceres – was discovered in 1801 by Giuseppe Piazzi at the University of Palermo in Sicily (Serio et al., 2002). Kepler actually in 1596 postulated the presence of a planet in between the orbits of Mars and Jupiter simply because he believed too

large a gap existed (North, 2008). This was exactly where 1 Ceres was discovered by Piazzi. The Titius-Bode Law's validity was reinforced by discoveries of numerous other asteroids with semi-major axes similar to 1 Ceres, but was eventually discredited when Neptune was discovered in 1846, and now the Titius-Bode Law appears to merely be a coincidence. With Neptune's discovery, the perceived order of the Solar System was challenged.

In 1802, Heinrich Olbers discovered 2 Pallas, and by 1807, 3 Juno and 4 Vesta had been discovered as well. These objects were regarded as planets despite William Herschel suggesting they be placed into a distinct category. In 1845, 5 Astraea was discovered, and more were soon found after that. Asteroid discovery proceeded slowly during this era but some astronomers discovered multiple asteroids. For example, Hermann Goldschmitt was credited for discovering 14 asteroids during the mid-1800s – a very large number of discoveries in that era (J.C., 1867). Eventually these objects were dropped from the list of planets and re-classified as asteroids. Their similar orbits soon led to the term *asteroid belt*. By 1868, 100 asteroids had been discovered (Moore & Rees, 2011). Originally, scientists and astronomers thought that asteroids could be fragments of a larger planet that had been destroyed. However, that hypothesis fell out of favor when the combined mass of the asteroid belt was realized to be only ~4% of the Moon. The compositional gradient within the Main Belt, discovered later, added more certainty that the asteroids never existed as one cohesive planet. Later, the discovery of differing isotopic ratios almost certainly discounted the "destroyed planet" hypothesis (McSween, 1999).

Originally, astronomers thought asteroids were confined to the asteroid belt between the orbits of Mars and Jupiter. However, this was found to not be the case. In 1898, 433 Eros was discovered. This was a novel discovery because 433 Eros had a perihelion interior to Mars' orbit, and thus was the first near-Earth asteroid (NEA, an asteroid with perihelion < 1.3 AU)

discovered. Also surprisingly, 624 Hektor was discovered in 1907 in the same orbit as Jupiter but shifted 60 degrees ahead of it. This was the first Trojan asteroid discovered (Beatty, Petersen, & Chaikin, 1999). In 1932, 1862 Apollo was discovered, having a perihelion interior to Earth. This was the first Apollo asteroid found – another class of NEA (Beatty, Petersen, & Chaikin, 1999).

During this time, asteroid discoveries accelerated, primarily due to the rise of photographic plates. By 1921, 1,000 asteroids had been discovered, 10,000 by 1981, and 100,000 by 2000 (Moore & Rees, 2011). Today, over 800,000 asteroids have been discovered, most now by automated surveys.

During the late 20th and early 21st Centuries, asteroids were discovered in increasingly odd orbits. The first Aten asteroid, 2062 Aten (also a NEA) was discovered in 1976. This is an asteroid with a semi-major axis less than 1 AU but an aphelion greater than Earth's perihelion (0.983 AU). Trojan asteroids co-orbital with Mars, Neptune, Earth, and Uranus were also discovered (Beatty, Petersen, & Chaikin, 1999). The first asteroid with an orbit completely interior to Earth, 163693 Atira, was confirmed in 2003. These are known as Atira or Apohele asteroids; some prefer to refer to them as interior-Earth objects (IEOs) (Bottke et al., 2002; Greenstreet et al., 2012).

History of Comet and other Small Solar System Body Discoveries:

An overview of small Solar System body (hereafter SSSB) discoveries would not be complete without also discussing comets. A comet is a SSSB that while near perihelion warms and begins outgassing volatiles, creating a visible coma and often a tail (Beatty, Petersen, &

Chaikin, 1999). Asteroids, discussed above, are also SSSBs; however, they do not exhibit a coma or tail as comets do.

Unlike asteroids, comets have been known to mankind since Antiquity. Halley's Comet (1P/Halley) has been known since 240 B.C. (Sagan & Druyen, 1997). Comets were historically seen as omens of death and destruction. Pliny the Elder believed comets were associated with political unrest. Famously, a comet appears in the Bayeux Tapestry depicting the Battle of Hastings in 1066, in which the Norman-French army of William Duke of Normandy defeated the Anglo-Saxon King Harold (Sagan & Druyen, 1997).

The true nature of comets was not known until the 16th Century, when Tycho Brahe measured the parallax of the Great Comet of 1577 and determined it must be at least four times more distant from the Earth to the Moon (North, 2008). Before then, many thinkers including Aristotle, believed comets were atmospheric phenomena or at least existed in sub-lunar space (North, 2008). Isaac Newton in his *Principia Mathematica* of 1687 showed that orbits followed conic sections, and comets plausibly followed parabolic or near-parabolic orbits. Edmund Halley used Newton's work and in 1705 found that the comets of 1531, 1607, and 1682 had similar orbital elements. He predicted that this comet would reappear in 1758 – 1759, and it did (North, 2008). This comet is now known as Halley's Comet (1P/Halley).

During the 19th Century, comets were discovered at a slow but steady rate. By the mid-20th Century, enough comets had been discovered for scientists to notice there were distinct populations among them: long-period comets (LPCs) which have periods of greater than 200 years and nearly-isotropic inclination distributions, Halley-type comets (HTCs), which have periods of ~20 – 200 years and moderate inclination distributions, and Jupiter-family comets (JFCs) which have periods of less than 20 years and typically low inclination, prograde orbits

(Bottke et al., 2002). These different populations hinted at different origins and different evolutionary pathways for comets. Edgeworth (1949), Oort (1950), and Kuiper (1951) hypothesized the existence of cometary reservoirs beyond Neptune's orbit. In particular, Oort hypothesized that LPCs originated from a spherical cloud of objects 5,000 – 150,000 AU from the Sun (Oort, 1950). These reservoirs today are known as the Kuiper Belt and Oort Cloud, and comets are believed to originate from these reservoirs. Comets are typically discovered at a slower rate than asteroids. Currently there are ~5,300 known comets.

At first glance, asteroids and comets appear to be two distinct and separate types of objects. This is not the case, however. There are objects that display both cometary and asteroidal properties: either dynamical, physical, or both. An example of such an object is 4015 Wilson-Harrington. It was discovered as Comet 1949 III in 1949 (and later named 107P). Thirty years later, in 1979, an asteroid with very similar orbital elements was discovered and named 1979 VA. However, an examination of older photographic plates in 1992 revealed that it was also the comet 107P (Beatty, Petersen, & Chaikin, 1999). Thus, 4015 Wilson-Harrington/107P and other objects similar to it are dubbed dormant comets. In addition, in 1977 an object was discovered between Saturn and Uranus. The object did not exhibit cometary activity, so it was named 2060 Chiron. By 1991, though, 2060 Chiron began to exhibit a coma and tail as it neared perihelion (Beatty, Petersen, & Chaikin, 1999). It seems that this asteroid had turned into a comet. More of these types of objects were found and were named Centaurs after the half-human/half-horse figure in Greek mythology.

In 1986 Comet Halley passed through the inner Solar System again. Instead of simply observing the comet through telescopes, multiple nations decided to send spacecraft to study Halley more intensely. One of the most striking discoveries was that only a small fraction

(~10%) of Halley's surface was actively sublimating volatiles (Sagan & Druyen, 1997). The rest of the surface looked like a dark asteroid's surface. Later spacecraft to other comets have confirmed this as the norm rather than an exception.

In 1992, David Jewitt and Jane Luu discovered the first Kuiper Belt object: 1992 QB1 (Jewitt & Luu, 1993). Today, over 1,000 KBOs are known, and there are thought to be over 100,000 KBOs over 100 km in diameter (Bottke et al., 2002). In addition, a population of objects in what is known now as the Scattered Disk were discovered, the most massive being dwarf planet Eris (Brown et al., 2005). In fact, Eris' discovery was immediately responsible for the International Astronomical Union's (IAU's) controversial 2006 demotion of Pluto's planethood and establishment of a new class of objects known as *dwarf planet*. In the 1990s and early 2000s, a small fraction of asteroids in the Main Belt were also found to display a coma on occasion. This baffled scientists because most believed all volatile compounds capable of sublimation at that distance from the Sun would have escaped from those asteroids long ago (Hsieh & Jewitt, 2006). However, this does not seem to be the case. There are numerous mechanisms in which an asteroid can plausibly be activated, including recent collisions uncovering volatiles beneath the surface or rotational spin-up due to non-gravitational forces (Jewitt, 2012). This class of objects were named “Main Belt comets” or “active asteroids.” On the subject of asteroid activation, some asteroids that have low perihelia ($q < \sim 0.3$ AU) can also exhibit a coma, perhaps due to thermal fracturing from the Sun's heat or desiccation of hydrated minerals (Jewitt, 2013). 3200 Phaethon may exhibit this behavior, whose orbit aligns with the Geminid meteor stream (Whipple, 1983; Li & Jewitt, 2013). It appears that our Solar System's small bodies are more diverse than we ever could have imagined.

So, how do all of these classes of objects relate to each other? As mentioned earlier, SSSBs' spectral features give clues as to their compositions, and their compositions are dependent upon where they formed in the early Solar System. By understanding where these objects formed, we can understand how they have evolved, both dynamically and physically. Understanding how SSSBs evolve dynamically and physically can tell us how other populations in the Solar System have migrated and evolved, which populations brought water and organics to the early Earth and other terrestrial planets, and perhaps what the Solar System's future holds.

Dynamical Properties of Asteroids:

As more asteroids were discovered, astronomers began organizing and categorizing them in order to observe trends in the population. One way to do this is by their orbital parameters. The three most relevant, especially in this research, for observing trends amongst the asteroid population are semi-major axis, eccentricity, and inclination.

Semi-Major Axis, Inclination, and Eccentricity:

If one observes the plot of numbers of asteroids as a function of semi-major axis (Figure 2), some trends become evident. Most asteroids reside in the $\sim 2 < a < 3.5$ AU region, known as the Main Belt (Pater & Lissauser, 2010). There are also other regions of population density, such as Hungarias at $1.78 \leq a \leq 2$ AU, Cybeles at $3.28 \leq a \leq 3.70$ AU, and Hildas at $3.7 \leq a \leq 4.2$ AU. There are also noticeable gaps in the Main Belt. These were discovered in 1867 by Daniel Kirkwood and were consequently named “Kirkwood Gaps.” The existence of Hungarias, Cybeles, and Hildas, as well as the Kirkwood Gaps, are due to mean-motion resonances with Jupiter. The in-depth properties of resonances are beyond the scope of this background, but

mean-motion resonances are regions in which an object's orbital period is a certain integer ratio with respect to another object's orbit – in this case Jupiter. Some mean-motion resonances may be stabilizing, and some may destabilize orbits. For destabilizing resonances, Jupiter's gravitational influence can increase an asteroid's eccentricity so that it eventually becomes planet-crossing. Next, a close encounter with a planet can thus remove it from the resonance. The 4:1, 3:1, 5:2, 7:3, and 2:1 resonances at 2.06, 2.50, 2.82, 2.95, and 3.27 AU, respectively, form the inner and outer boundaries of the Main Belt and divide it into inner, middle, and outer regions (Bottke et al., 2002; Pater & Lissauser, 2010). How Main Belt asteroids are perturbed by gravitational resonances and other forces will be covered in more detail later. However, due to these resonances, a small population of asteroids with semi-major axes in the region of the inner planets appear. These are the NEAs.

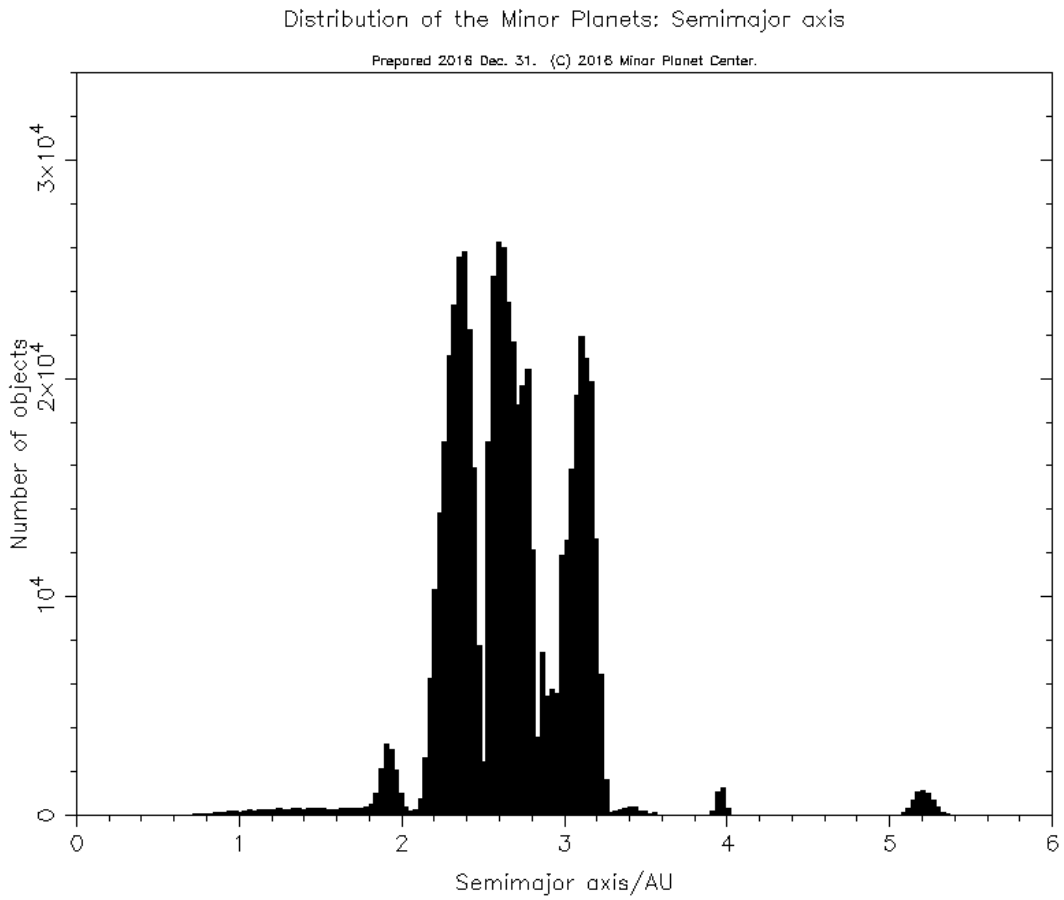

Figure 2: Distribution of the Minor Planets: number vs semi-major axis (IAU-A, 2018).

Orbital inclination shows the angle of an object's orbit with respect to the ecliptic. Most asteroids have low-inclination orbits, and thus remain near the ecliptic throughout their orbits. Some asteroids, however, have higher inclinations, and thus remain either above or below the ecliptic throughout the majority of their orbits. Figures 3 and 4 plot asteroid number vs inclination and also inclination vs semi-major axis. Orbital inclination directly affects which asteroids will be affected by secular resonances, which are explained below.

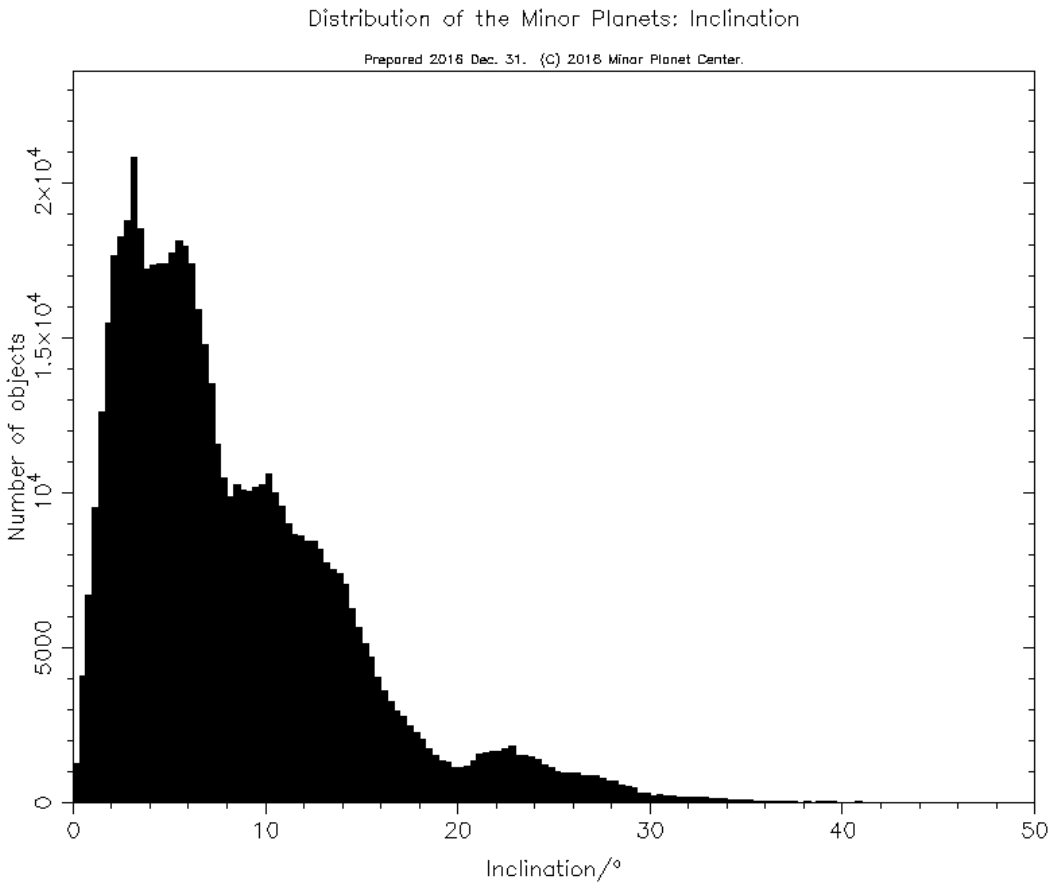

Figure 3: Distribution of the Minor Planets: number vs inclination (IAU-C, 2018).

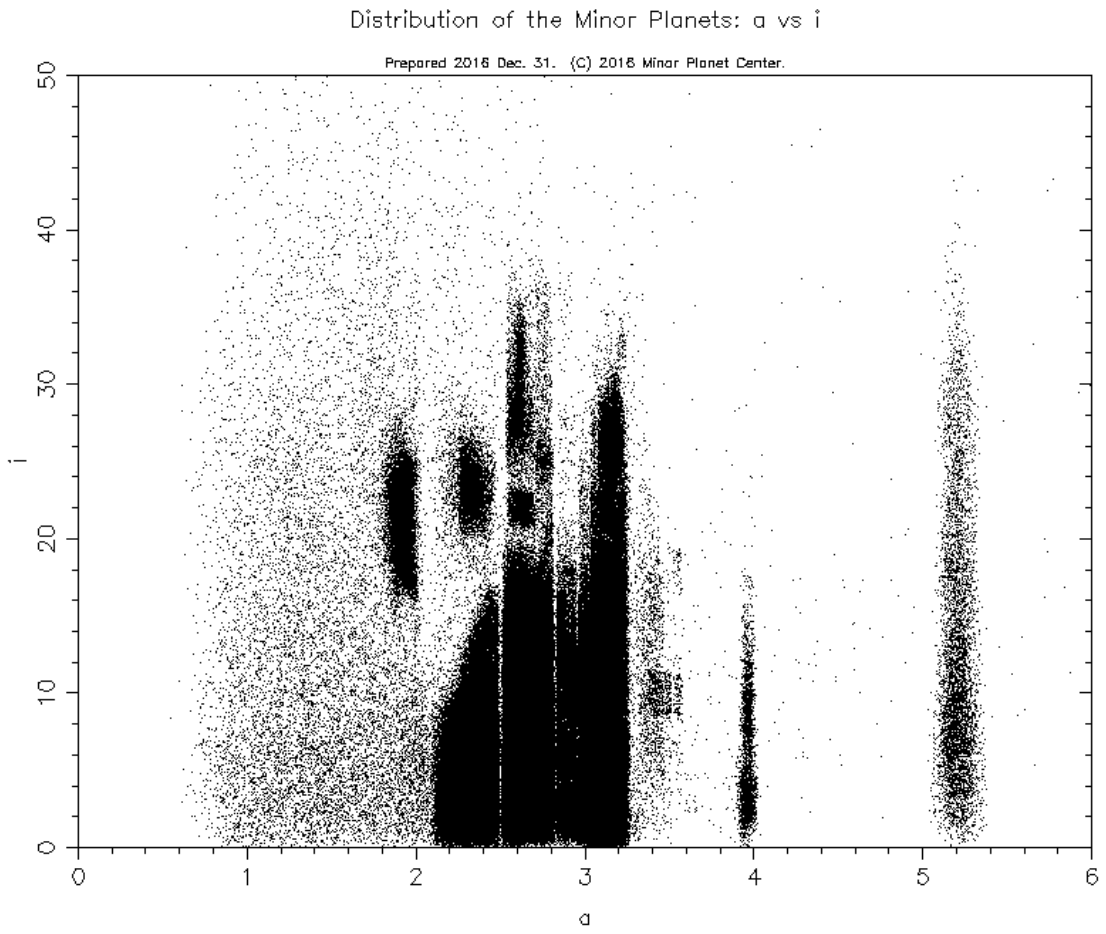

Figure 4: Distribution of the Minor Planets: inclination vs semi-major axis (IAU-F, 2018).

Asteroids can also be arranged by eccentricity. Similar to inclination, most asteroids in the inner Solar System have low-eccentricity orbits. In fact, over 90% of them have eccentricities below 0.3, with average eccentricity at ~0.14 (Pater & Lissauser, 2010). The median value of asteroid eccentricity is ~0.125, and thus that asteroid's distance from the Sun will vary by ~25% over the course of its orbit. These are shown graphically in Figure 5.

In addition to mean-motion resonances being able to increase eccentricity, so can secular resonances. Secular resonances are where the orbital precession of an object is synchronized with that of another object (Pater & Lissauser, 2010). The most significant secular resonance is

υ_6 the secular resonance with Saturn. Secular resonances can increase an asteroid's eccentricity as well, causing an asteroid to potentially become planet-crossing. This is shown to be a possible dynamical pathway for Main Belt asteroids to become Mars Crossers and NEAs (Morbidelli et al., 1993). Figure 6 shows asteroids plotted as eccentricity vs semi-major axis, clearly showing both the low- and high-eccentricity populations.

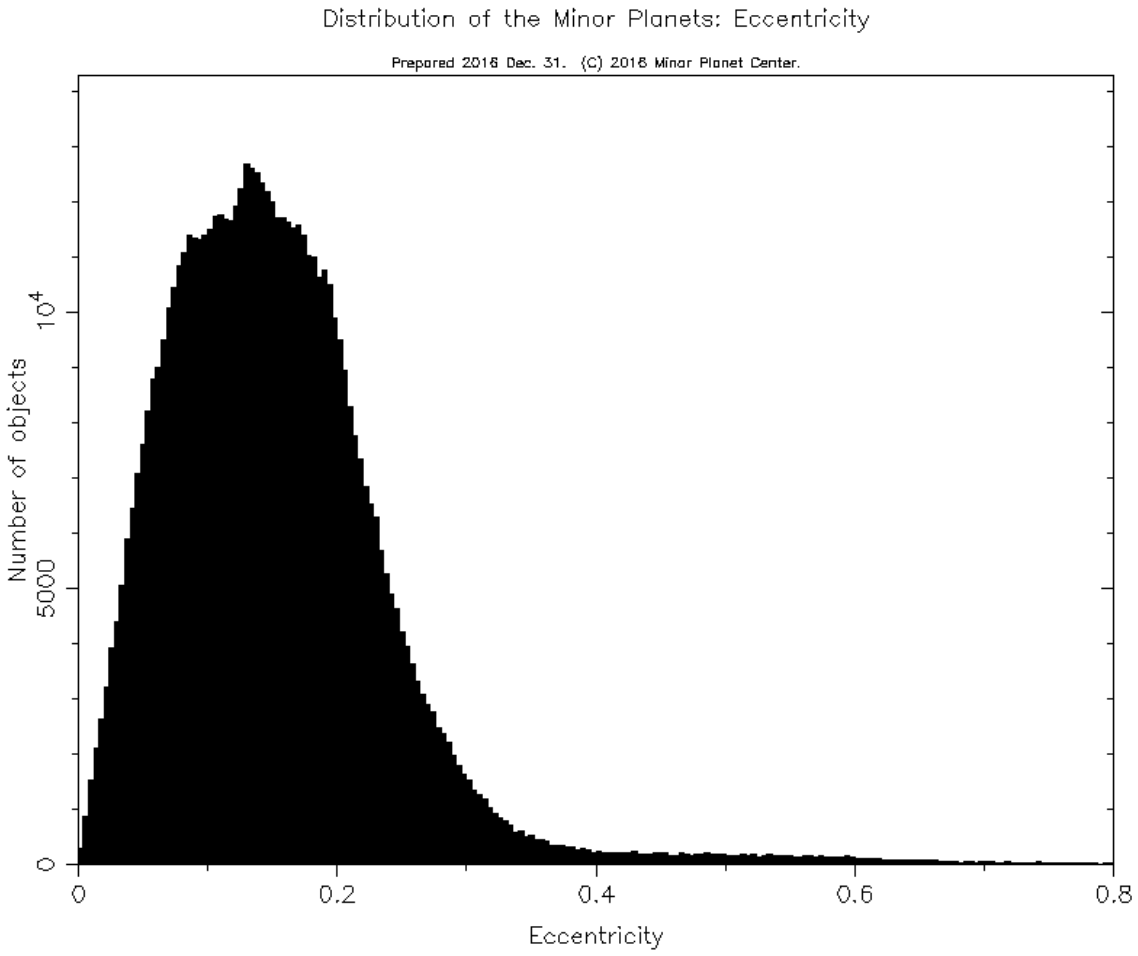

Figure 5: Distribution of the Minor Planets: number vs eccentricity (IAU-B, 2018).

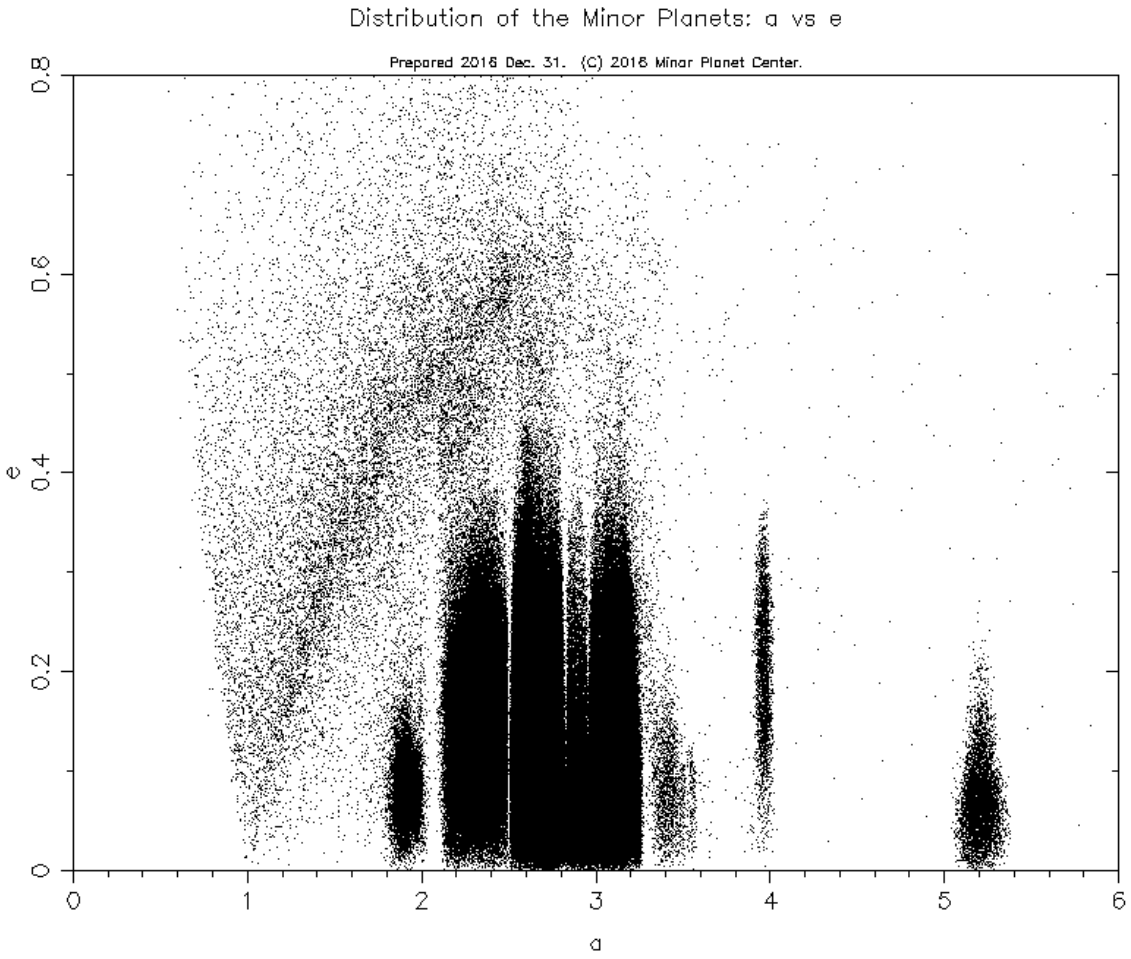

Figure 6: Distribution of the Minor Planets: eccentricity vs semi-major axis (IAU-E, 2016).

Knowing the dynamical properties of asteroids is important because it is the first step in describing these objects, and it informs further sections of this literature review. In fact, Main Belt asteroids follow a rough spectral and compositional gradient. More reflective asteroids with silicate spectral absorption bands are more abundant in the inner Main Belt, that is, interior to ~2.5 AU. Less reflective asteroids with featureless reflectance spectra are more abundant in the central-to-outer Main Belt, beyond ~2.5 AU (Bottke et al., 2002, DeMeo & Carry, 2014). Some of these darker asteroids have neutral-to-blue spectral slopes, while some have redder spectral

slopes, which give clues as to their surface compositions. Asteroids' spectral features and slopes – and hence likely their compositions – are dependent upon where they formed in the Solar System. These will be discussed in greater detail below. What we know about the locations of these small Solar System objects can tell us a great deal about the formation and evolution of our Solar System.

Observing Asteroids:

Like other astronomical phenomena, asteroids are observed using telescopes. Contrary to stars and galaxies, however, asteroids appear to move with respect to background stars and galaxies. Thus, asteroids will be in different positions in the sky from night to night and traditional observing techniques have to be adjusted accordingly.

Near-Earth asteroids (NEAs) typically appear to move on the order of ~2.5 arcseconds/minute, so they will only be in the field-of-view of a telescope for a limited period of time. For example, if a telescope's field-of-view is 9'x9', the maximum amount of time the NEA will be in the field-of-view is approximately 300 minutes, or 5 hours. This is if the asteroid appears to move diagonally across the field-of-view as well. This is rarely the case, however. In practice, one can observe a NEA for ~2 – 3 hours with sidereal tracking until the telescope's position must be adjusted.

During the observing run, airmass will change, and this must be accounted for. Airmass is the relative amount of atmosphere the light must pass through before reaching the telescope. An airmass of 1 means the object is directly overhead. It is preferable to observe objects with an airmass value of less than 1.5. Over the span of days to months, the Sun-asteroid-Earth angle - called phase angle – will change, and this affects the results of measurements taken during the

data analysis process. Phase angle effects will be discussed in detail later. The asteroid may move in front of background stars as well, which makes any type of measurement very difficult. The asteroid's position relative to the Moon will also change, which can affect background counts. The asteroid's position with respect to the galactic plane will also change. Lastly, since the asteroid is moving non-sidereally, it will not appear as a point source in the images. This affects the type of photometry that can be applied to measure the brightness of the asteroid. As can be seen, there are many variables which must be accounted for while observing asteroids.

Before discussing the practice of observing asteroids any further, it is prudent to give a brief introduction to instrumentation and methods used to observe them, measuring the light coming from them, and determining their properties.

Charge-Coupled Devices:

Charge-coupled devices (CCDs) are the primary way in which modern optical astronomers obtain images of astronomical objects. Simply put, a CCD converts incoming light (photons) into an electrical signal which is then converted into an image. The concept of charge-coupling was theorized in 1969 at Bell Labs, and the first CCD based on silicon semiconductors was invented (McLean, 2008). The utility and size of CCDs greatly increased in the 1980s and by the 2000s almost every professional astronomical observatory in the world had a CCD imager. CCDs are indispensable to modern astronomy. Why is this?

CCDs have many advantages over older imaging systems like photomultiplier tubes, photographic plates, and vidicons. First, CCDs are sensitive to light from ~300 – 1,100 nm, making them able to detect light over the entire visible range. CCDs also have high quantum efficiency, meaning they have a high efficiency of converting photons into signal. CCDs also

are small, relatively low power, and linear in their response to light over a wide range of levels (McLean, 2008). How do CCDs work?

At its heart, a CCD is an array of numerous picture elements (pixels), and each pixel can absorb photons and utilize that energy to release an electron within the silicon semiconductor. A CCD's structure consists of metal electrodes on top of the silicon semiconductor slab with a thin silicon oxide depletion layer to act as an insulator. This structure behaves like a metal-oxide semiconductor (MOS) and is capable of storing electrical charge. An electric field is created in the silicon slab by the voltage applied to the metal electrode, so when a photon enters the silicon slab, an electron-hole pair is generated. The hole is driven away from the depletion region, but the electron is attracted to the positively-charged electrode. As more photons interact with the silicon slab, more electrons accumulate on the depletion region, which acts as a potential well or "bucket" to store these photon-generated charges (McLean, 2008). There are only a finite number of electrons that can accumulate in the depletion region due to the voltage used, and this number of electrons is known as the full-well capacity.

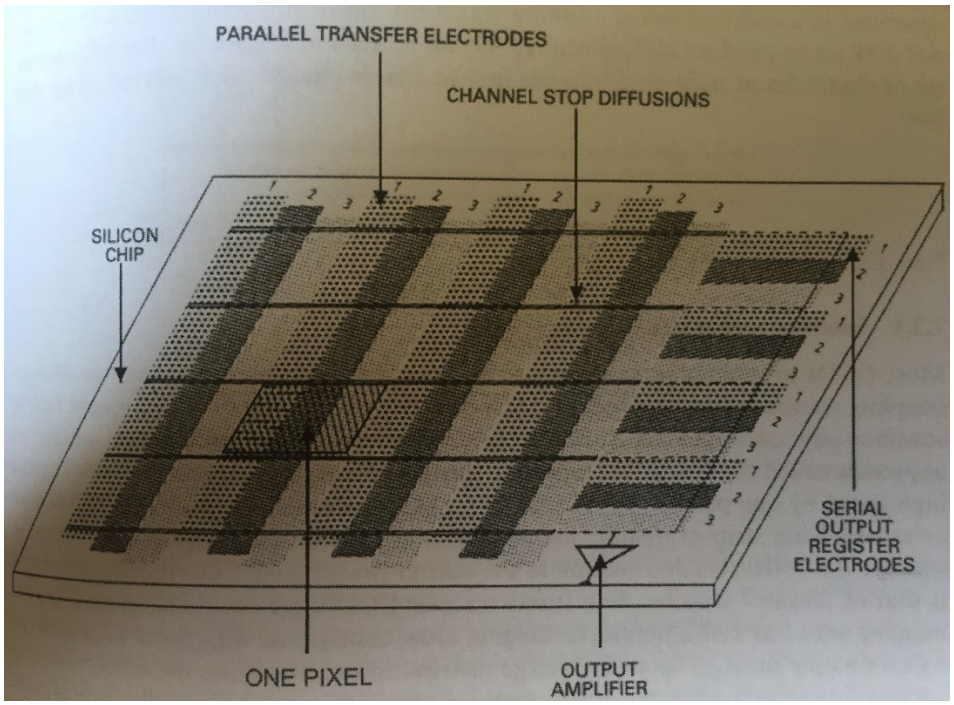

Figure 7: Graphic of CCD (McLean, 2008).

What makes CCDs so useful is how they read out charges. Actually, most CCDs have three strips of electrodes making up one pixel, with one of those strips having a more positive voltage than the other strips. Under this electrode is where electrons accumulate. The others act as walls to the pixel. How charge is read out is called "charge coupling." Voltages are changed on the electrodes in order to transfer the accumulated charges one electrode at a time. Three transfers are necessary in order to move the charges one pixel. The process of manipulating the voltages to shift the charges is called clocking (McLean, 2008).

At the end of the CCD is a special row of pixels called the output register. Charges are transferred vertically along the CCD and into the output register row, then transferred horizontally along the output register row. This charge is then delivered to an output amplifier and converted to a voltage which is then measured and digitized by an analog-to-digital converter (ADC). This happens until all the charges are read out. Most ADCs used today are

16-bit (2^{16}), so the read-out voltage range can be divided into 65,536 parts. Thus the ADC matches the voltage to the nearest value from 0 – 65,535. The resulting image is the two-dimensional graph of these values (McLean, 2008). As a note, the number of electrons needed to change a pixel value by one number is known as the CCD's gain.

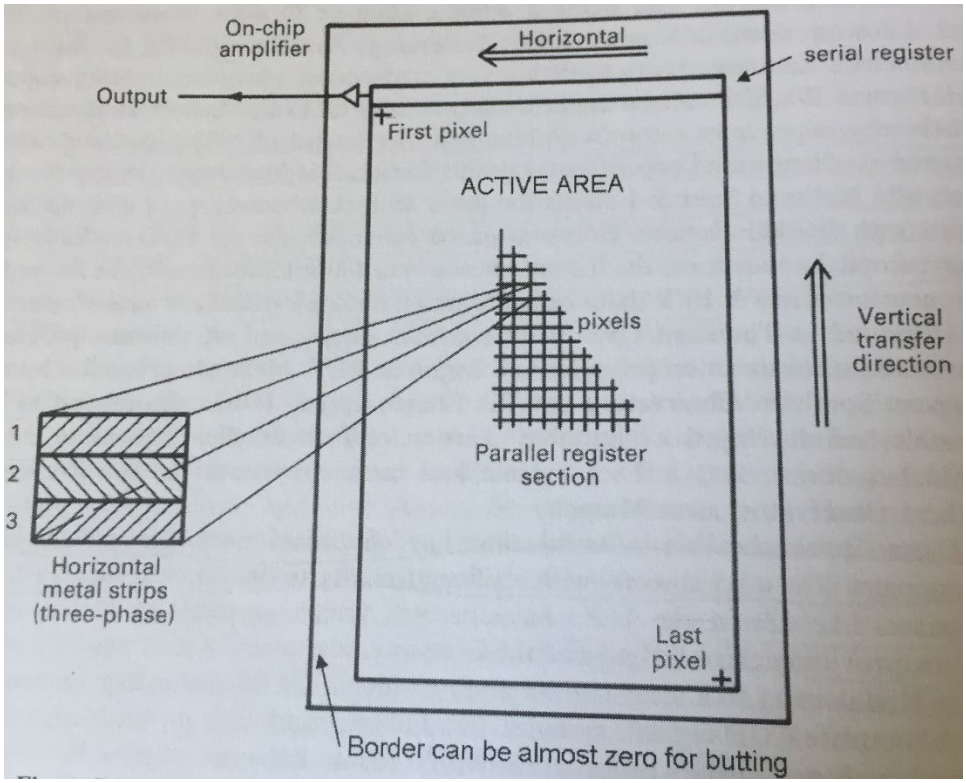

Figure 8: Graphic of CCD read-out process (McLean, 2008).

As revolutionary as CCDs are, they are not perfect. The first is the full-well capacity. If enough photons strike a pixel, there will be a time where no more charge can accumulate. Thus, the CCD will lose linearity. An astronomer must be aware of this limitation. Also, Brownian motion of the atoms in the CCD is large enough to generate a continuous stream of electron-hole pairs, and this is known as dark current. Fortunately, dark current is strongly dependent on

temperature, so decreasing the temperature of the CCD dramatically reduces dark current (McLean, 2008). This must be accounted for in the data reduction process. Not all pixels are equally sensitive, either, and sometimes dust on the CCD blocks some photons. This must be corrected by the data reduction process too by calibrating or "flat-fielding" the CCD. In addition, even if no photons are absorbed by the CCD, there will always be a small positive value for each pixel when read out. This is known as read out noise or the bias level. An exposure of zero time with the shutter closed is used to measure the bias level, and this also must be accounted for in the data reduction process. All in all, dark current, pixel-to-pixel sensitivity, and bias need to be corrected for in the data reduction process and are commonly known as "biases, darks, and flats" (McLean, 2008). Lastly, as mentioned before, although CCDs are sensitive to light across the entire visible wavelength range, there are issues with traditional CCDs absorbing photons shortward of 300 nm and longward of 1,100 nm due to the material properties of silicon and UV atmospheric cutoff.

In conclusion, charge-coupled devices are revolutionary to the science of astronomy and they are today an indispensable part of practically every observatory practicing astronomy at optical wavelengths. Now that this subject has been covered, the techniques of photometry and spectroscopy can be discussed.

Photometry:

Photometry is the science of measuring light from a source. This is usually done over relatively broad wavelength ranges, but some types of photometry do use narrow wavelength range to try to isolate specific spectral features (McLean, 2008). This research uses only broadband photometry, so this section will discuss that practice only.

Overall, the goal of photometry is to obtain accurate values for objects' brightnesses. At times, relative brightness is adequate; this may be relative to other objects in the field of view. Other times, absolute brightness must be determined (McLean, 2008). These two terms are called differential photometry and absolute or calibrated photometry. This research uses both types of methods. In short, though, for the purposes of this research, light from both asteroids and background stars need to be measured. The details of the experimental methods in the research are described in the Methods section; this section serves merely to give an overview.

First, some terms need to be defined. Flux is the power received in W/m^2 by integrating over the intensity over the area of the source. Magnitudes are relative measurements of the flux of a source. The magnitude equation is

$$m = m_0 - 2.5\log(F) + 2.5\log(F_0)$$

where m is the magnitude of the source and m_0 is the magnitude of a reference source. Similarly, F and F_0 are the fluxes of the source and reference source, respectively (McLean, 2008).

In practice, how are these fluxes measured? There are multiple ways, but for this thesis counts from the CCD image of the sources (both asteroids and stars) were used to represent flux and conversion into other physical units was not performed. So, how does one measure counts from a CCD image? As the name implies, they are counted. There are, not surprisingly, many methods to do this. The first is called aperture photometry and it is the simplest. One draws a shape, usually circular, around the source to be measured, determines the number of counts within the circle, then does the same thing for nearby background sky. Thus,

$$\text{Counts(source)} = \text{Counts(total)} - \text{Counts(background)}$$

The important thing to remember about aperture photometry is that the sizes of the apertures used to perform the measurement must be the same. Aperture photometry was used for

some parts of the data analysis of this thesis. Annular photometry is another method and uses concentric circles to obtain counts.

Another photometry method is called profile fitting or point-spread function (PSF) fitting. This method models the source as opposed to summing over the source. Mathematical curves are fitted to the data, for example, a stellar source would be compared to a Gaussian profile

$$I(r) = I(0)\exp(-r^2/2\sigma)$$

Where I(0) is the peak intensity of the source and r is the distance from the center of the source. This method works well for point sources like stars, but since asteroids move at appreciable non-sidereal rates, they often do not appear as point sources in the image. Thus, PSF fitting was not used in this thesis.

Yet another form of photometry uses the Kron first-moment algorithm to construct an elliptical aperture fitted to the object's light distribution (Kron, 1980). An elliptical aperture whose elongation and position angle is defined by the second-order moments of the source's light distribution. The ellipse is scaled to approximately two isophotal radii, and then the first moment is calculated within the aperture using

$$r_1 = \frac{\sum rI(r)}{\sum I(r)}$$

where I(r) is the intensity of the source at a certain distance r away from its center. This algorithm was developed in order to accurately measure the brightness of galaxies, which are non-point source objects. It can be applied to asteroids as well.

Because flux can be measured as counts (see above), after photometric measurements are performed the result is a non-calibrated magnitude known as the instrumental magnitude (Im). This is defined as

$$Im = -2.5\log(Counts(source))$$

Instrumental magnitudes can be used effectively for differential photometry, and some of this research is performed using only instrumental magnitude. However, if one wants the true brightness of an object, calibration must be performed. This is commonly done by calculating the zero point (ZP) for an image. The zero point can be determined by calculating the difference between the instrumental magnitude for a source and its known catalog magnitude. This research measures instrumental magnitudes of multiple stars and compares them to their catalog magnitudes using the equation

$$ZP = m_{catalog} - Im$$

The zero point should be similar for all sources, but it is important to use multiple sources in order to reduce uncertainties.

After this step is complete, the calibrated magnitude of an asteroid can be determined using

$$m_{calibrated} = Im + ZP$$

There are other factors that can be considered in the calibration process, such as extinction through the Earth's atmosphere, but the method above usually works well for low airmasses (McLean, 2008).

Photometry is often performed in different filters. These filters only let light of certain wavelengths through while rejecting other wavelengths. These filters have a sensitivity, central wavelength, and bandpass. Filters are often grouped into systems called photometric systems. Some examples are the original UBV photometric system of Johnson and Morgan, later expanded into UBVRI Kron-Cousins system, and the Sloan u'g'r'i'z' photometric system which uses non-overlapping filters (McLean, 2008). There are many other photometric systems in use today, and they span not only the optical wavelengths region but also the infrared and ultraviolet.

Observing objects in different filters gives an opportunity to study their brightness through varying wavelength regions and thus gives astronomers the ability to determine properties of the object being studied. Below are figures and tables of the Kron-Cousins and Sloan u'g'r'i'z' photometric systems.

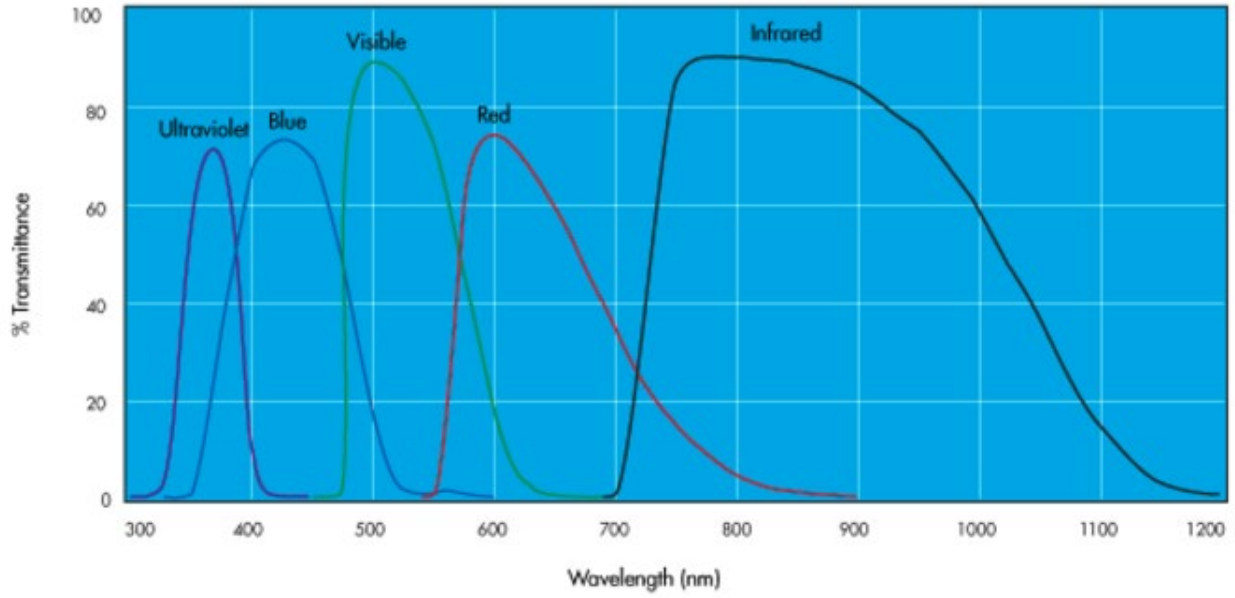

Figure 9: Graphic of UBVRI system. Note that CCDs lose sensitivity longward of 1,100 nm (qd-europe.com).

Filter	Central Wavelength (nm)	Width (nm)
U	360	70
B	440	100
V	550	90
R	650	100
I	800	150

Table 3: Table of UBVRI system (McLean, 2008).

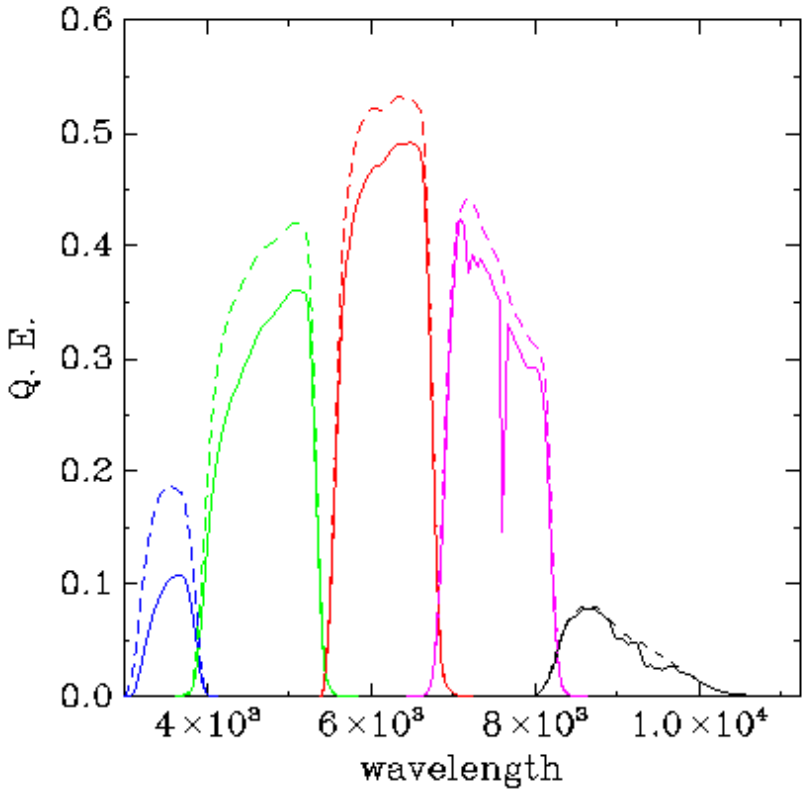

Figure 10: Graphic of u'g'r'i'z' system. Dashed curves are without atmospheric extinction and solid curves take into account atmospheric extinction (classic.sdss.org).

Filter	Central Wavelength (nm)	Width (nm)	Magnitude Limit
u’	355.1	56.0	22.0
g’	468.6	137.7	22.2
r’	616.5	137.1	22.2
i’	748.1	151.0	21.3
z’	893.1	94.0	20.5

Table 4: Table of u’g’r’i’z’ system (McLean, 2008). The limiting magnitudes for each filter correspond to a signal-to-noise ratio of 5, corresponding to a 20% uncertainty in magnitude measurements (Gunn et al., 1998).

Often in photometry the color indices of objects are determined. For example, U – B is the object’s difference in magnitude between the U and B filter. Usually the longer-wavelength filter’s magnitude is subtracted from the shorter-wavelength filter’s magnitude. Thus, if the resulting value is positive (recalling how magnitudes work) the object is said to be redder. If the resulting value is negative, the object is said to be bluer. Below in Figure 11 is a B – V vs V – R graph of asteroid observations from Jewitt (2013).

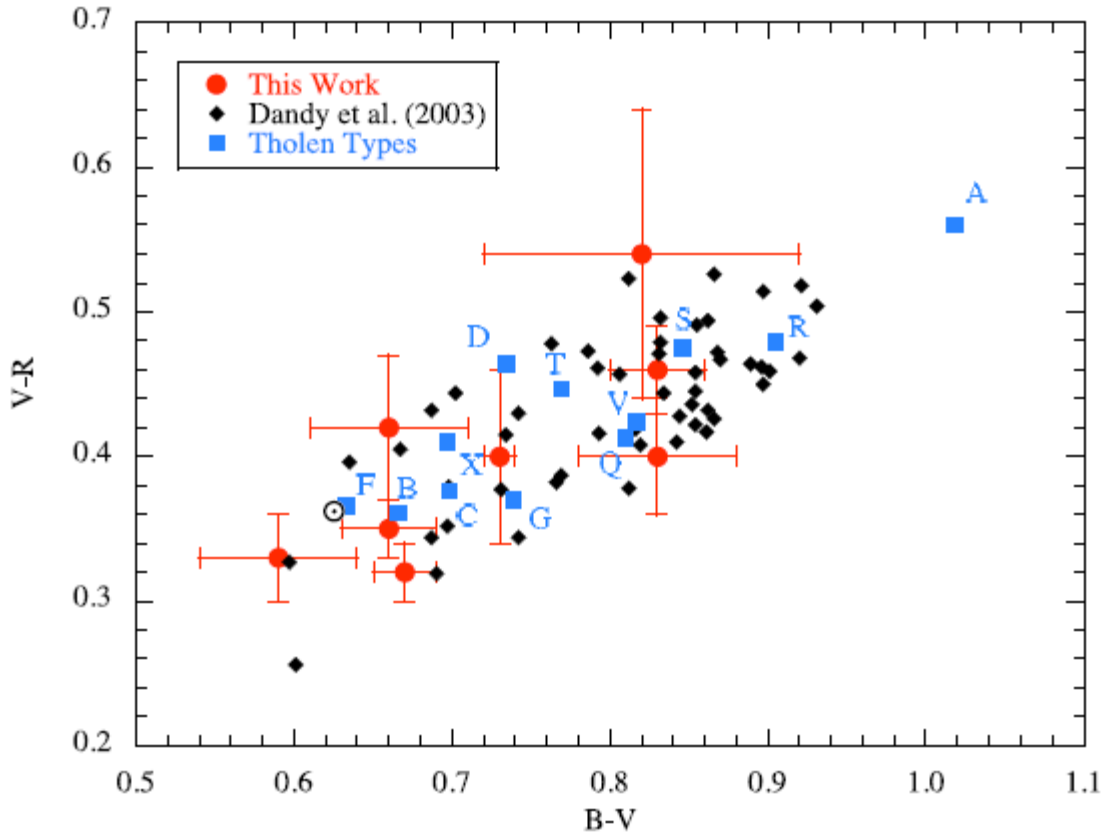

Figure 11: Asteroid color index graph from Jewitt (2013). Also included in this graph are asteroid colors from Dandy et al. (2003).

One last aspect of photometry – one that is relevant for this thesis – is observing with a clear (C) filter or no filter at all. A C filter usually has a short wavelength cutoff to block UV light but no longer wavelength cutoff. Thus, a C filter would allow all light from ~350 – 400 nm (~0.35 – 0.4 µm) until the wavelength cutoff due to properties of the CCD at ~1,100 nm (~1.1 µm). While not useful for determining the colors of an object, observing in a C filter is useful for obtaining high signal-to-noise images of an object, and this is applicable for astrometry or studying rotational characteristics of an object where obtaining the highest signal-to-noise is favorable. This study will use C filter images to build rotational light curves of NEAs.

Spectroscopy:

Spectroscopy is the science of measuring the light from an object as a function of its wavelength. It gives astronomers information on the physical and chemical compositions, temperatures, densities, and velocities of astronomical objects and phenomena (McLean, 2008). Compared to how long the science of astronomy has been performed, spectroscopy is a new scientific tool, appearing only within the last ~200 years. Although at the beginning of the 14th Century the basic geometry of the rainbow was known, it was not until Isaac Newton's experiments in the late 1600s that scientists began studying the Sun's spectrum. Joseph Fraunhofer observed over 500 dark lines in the Sun's spectrum in 1814. These are today known as Fraunhofer lines. In the mid 1800s Gustav Kirchoff and Robert Bunsen studied the spectra of various chemical elements. Once these were known, astronomers began using these "fingerprints" to determine chemical compositions of astronomical objects (Appenzeller, 2013).

Early spectrometers used prisms to disperse incoming light into its constituent wavelengths. However, in the 20th Century diffraction gratings have slowly replaced prisms, especially as manufacturing methods and standardization have improved. With the advent of photographic methods and eventually CCDs, spectroscopy has matured.

Astronomical spectra fall into a few types: continuous, absorption, or emission. A continuous spectrum for example would be the highly ionized interior of the Sun. The wavelength of peak emission is determined by its temperature. When photons from a continuous source pass through another material, photons of certain wavelengths are absorbed corresponding to the chemical composition of the material. When observed in front of the continuous source, the spectrum from the material appears to have missing wavelengths or dark lines. This is

known as an absorption spectrum. The photons absorbed by the material will usually be re-remitted, but in random directions. When viewed without the continuous source behind it, the material's spectrum appears dark except for emission lines at those earlier missing wavelengths (McLean, 2008).

Asteroid spectroscopy is different from other types of spectroscopy in that what is measured is light from the Sun – which in itself is not constant with respect to wavelength and contains absorption features – reflected off the asteroid. Thus, by obtaining a spectrum of an asteroid, one is measuring the reflectance of the Sun's light off the asteroid's surface as a function of wavelength. This is a reflectance spectrum.

The resolution of spectrometers is defined as the ratio of the wavelength divided by the smallest discernible change in wavelength ($R = \lambda/\Delta\lambda$) and varies from very high ($R > 25{,}000$) to intermediate ($R \sim 5{,}000$) to low ($R \sim 500$) (McLean, 2008). Lower resolutions are better for observing fainter objects, such as asteroids. In effect, the light (signal) from an object is being "spread" over a range of wavelengths, so using low-resolution spectrometers for asteroid spectroscopy acts to preserve signal-to-noise ratio.

Performing asteroid spectroscopy is an arduous task. Not only does a relatively faint asteroid moving in a non-sidereal manner have to be tracked, but the Sun's spectrum must be removed from the raw spectrum of the asteroid. Since the Sun is not visible when these observations take place, usually a Solar analog star is observed which has a similar spectrum to that of the Sun, and this is used to remove the Sun's spectrum from the asteroid's raw spectrum. In addition, telluric features due to the passage of light through Earth's atmosphere must be accounted for, and this is accounted for through obtaining spectra of several standard stars. Observations of Solar analog and standard stars should occur at similar airmass to the asteroid.

Sky background must be subtracted, and this can be done by "nodding" the telescope between the asteroid and background sky. Wavelength calibration must also be performed. The exact details of asteroid spectroscopy data analysis are beyond the scope of this literature review, but it is a relatively time-and-effort-intensive task. Examples of these procedures as well as different spectroscopic surveys performed can be found in the Asteroid Data-Collection Efforts section.

Asteroid spectra have been successfully obtained in both the visible and near-infrared (NIR) (DeMeo et al., 2009). Visible spectroscopy usually ranges from ~0.4 – 1.1 μm and NIR spectroscopy ~0.8 – 2.5 μm. Individual spectrometers will have slightly different characteristics, but these ranges are general rules-of-thumb for visible and NIR asteroid spectroscopy. There is a small overlap of wavelength ranges between visible and NIR defined here. This overlap has been used to attempt to construct combined visible/NIR spectra of asteroids (DeMeo et al., 2009). Once again, specific examples of spectroscopic efforts can be found in the Asteroid Data-Collection Efforts section.

Once the spectrum of the asteroid is obtained, its absorption features become evident. These absorption features can be very broad as they are due to mineral structures. This is also a reason why low-resolution spectroscopy works adequately for asteroids. Measurements of the properties of these absorption features gives clues as to the composition of the object under study. In asteroid spectroscopy, for example, 1 and 2 μm absorption features indicate the presence of olivine and/or pyroxene. The measurement of the centers of these bands and the sizes of these bands indicates the relative amounts of these minerals on the asteroid's surface (Gaffey et al., 1993). Other absorption features may be observable, such as one near 0.7 μm due to the presence of phyllosilicates. Below in Figure 12 are sample asteroid spectra.

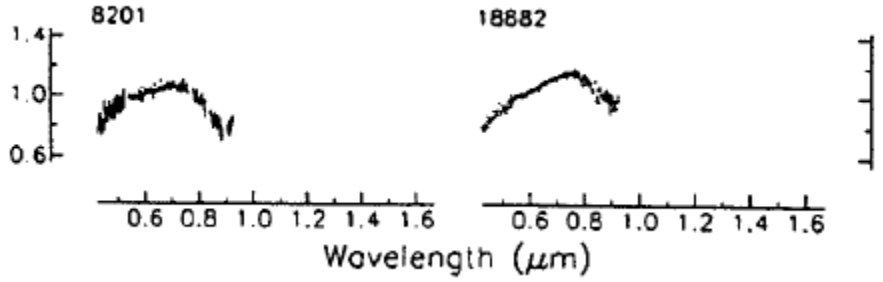

Figure 12: Visible spectra of asteroids 8201 (1994 AH2) and 18882 (1999 YN4) from Binzel et al. (2001). Both asteroids are NEAs and show a 1 μm absorption feature. 8201 is classified as O-type and 1882 is S-type.

Another property of asteroid spectra is spectral slope S, defined as change in reflectance with respect to wavelength $S = \Delta R/\Delta\lambda$. There are multiple ways to measure this practically. Jewitt (2002) defined spectral slope S' as percent change in reflectance per 1,000 Angstroms (0.1 μm) (Jewitt, 2002).

S' = % change in reflectance/0.1 μm

Spectral slope varies greatly among the asteroid population, from slightly blue (-5%/10^3 Angstroms, Å) to moderately red (+10%/10^3 Å) in the visible range of the electromagnetic spectrum (Jewitt, 2002). Spectral slope may depend on many factors, such as surface composition of the asteroid, observation geometry, and space weathering effects (Sanchez et al., 2012). This section serves to only give a brief overview of the science of spectroscopy, so more details of these will be delegated to their respective sections in this literature review.

Asteroid spectra are also usually normalized to unity at a specific wavelength value. For example, asteroid spectra in the Small Main Belt Asteroid Spectroscopic Survey (SMASS) were normalized to 0.55 μm (Bus & Binzel, 2002A). Normalization depends on wavelength range covered in the spectrum as well, so a NIR spectrum may be normalized to unity at 1 or 1.5 μm.

The last topic to be discussed with respect to asteroid spectroscopy is spectrophotometry. Spectrophotometry is a mixture between photometry and spectroscopy in which photometry is plotted as a function of wavelength. The details of this process are described in the Data Analysis section, but for asteroids once the calibrated magnitude in a certain filter is determined, that magnitude is transformed into reflectance by the following equation

$$F_j = 10^{-0.4[(m_j - m'_r) - (m_j - m'_r)_\odot]}$$

where F_j is the reflectance in the jth filter, m_j is the calibrated magnitude in the jth filter, and m_r' is the calibrated magnitude in the filter to be normalized to (Alvarez-Candal, 2013). The ⊙ symbol represents these values for the Sun, as the Solar contribution must be removed. So, $m_j\odot$ and $m_r'\odot$ are Solar magnitudes in the respective filters. For Solar colors in the ugriz photometric system, g – r = 0.40, r – r = 0, i – r = -0.11, and z – r = 0.128 (Sloan Digital Sky Survey, 2020). The resulting spectra look like Figure 13.

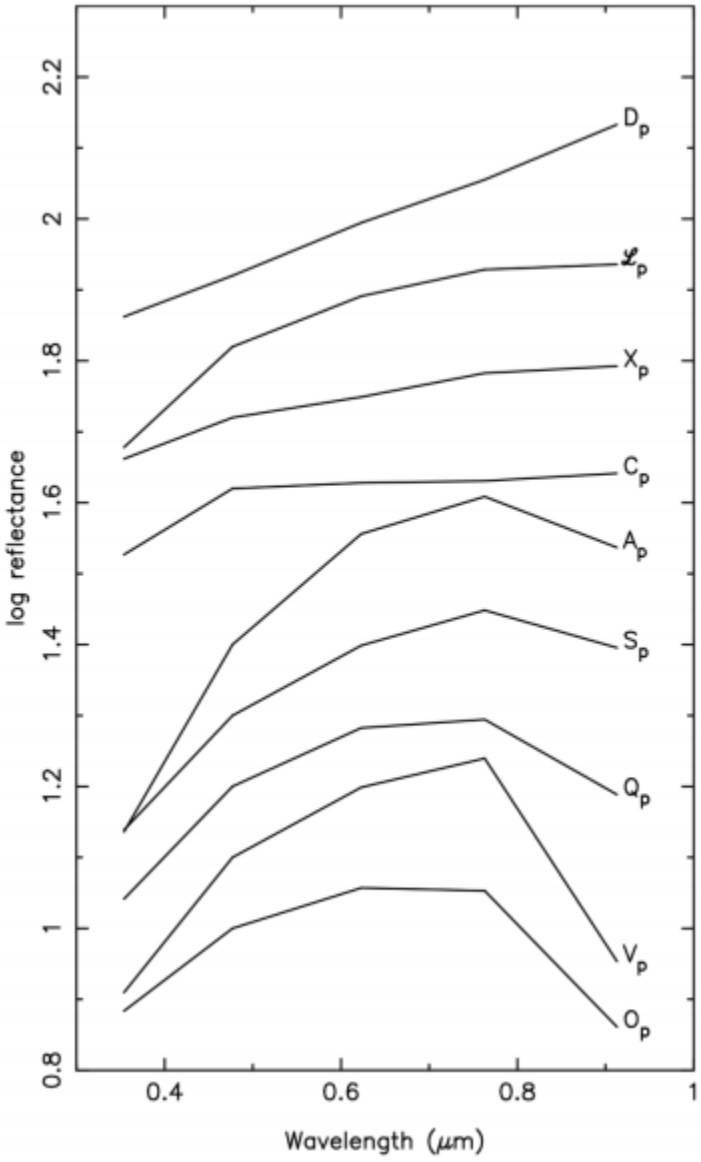

Figure 13: Representative photometric spectra of asteroids from Carvano et al. (2010). These photometric spectra use the u filter as well as g, r, i, and z filters.

In conclusion, spectroscopy is a powerful tool used to determine the physical, chemical, and mineralogical properties of asteroids. Next, effects based on observing geometry will be discussed.

Phase Angle Effects

Since the 1960s, scientists have studied how viewing geometry affects the features of objects' visible and near-infrared spectra. Laboratory samples of meteorites, computational modeling, and observational studies of Solar System objects have been included in this research (Gradie & Veverka, 1986), resulting in photometric functions to describe changing light intensity reflected from an object as a function of viewing geometry. Asteroids, being Solar System objects, have been studied as well. For example, the UBV colors of asteroids are known to become redder with increasing Sun-asteroid-Earth angle (Gehrels, 1970; Gehrels & Tedesco, 1979). The NIR spectrum of 1566 Icarus changes greatly between Sun-asteroid-Earth angles of 40 – 90 degrees (Gehrels et al., 1970). Spectral slopes of NEAs also tend to be higher than Main Belt asteroids, likely due to their higher Sun-asteroid-Earth angle of observation (Luu & Jewitt, 1990). As a general rule, as the Sun-object-Earth angle – the phase angle – increases (see Figure 14), the object's spectrum becomes redder and absorption features become deeper. Why does this occur?

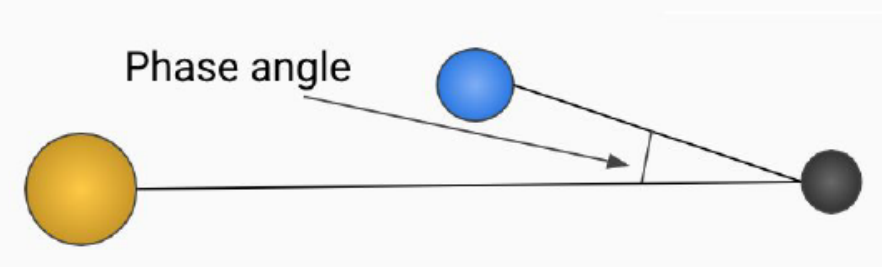

Figure 14: Phase angle general graphic. The yellow object represents the Sun, the dark grey object represents the asteroid, and the blue object represents the Earth.

As mentioned above, any spectrum from an asteroid is a reflectance spectrum in which the light originates at the Sun, interacts with the asteroid through reflection and absorption, and then travels through space, the atmosphere, and finally enters the telescope. Reflectance spectra are controlled by the single scattering albedo, which in itself is a function of the absorption coefficient. The absorption coefficient is a variable describing how deep light *of a certain wavelength* can penetrate into a surface before being absorbed, and is *inversely proportional* to wavelength (Sanchez et al., 2012). Thus, the single scattering albedo is wavelength-dependent. As phase angle increases, light is less able to escape from the surface, and this results in an overall decrease in reflectance across the entire spectrum. But since the absorption coefficient is wavelength dependent, bluer light will be absorbed more than redder light. Thus, the spectrum appears to be redder, and so is called phase reddening. This is shown in Figure 15.

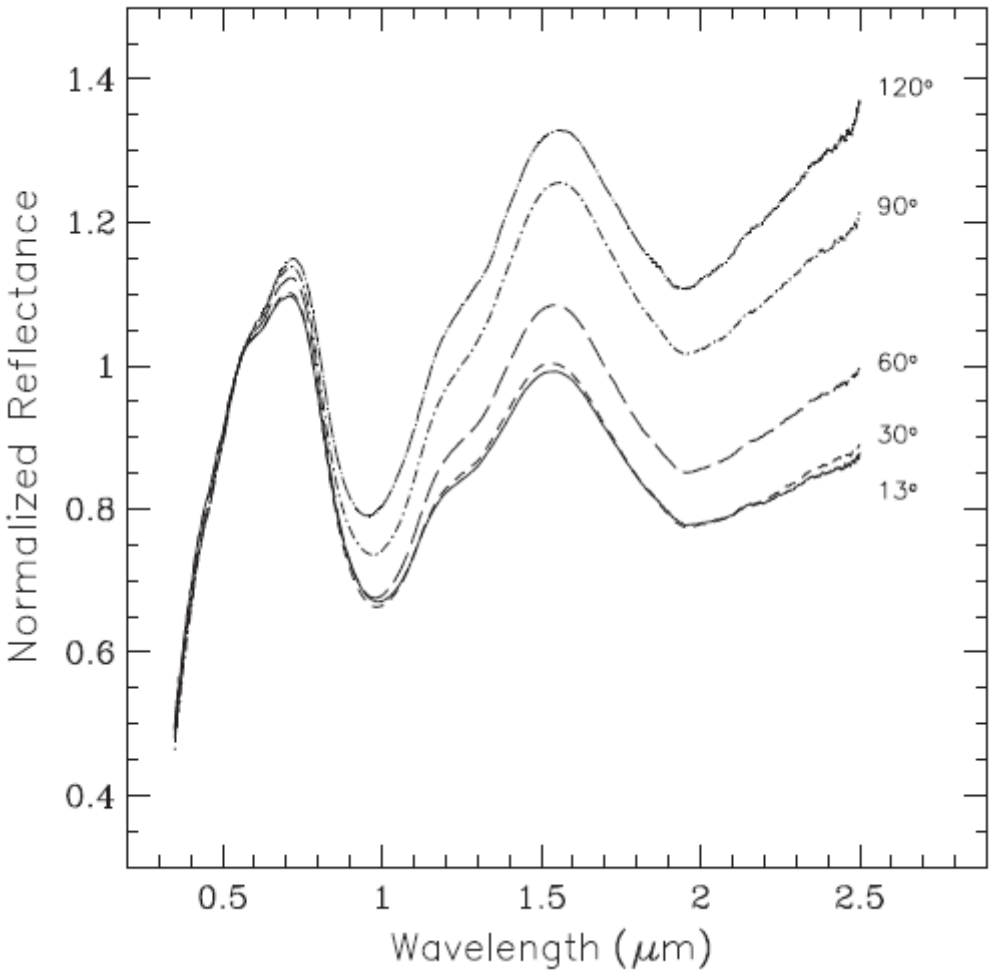

Figure 15: Reflectance spectrum for LL6 chondrite Dhurmsula from Sanchez et al. (2012). Notice two effects: 1) as phase angle increases, reflectance increases at longer wavelengths, and 2) as phase angle increases, the depths of absorption bands increase.

There are more effects at play, though. In addition to reddening the reflectance spectrum, phase reddening also affects absorption band parameters (Gradie & Veverka, 1986; Sanchez et al., 2012). Band depth is found to generally increase for phase angles from ~2 – 55 degrees, and is more or less constant at angles beyond this. Why does this occur? Gradie and Veverka (1986) found that the phase coefficient – the change in magnitude/degree of phase angle – is inversely

proportional to the normal reflectance in basalt and Allende (carbonaceous chondrite) samples. In order to have a *large phase coefficient*, efficient shadowing among surface particles must exist, which means that the *surface grains must be more opaque*. In contrast, in order to have a *small phase coefficient*, inefficient shadowing must exist, and *more transparent grains must exist on an object's surface* (Gradie & Veverka, 1986). So, as reflectance decreases, the phase coefficient increases; for an absorption band which by definition reflects less light, the phase coefficient increases and therefore band depth increases. It was also determined by studying the effects of surface roughness on phase coefficients that differences in phase coefficients between S-type and C-type asteroids can be primarily attributable to differences in reflectance and not differences in surface roughness (Gradie & Veverka, 1986). Thus, many S- and C-type asteroids may have similar surface roughness. To extend this theory, phase coefficient should also vary across the absorption and thus band center will change with respect to phase angle. Sanchez et al. (2012) found that band center may change, but this change is within the error bars for band center measurements, so no definitive conclusions could be made.

Phase reddening has also been studied in large-scale astronomical surveys and using Hapke models. Carvano and Davalos (2015), in their analysis of SDSS photometry of asteroids, found that the 55.4% of asteroids in SDSS displayed phase reddening trends consistent with previous studies. That is, as phase angle increases, spectral slope increases and band depths increase. However, they also found that 24.4% showed no correlation with increasing phase angle and 20.2% showed an *anti-correlation* with increasing phase angle. Positive correlation between spectral slope and phase angle also appears to be weaker for asteroids without a 1 μm absorption feature. They found that only 47.1% asteroids classified as C-/X-/D-type showed a positive slope-phase angle correlation vs 59.5% of V-/S-/Q-types.

Carvano and Davalos (2015) also used Hapke models and showed that phase reddening increases as surface material becomes more forward-scattering, while surface materials that are extremely back-scattering can show a negative relation between phase reddening and spectral slope. In addition, phase reddening increases for more elongated objects. Since many asteroids are not spherical but are elongated, this result is directly applicable to asteroid science.

Sample	Parameter	Total	Correlation (%)	No correlation (%)	Anticorrelation (%)
All	*slope*	2077	1150 (55.4)	508 (24.4)	419 (20.2)
C, X, D	*slope*	626	295 (47.1)	164 (38.2)	167 (26.7)
V, S, Q	*slope*	1164	692 (59.5)	274 (23.5)	198 (17.0)
V, S, Q	*bd*	1164	480 (41.2)	310 (26.6)	374 (32.2)

Table 5: Table 1 from Carvano and Davalos (2015) showing phase angle and band depth relationships for asteroids found in the MOC4. Acronym: bd (band depth, referring to 1 μm band depth due to olivine and/or pyroxene).

Phase reddening can also look a lot like space weathering (Sanchez et al., 2012). The phenomenon of space weathering will be discussed later, but in short, space weathering also reddens spectra. Increasing phase angle from 30 – 120 degrees can produce a reddening of reflectance spectra equivalent to exposure times of 100,000 – 1.3 million years (Sanchez et al., 2012). Both phase reddening and space weathering must be taken into account when studying asteroids.

Can phase reddening affect the analysis of asteroid spectra? The short answer is yes, but probably only if the asteroid's spectrum is close to one of the taxonomic boundaries. The effects of phase reddening usually lie within the error bars for taxonomic classification (Sanchez et al., 2012). On a different note, knowledge of the phase coefficient of an asteroid's spectrum coupled

with its reflectance can provide constraints on surface grain size (Gradie & Veverka, 1986). Thus, if one knows the spectral reflectances and phase coefficient, estimates of surface grain size can be made. Even if phase coefficient is not tightly constrained, an asteroid's spectral slope vs phase angle relationship can be used to make educated guesses about its surface properties.

All in all, phase reddening can thus be summarized as the reddening of spectra and increase in band depths as phase angle of observation increases.

Asteroid Data Collection Efforts:

Throughout the second half of the 20th Century, many efforts have been made to observe large numbers of asteroids in order to classify them into dynamical and taxonomic categories. These categories will be discussed later. The developments of materials science, electronics, and the ability to launch telescopes into space has opened up much wider regions of the electromagnetic spectrum and has aided greatly in studying and classifying asteroids. The following is a list of asteroid data collection efforts. Although not exhaustive, this review includes studies most relevant to the thesis question.

24 Color Asteroid Survey:

The 24 Color Survey used the McCord Dual Beam Photometer at Mt. Wilson, Mt. Palomar, and Kitt Peak. Dual beam photometry images the asteroid and a nearby patch of sky repeatedly in order to minimize the effects of changing sky conditions such as clouds or atmospheric extinction. The wavelength range for this survey was from 0.32 – 1.08 μm over 24 filters. Spectra were normalized at 0.57 μm and were also averaged over multiple observations of the same asteroid. An alpha Lyrae standard star was used for calibration, causing an

uncertainty of ~2% in visible and ~4% in infrared (Chapman et al., 1973; McCord and Chapman 1972, 1975; Chapman and Gaffey, 1979).

ECAS:

The Eight Color Asteroid Survey (ECAS) used the eight color photometer at the 1.54 m Catalina and 2.29 m Steward telescopes (Tedesco, Tholen, & Zellner, 1982). The filters used had the following wavelength ranges: s – 0.310 μm, u – 0.320 μm, b – 0.430 μm, v – 0.545 μm, w – 0.705 μm, x – 0.860 μm, p – 0.955 μm, and z – 1.055 μm. Thus ECAS used overlapping filters ranging from 0.31 – 1.07 μm (Zellner et al., 1985). Data were normalized at the v filter (0.545 μm). ECAS obtained spectrophotometry of 589 small Solar System bodies, and included ~50% of the numbered objects from the NEO, Hungaria, Nysa, Cybele, Hilda, and Trojan populations. Tholen (1984) used results from ECAS to expand on the Chapman (1975) asteroid taxonomy and therefore obtained the Tholen taxonomic classification system.

52 Color Asteroid Survey:

The 52 Color Survey was a near-infrared survey covering the wavelength range of 0.8 – 2.5 μm. It was conducted from 1983 – 1987. In total, 119 asteroids were observed. In order to compare with the data from ECAS, spectra were normalized at 0.55 μm (Bell et al, 1988; Gaffey, Reed, & Kelly, 1992). The NASA Infrared Telescope Facility (IRTF) 3 m telescope was utilized, with two circular variable-bandpass filters (CVFs) in order to obtain photometry in 52 bandpasses. For each observation, standard stars were observed 2 – 3 times and used for extinction coefficient calculations relative to 16 Cyg B. Multiple starpacks – models to calculate

the standard star flux-to-airmass relation – were calculated through each observation run, which minimized observational and instrumental errors.

SMASS I, SMASS II and SMASS IR:

The Small Main Belt Asteroid Spectroscopic Survey (SMASS) collected visible-wavelength spectra of Main Belt asteroids, and was the largest survey attempt since ECAS. It used the Michigan-Dartmouth-MIT 2.4 m Hiltner telescope located at Kitt Peak National Observatory (KPNO). SMASS had a resolution of ~10 Å/pixel and covered the wavelength range of ~0.4 – 1.0 μm up to a visual magnitude of 19.0 (Xu et al., 1995; Bus & Binzel, 2002A; Bus & Binzel, 2002B). The 4.7 arcsecond-wide slit was oriented in a north-south direction to minimize the effects of atmospheric dispersion and gave a spectral resolution of 0.007 μm (R ~ 100). While this is a low spectral resolution, it improved signal-to-noise ratio, especially for fainter asteroids. It should be noted that while this long-slit spectroscopy used allowed for imaging of fainter asteroids in a single exposure, effects from asteroids' rotation (i.e., their light curves) were averaged in the processing of these spectra.

For SMASS I (Xu et al, 1995), multiple flat-field images were taken. There were issues applying the flats evenly to both the blue and red ends of the spectrum, which resulted in lower signal-to-noise ratio at the ends of the spectra. In order to minimize this effect, asteroids were placed along the same CCD columns. Telluric features at 0.760, 0.900, and 0.940 μm were removed and spectra were normalized at 0.55 μm. Standard stars were observed at within 0.1 airmasses of the asteroid in order to remove the effects of wavelength-dependent atmospheric absorbance. Brighter asteroids with well-known spectral features were also used to correct for

instrumental effects. The asteroid spectral flux was divided by the spectral flux of these standard stars.

For SMASS II, Image Reduction and Analysis Facility (IRAF) was used for data reduction and analysis. Mean bias levels were measured from the unexposed overscan region of the CCD and then were subtracted. Inherent flat-field characteristics of the CCD cameras were used instead of performing flat-field corrections. The wavelength calibration was performed using a dispersion model based on mercury-argon-xenon lamps. Atmospheric extinction was corrected for by using a mean extinction model developed for KPNO. The spectra were normalized at 0.55 μm as well.

Initial results from observations of 316 asteroids were published by Xu et al. (1995) with a wavelength range of 0.4 – 1.0 μm, with follow-on publications from Bus and Binzel (2002A) and Bus & Binzel (2002B) with a wavelength range of 0.435 – 0.925 μm. The wavelength range was reduced from 0.4 – 1.0 μm to 0.435 – 0.925 μm in Bus and Binzel (2002A; 2002B) for consistency and to reduce effects from CCD quantum efficiency reduction on the far ends of the spectra. All in all, 26 taxonomies were identified using 1,447 Main Belt asteroid spectra from this survey. To date, SMASS has contributed the most visible-wavelength spectra of asteroids.

In addition to SMASS I and SMASS II, a near-infrared (NIR) survey was performed by Burbine and Binzel (2002) using NASA IRTF. The spectral range for this survey was approximately 0.9 – 1.6 μm and used a specialized grism. NIR spectra for 181 asteroids were obtained, with more than 50% of them having diameters smaller than 20 km. The focus for this survey was on olivine- and pyroxene-dominated asteroids because it complemented the spectral range of the instrumentation.

S3OS2:

The Small Solar System Objects Spectroscopic Survey (S3OS2) obtained visible-wavelength spectra of 820 asteroids from 1996 – 2001 at the 1.52 m telescope at European Southern Observatory (ESO), covering a wavelength range of 0.490 – 0.920 μm (Lazzaro et al., 2004).

A grating of 225 gr/mm with a dispersion of 330 Å/mm in first order was utilized. Spectra were taken using a 5 arcsecond slit aligned in the east-west direction in order to reduce the loss of light due to the movement of the asteroid, as the telescope did not have automated differential tracking. Thus, most asteroids were observed at a small zenith distance to compensate for the east-west orientation of the slit as opposed to the preferential north-south direction used in SMASS.

Most Main Belt asteroids were observed at small phase angles (median of 13.7 degrees) in order to minimize phase reddening. IRAF was used to reduce and analyze the spectra, with wavelength calibration performed using a helium-argon lamp. Airmass correction was performed using the mean extinction curve for the observatory, and multiple solar analog stars were observed during each observing run. Spectra for each asteroid were obtained multiple times each night, but instead of the spectra being averaged, only the best spectrum was selected. 70% of asteroids were observed more than once, and 53% were observed on multiple or consecutive nights.

Since S3OS2 was a Main Belt asteroid survey, it only covered a distribution of asteroids from 2.2 – 3.3 AU, and the spectra it obtained were classified according to Tholen and Bus and Binzel taxonomies, with good agreement (Lazzaro et al., 2004).

Sloan Digital Sky Survey (SDSS):

The Sloan Digital Sky Survey began operations in 2000 using the 2.5 m telescope at Apache Point Observatory, and focused obtaining photometric and spectral observations of the northern sky and Galactic cap regions (Gunn et al., 2006; Ivezic et al., 2010). The photometric observations utilized a filter system of u, g, r, i, and z filters. The filters had almost zero overlap and had central wavelengths of 0.3551, 0.4686, 0.6165, 0.7481, and 0.8931 μm, respectively. Among the objects observed were asteroids, which were compiled into the Moving Objects Catalog (MOC). The MOC includes observations linked to known asteroids as well as undiscovered moving objects. There were four releases of the MOC, with MOC4 including 471,569 moving objects, with 220,101 observations linked to 104,448 known asteroids (Carry et al., 2016). Many asteroids were observed multiple times. Although operating with a restricted wavelength range and low resolution, the sheer amount of data produced by this survey is very useful. The u, g, r, i, z filters are commonly used today, both by PanSTARRS and by the Cerro-Tololo Inter-American Observatory (CTIO) 1 m telescope.

WISE/NEOWISE:

MIR/TIR space telescopes have revolutionized studies of asteroid albedo, size, and size distribution. The first was the Infrared Astronomical Satellite (IRAS), launched in 1983 (Neugebauer et al., 1984). More recently, the Spitzer Space Telescope and WISE/NEOWISE have contributed orders of magnitude more data, allowing large-scale studies of asteroid populations with accurate albedo measurements (Mainzer et al., 2011).

Contrasting from previous surveys, the Wide Field Infrared Explorer (WISE) was a space-based survey conducted entirely in infrared wavelengths (Mainzer et al., 2011). The 0.40

m telescope was launched into a polar orbit in December 2009 and conducted an all-sky survey at 3.4, 4.6, 12, and 22 μm. Because the telescope was in orbit, its observations were unhindered by Earth's atmosphere. The initial survey was conducted in all four wavelengths, then when coolant was exhausted it continued observations at 3.4 and 4.6 μm. WISE was briefly put into hibernation in February 2011 then recommissioned in 2013 and redubbed NEOWISE to perform a three year survey to observe only NEOs. As of 2020, WISE/NEOWISE has discovered 336 NEOs in total, including 308 NEAs, 28 comets, and 56 potentially hazardous asteroids (PHAs) (CNEOS, 2020). Since NEA orbits are inherently unstable (Bottke et al., 2002; DeMeo & Binzel, 2008) small perturbations of these objects' orbits may cause them to collide with Earth on short timescales, so PHAs are defined as NEAs that pass within 0.05 AU of Earth.

Currently, NEOWISE does not have the ability to point, but its polar orbit ensures it images the entire sky over the course of a year. One of the benefits of WISE's/NEOWISE's wavelength range is that it enables accurate diameter and albedo determinations of asteroids, and this has increased the number of asteroids with known albedos and diameters by multiple orders of magnitude.

Palomar Transit Facility (PTF):

Compared to the other asteroid surveys, the Palomar Transit Facility (PTF) is unique. The PTF uses the 1.2 m Oschin-Schmidt telescope with 11 CCDs to image 7.3 deg^2 of the sky at a time with a resolution of 1.0 arcsecond/pixel. It has observed approximately 54,000 asteroids, and out of those observed, Waszczak et al. (2015) published rotation periods for 8,300 of them. As a result, PTF has effectively doubled the size of the Light Curve Database (LCDB) (Warner et al., 2009). However, each asteroid observed by PTF is sampled only twice per night, thus

these observations have very low temporal resolution. As a result, rotation periods determined using PTF data can often only be used as an initial estimation of the asteroid's rotation period, and follow-up observations are usually needed to further constrain it.

Physical Properties of Asteroids:

Now that the basics of asteroid discovery and study have been covered, how have these efforts increased our knowledge of asteroids? In order to better understand the physical (and dynamical) properties of asteroids, a discussion of the origin of the Solar System must first be had. There have been many theories of the origin of the Solar System. Immanuel Kant actually proposed the first theory of Solar System formation, called the nebular theory, in 1755 (Woolfson, 1993). Other theories were proposed throughout the decades, including tidal theory and capture theory, but in the 20th Century scientists returned to Kant's original idea, although with many refinements (North, 2008). Today, the nebular theory has been generally accepted by the scientific community, although it is much more rigorous today than Kant's original hypothesis.

Solar System Formation:

In the current version of the nebular theory, about 4.6 billion years ago, the Solar System was initially a large, slowly rotating cloud of dust and gas approximately 2% of the Sun's mass (Gomes et al., 2005; Montmerle et al., 2006; Morbidelli et al., 2005; Tsiganis et al., 2005). The nebula contracted and through conservation of angular momentum it flattened and began to rotate faster. Small particles of gas and dust began to condense in the nebula, first sticking together by electrostatic forces. Once the masses became large enough, gravity began to take

over, and larger and larger bodies formed. In the outer Solar System, viscosity and tidal friction helped form the giant planets by pulling in gas from the surrounding nebula. In the region interior to Jupiter's orbit, gravitational perturbations drove material inward toward the Sun. This material condensed and formed the asteroids (Montmerle et al., 2006).

The nebular theory has received support by observations of other solar systems in the Milky Way Galaxy. Other solar systems in the process of formation have a flattened disk of material resembling an ecliptic plane. As a result, observations of other solar systems can show the process of solar nebula collapse to planetary formation. We can learn a lot about the formation of our own Solar System from observing these other solar systems, but other details still remain obscured. For example, the exact chemical composition of our Solar Nebula is unknown because the vast majority of the material from the Solar Nebula now resides in the Sun and planets, which have their own material recycling processes. As a result, most of the material on these objects has been recycled many times over. However, there is a very small amount of material – less than 0.01% of the original Solar Nebula mass – that has not been materially altered and thus can be counted as "pristine," although this definition is up for debate as well. This mass currently resides in asteroids, comets, and other SSSBs. Asteroids are the primary focus of this study, but as has been discussed earlier, there is currently much gray area between the definitions of "asteroid" and "comet." All in all, understanding the formation and evolution of our Solar System is crucial for understanding not only its original composition but also its chemical and dynamical evolution, and how it may evolve in the future. For example, one of the major problems today is how to explain how the Main Belt is only ~5×10^{-4} Earth masses when models predict an original mass of ~1 – 2.5 Earth masses (Bottke et al., 2015). Thus, any model

explaining the dynamical evolution of the Solar System must account for this large mass discrepancy.

The material from which asteroids formed varied as both a function of radial distance from the Sun – and therefore temperature – and also time of formation (Vernazza & Beck, 2017). Some of the largest asteroids likely formed first, melted and differentiated due to radioactive decay of Aluminum-26, and then were subsequently collisionally disrupted. These are likely the A-, E-, K-, L-, M-, O-, V-types, and other "end member taxonomy" asteroids (Vernazza & Beck, 2017). Their relative scarcity due to likely collisional evolution supports this hypothesis. Later generations of asteroids formed from already-cooled material, and that is what we observe as the S-complex asteroids (Vernazza & Beck, 2017). Material beyond the "soot line" at ~2.7 AU contained carbonaceous material in solid form, as well as water (Beatty, Petersen, & Chaikin, 1999). Thus, a compositionally distinct class of objects formed in this region, and they are known as the C-complex of asteroids (Vernazza & Beck, 2017). In addition, material from the giant planets region was likely scattered both inward into the Main Belt and outward into the Kuiper Belt and Scattered Disk (Bottke et al., 2002). These scattered objects are probably the P- and D-types of asteroids, and populate the outer Main Belt as well as Jupiter Trojan populations (Vernazza & Beck, 2017). This formation probably occurred within the first few tens of million years after Solar nebula collapse. Although collisional and dynamical evolution have mixed asteroid populations throughout time, a rough compositional gradient still exists in the Main Belt due to formation temperature and also due to gravitational perturbations from planetary migrations (see Figure 16). The way this compositional gradient in the Main Belt is inferred is through asteroids' spectral features (DeMeo & Carry, 2013). Thus, the Main Belt is a mish-mash of SSSBs from a range of formation locations and times.

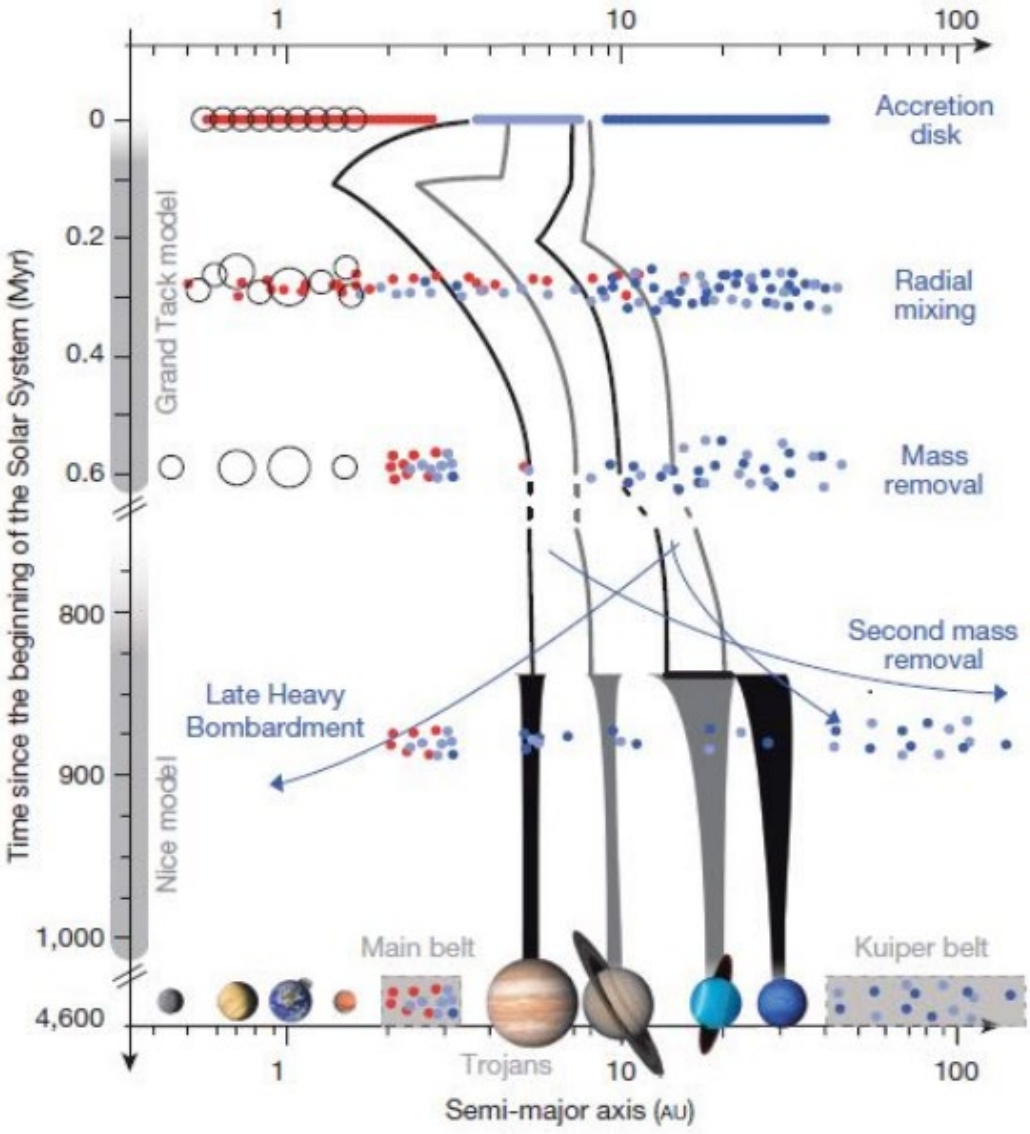

Figure 16: Graphic of Solar System Formation and Evolution, created by combining several proposed models, including the Nice Model and Grand Tack Model. From these planetary dynamics it is clear that 1) the Main Belt consists of a wide range of compositions, 2) a Late Heavy Bombardment occurs for inner Solar System planets, and 3) a Kuiper Belt, Scattered Disc, and Oort Cloud are formed from mass removal events. The figure is from DeMeo & Carry (2014). For a more thorough explanation of Solar System formation and evolution, see Vernazza & Beck (2017), Gomes et al. (2005), Montmerle et al. (2006), Morbidelli et al. (2005), and Tsiganis et al. (2005).

Taxonomies:

Starting in the 1970s and 1980s, astronomers worked to classify asteroids by their visible – and later near-infrared – spectral features (Chapman et al., 1975; Tholen, 1989). These classification schemes often are tied to specific surveys, and the means of classification and the classifications themselves have evolved through time. Below is an overview of different taxonomies that have been proposed to classify asteroids.

Chapman:

Early taxonomies included just two classes of asteroids: S-types and C-types (Chapman et al., 1975). S-type asteroids have a moderately red spectral slope with a broad absorption feature near 1 μm. S-type objects also tend to have higher geometric albedos (> 0.1). C-types have slightly blue to slightly red spectra, but no large visible absorption features (some asteroids belonging to the C-complex were later found to have a 3 μm absorption feature attributed to hydrated silicate minerals) (Bus & Binzel, 2002A). C-types also tend to have lower geometric albedos (< 0.1).

Tholen:

The Tholen taxonomy developed in the 1980s classified 14 different types of asteroids based on the Eight Color Asteroid Survey (ECAS) using overlapping filters ranging from 0.31 – 1.07 μm (Tholen, 1989). Tholen's taxonomic system was the first to utilize principal component analysis (PCA) which showed that almost all spectral variations could be represented using two principal components. It is an expansion of the Chapman et al. (1975) system and includes 14 taxonomic types, the majority being classified as S-, C-, or X-type. X-types could be classified

into E-, M-, or P-type, depending on their geometric albedos (E-types having the highest albedo and P-types having the lowest). X-type asteroids' albedos could vary from ~0.05 to > 0.2. There are also small classes A-, B-, D-, F-, G-, T-, Q-, R-, and V-types, as shown in Figure 17 (Tholen, 1989).

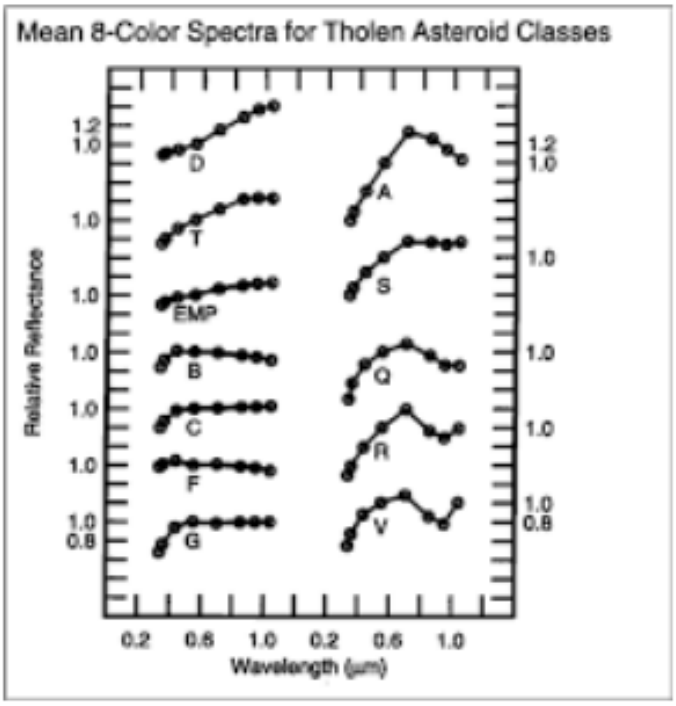

Figure 17: Tholen ECAS taxonomy figure (Tholen, 1989).

Bus and Binzel:

The more recent Small Main Belt Asteroid Spectroscopic Survey (SMASS) asteroid taxonomy (Xu et al., 1994; Bus & Binzel, 2002A; Bus & Binzel 2002B) included 26 distinct asteroid spectral classes. Although Tholen's taxonomies are still used for reference, the SMASS data used by Bus & Binzel (2002A, 2002B) has higher spectral resolution because it used

spectroscopic measurements instead of ECAS's spectrophotometry. However, ECAS covered more of the ultraviolet and infrared wavelengths.

The Bus and Binzel taxonomy retains the three major original taxonomies but also includes small sub-groups as well as end-member groups. All in all, 26 taxonomies were identified from 1,447 Main Belt asteroid spectra ranging from 0.44 – 0.92 μm. Unfortunately, since the spectra collected only went up to 0.92 μm, central wavelength of absorption, band width, and band depth of the olivine/pyroxene absorption at ~1 μm was unable to be accurately determined. Fortunately, the 1 μm feature could still be observed as a decrease in reflectance toward the red end of the spectrum.

The method in which Bus and Binzel determined an asteroid's taxonomy is through PCA as well (Bus & Binzel, 2002A). The three values spectral slope, PC2', and PC3' were used. The more negative the PC2' value was, the deeper the ~1 μm absorption feature. PC3' represented higher order variance in the spectrum or an ultraviolet absorption feature (Bus & Binzel, 2002A). SMASS taxonomic types are arranged below on a plot of absorption feature depth to spectral slope in Figure 18.

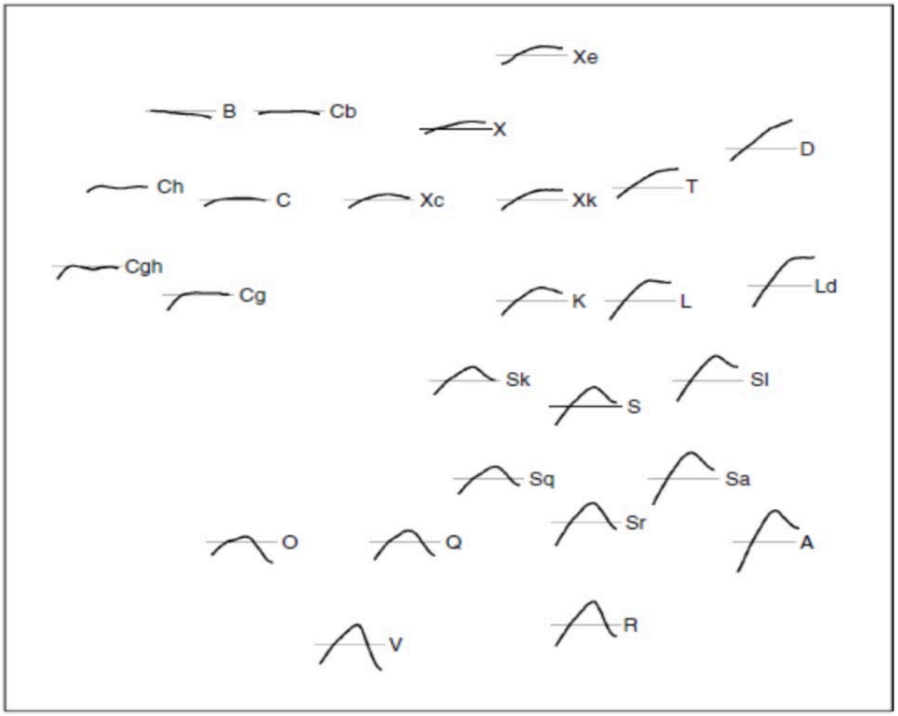

Figure 18: The 26 different SMASS taxonomic types from Bus and Binzel (2002A, 2002B). These representative spectra represent spectral reflectance from 0.44 – 0.92 μm. They are plotted with respect to both spectral slope and 1 μm absorption feature depth.

As can be seen, if an asteroid's spectral slope is near zero, it is similar to a C-type asteroid and would have a constant reflectance (albedo) as a function of wavelength through the visible spectrum. S-types exhibit an increase in reflectance (albedo), with a maximum at ~0.7 μm, which then drops due to the ~1 μm olivine/pyroxene absorption feature. Thus, the primary difference between S- and C-type asteroids' spectra is a higher reflectance near 0.7 μm and a lower reflectance near 1 μm versus a relatively uniform reflectance throughout visible wavelengths. On the other hand, X- and D-types exhibit a generally smooth and featureless increase in reflectance as a function of wavelength, and thus are distinct from both S- and C-

types. Of course, Bus and Binzel identified many more taxonomies that have slight differences in spectral features.

DeMeo:

DeMeo et al. (2009) expanded upon the Bus and Binzel taxonomy by studying asteroids in NIR wavelengths as well as visible wavelengths. They found good correlation between visible and NIR absorption features or lack of features from observations of 371 asteroids at ~0.45 – 2.45 μm. The DeMeo taxonomy is shown below in Figures 19 and 20.

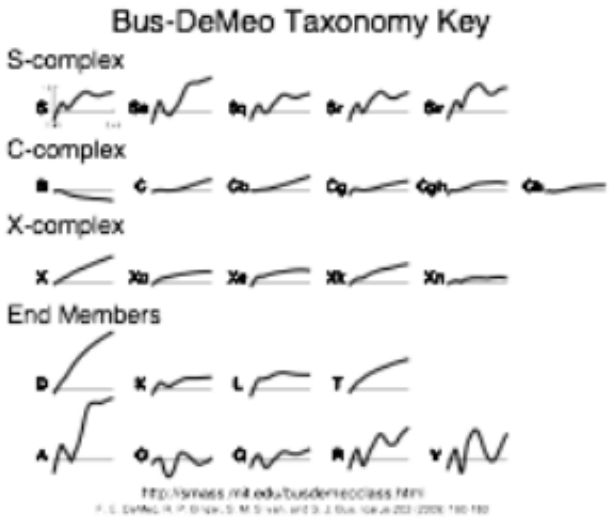

Figure 19: DeMeo taxonomy figure arranged by taxonomic complex (DeMeo et al., 2009).

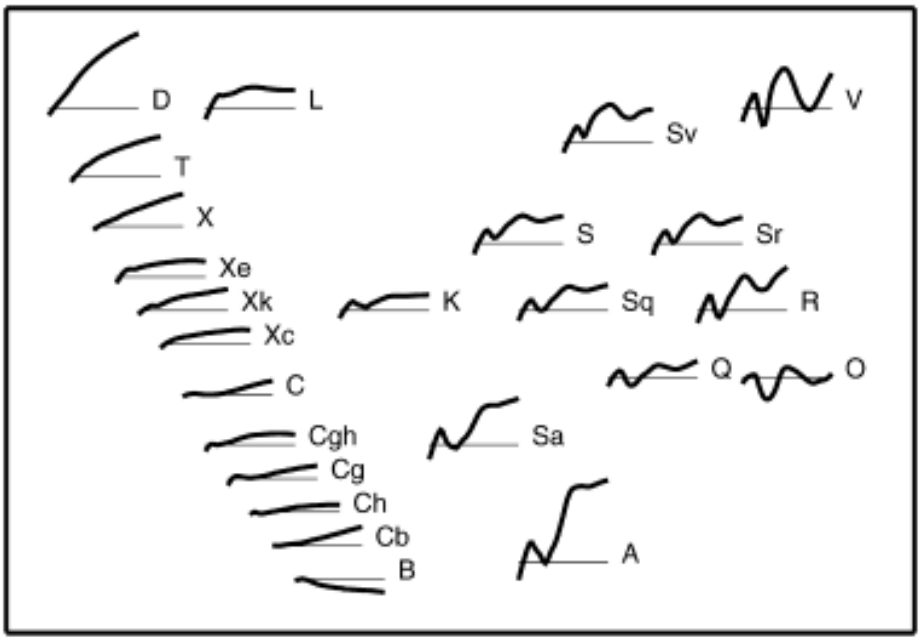

Figure 20: DeMeo taxonomy figure arranged by spectral slope and band depths (DeMeo et al., 2009).

Szabo and Carvano:

As more spectrophotometric data on asteroids were compiled, astronomers began processing large datasets in order to better classify them. Szabo et al. (2004) analyzed 7,531 asteroids from the Sloan Digital Sky Survey (SDSS) Moving Object Catalog Release 3 (MOC3). SDSS and the MOC will be discussed in detail later, but they discovered that some asteroids displayed color variability from observation to observation. This color variability was determined to be significant because the reported error of SDSS was 0.02 magnitude while Szabo et al. (2004) reported variabilities up to 0.11 magnitude. They found no correlations between color and: diameter, absolute magnitude, taxonomy, family, velocity, apparent brightness, angle of opposition, or non-simultaneous measurements. These results point to some asteroids' color variability being real.

Using the SDSS MOC4, Carvano et al. (2010) analyzed 22,019 asteroids having multiple observations and found that 14,962 (67.95%) exhibited taxonomic variability. Carvano et al. (2010) developed a spectrophotometry-based taxonomic classification system, with the subscript "p" denoting that the taxonomy was spectrophotometry-based. One of the most surprising results from this study is that there are 152 asteroids that were classified as both S_p and C_p. This is difficult to rationalize given our current understanding of asteroid taxonomies and their compositional analogs, but will be discussed in more detail below. In addition, Carvano et al. (2010) classified 303 asteroids as both C_p, X_p, and D_p. Although perhaps not as surprising from a compositional standpoint, these are still peculiar results. Thus, there is concern over the repeatability of SDSS observations for moving objects, and this thesis will attempt to examine the repeatability for two such objects and thus the reliability of SDSS observations of moving objects. Reasons for the taxonomic variability in SDSS MOC found by Szabo et al. (2004) and Carvano et al. (2010) may be that phase angle plays a larger role in spectral slope that previously thought, that the surfaces of some asteroids are compositionally non-uniform and a change in reflectance is detected as the object rotates about its axis, or that a higher fraction of asteroids are active than was previously thought. This thesis will shed more light upon the research by Szabo et al. (2004) and Carvano et al. (2010).

Compositions:

So, what do these taxonomies actually *mean*? The first thing to remember is that taxonomy does not necessarily inform composition, and vice-versa. Taxonomy can narrow down the possible compositions that an asteroid can have, but rarely does it point to one particular mineralogy or composition (Carvano & Davalos, 2015). The 1 μm absorption band

prevalent in the S-type asteroids is, as mentioned before, almost certainly due to olivine and pyroxene (fayalite and ferrosilate, respectively). In addition, if one obtains a spectrum extending to ~2.5 μm, an absorption band near 2 μm is also evident. This is probably due to only pyroxene (ferrosilate). Thus, asteroids with 1 and 2 μm absorptions are regarded as stony or silicaceous asteroids, as their visible and near-infrared spectra are dominated by silicate absorption features (Bus & Binzel, 2002A; Bus & Binzel, 2002B). These are the olivine-and pyroxene-dominated asteroids. It is less clear what other taxonomic types of asteroids are composed of, but by comparing their spectra with spectra of meteorites some conclusions can be made. E-type asteroids are likely rich in enstatite (magnesium pyroxene). V-type asteroids – named after its largest member 4 Vesta – are the likely parent bodies of basaltic achondrite meteorites known as HEDs (Vernazza & Beck, 2017). M-type asteroids have been hypothesized to be metal-rich (Vernazza & Beck, 2017). C-group asteroids are probably rich in volatiles, anhydrous silicates, hydrated clay minerals as evidenced by a ~3 μm absorption feature, organic polymers, magnetite, and sulfides (Vernazza & Beck, 2017). P- and D-type asteroids may also contain organic-rich silicates, carbon, anhydrous silicates, and perhaps water ice in their interiors (Vernazza & Beck, 2017). Although plausible matches have been made, it is not yet possible to remove all doubt about these asteroids' surface compositions without *in situ* measurements.

All in all, one of the goals of studying Solar System formation and evolution and Earth's meteorite collection is to determine the compositions of asteroids. This task would be straightforward if spacecraft could visit many various types of asteroids to analyze surface and sub-surface material and perform *in situ* measurements, but budget and resource constraints force astronomers to rely heavily on telescopic observations. Additionally, over the age of the Solar System, asteroids have endured bombardment by micrometeorites, grinding their surfaces into a

layer of dust and rubble called regolith (Pater & Lissauser, 2010). This bombardment actually only affects the top few millimeters of the surface of the asteroid, but since visible and near-infrared observations do not penetrate past the surface regolith, the taxonomic classifications discussed above are only an analysis of asteroidal surface composition. Much research has been performed on particle size and regolith formation, but studies beyond those applicable to visible and near-infrared observations are beyond the scope of this literature review.

Mineralogy:

As mentioned above, different types of asteroids formed out of the Solar Nebula, depending on radial distance from the Sun and time of formation (Vernazza & Beck, 2017). These variables affected their thermal histories. If an asteroid accreted out of the Solar Nebula but did not experience significant post-accretionary heating, then its mineral composition would be largely unaltered and thus its petrology would be sedimentary. If moderate post-accretionary occurred, then the original mineral assemblage would be metamorphosed and thus would homogenize the mineralogy. If strong post-accretionary heating occurred, then the asteroid would have experienced at least partial melting and some degree of differentiation. This would form igneous assemblages. The majority of the meteorite collection probably comes from the latter form of parent bodies (Keil, 2000).

With that said, olivine and pyroxene are two primary minerals in the Solar System that can be observed in both visible and near-infrared wavelengths. It was mentioned that olivine has a ~1 μm absorption feature while pyroxene has both ~1 and ~2 μm absorption features. In reality, olivine has three absorption features centered at ~0.75, 1.04, and 1.25 μm. So, the ~1 μm feature is a combination of both olivine's three absorptions and pyroxene's one absorption at that

wavelength. These absorption features are characterized by three main parameters: central wavelength of absorption, band width, and band depth. These three parameters change based on the relative abundances of olivine and pyroxene.

The spectral absorption features themselves are due to electrons in the minerals absorbing solar flux. Solar photons that have the same energy as an energy level transition in olivine or pyroxene will be absorbed by that mineral and thus its electrons will become excited and transition to a higher orbital state. When visible and near-infrared (vis/NIR) telescopic observations are made of an asteroid – which is reflected light from the Sun – there is missing light at certain ranges of wavelengths. This light was not reflected, but absorbed by the minerals in the asteroid. Thus, astronomers call these absorption features. Many changes in central wavelength of absorption and band depth are due to compositional variations, for example, an abundance of oxidized iron in olivine or an abundance of calcium in pyroxene.

In Figures 21 and 22 below are vis/NIR spectra of asteroids 354 Eleonora and 4 Vesta (Gaffey et al., 2015; Reddy & Sanchez, 2016). As can be seen, 354 Eleonora has a 1 μm absorption feature but no 2 μm absorption feature. However, 4 Vesta has clear absorptions at both 1 and 2 μm. These features are important for analyzing the compositions of these objects.

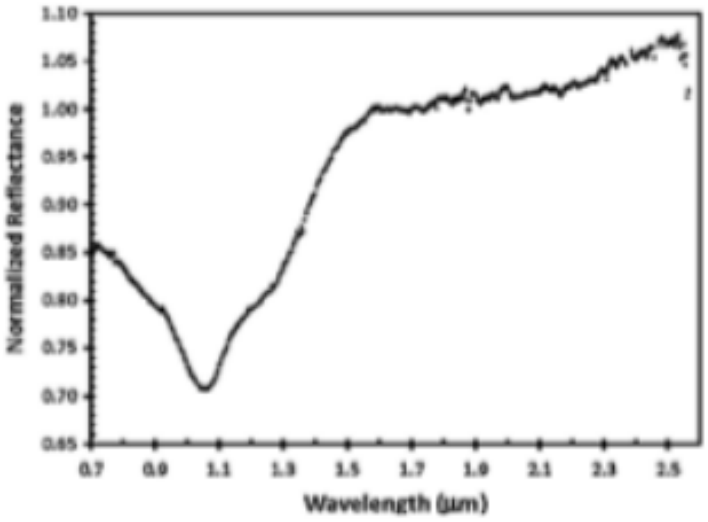

Figure 21: Vis/NIR spectrum of 354 Eleonora. Notice the absorption features at ~1 µm but not at ~2 µm (Gaffey et al., 2015).

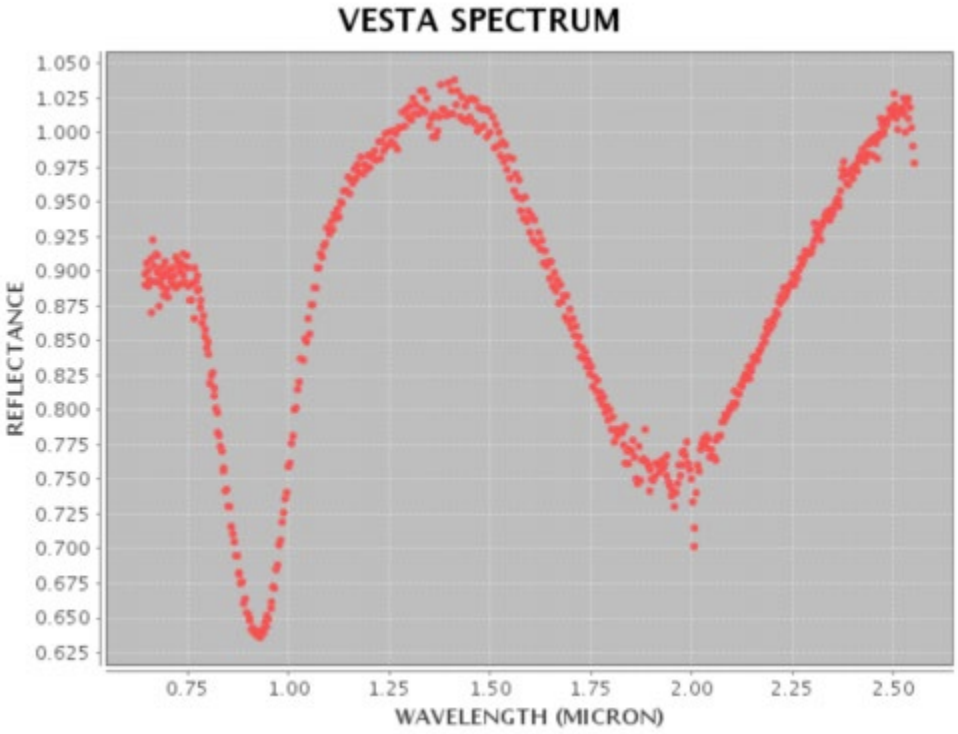

Figure 22: Vis/NIR spectrum of 4 Vesta. Notice the absorption features at both ~1 and ~2 µm (Reddy & Sanchez, 2016).

One of the most useful ways to classify an asteroid's spectrum is to compare the 1 μm vs 2 μm central wavelength of absorption. This tool can also be useful in determining asteroid surface composition. Gaffey et al. (1993) determined likely compositions of asteroids by comparing the 1 μm central wavelength of absorption vs the 1 and 2 μm band area ratio (BAR), as shown in Figures 23 and 24 below.

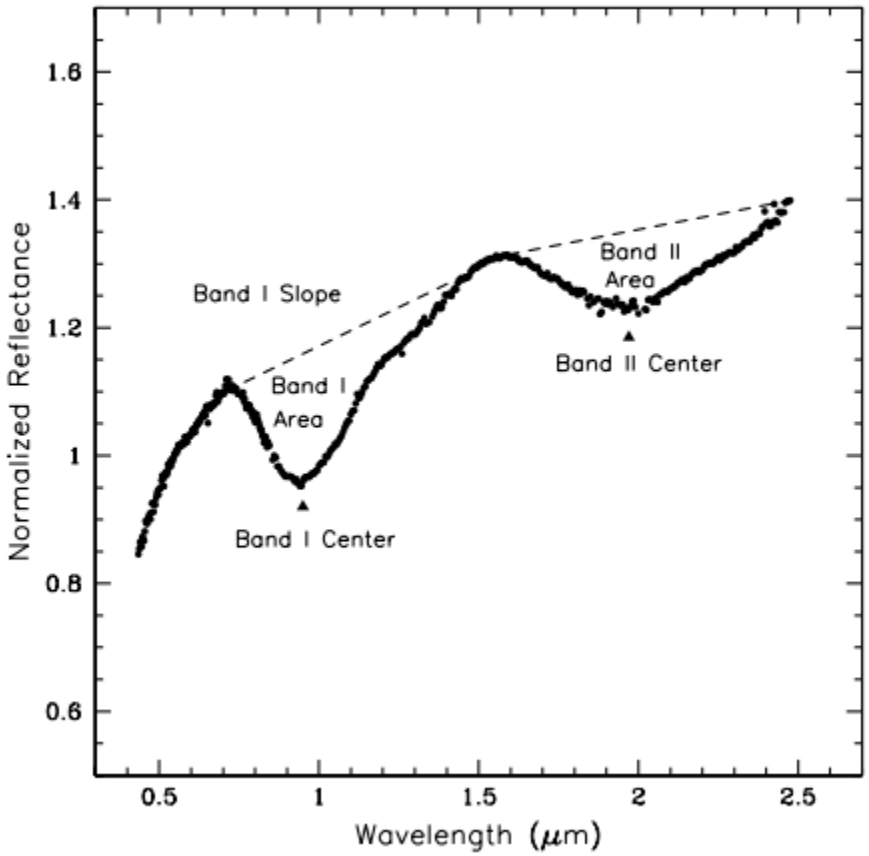

Figure 23: This figure shows the reflectance spectrum of an S-complex asteroid, with Band I and II centers and Band I and II areas labelled (Gaffey et al., 1993; Sanchez, 2012).

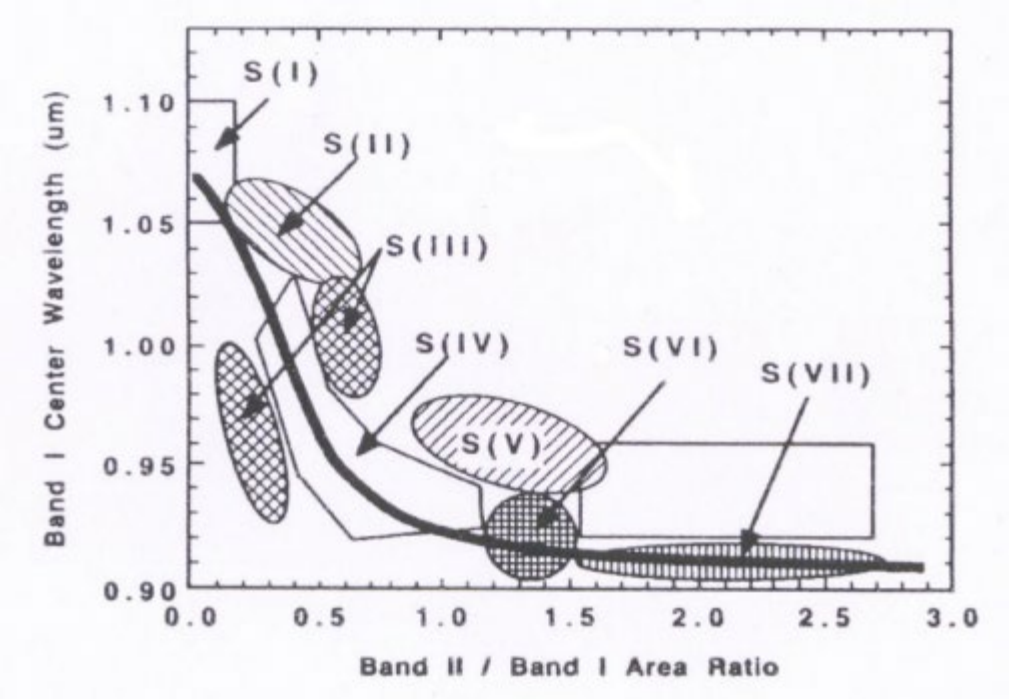

Figure 24: Gaffey S-complex asteroid figure (Gaffey et al., 1993).

Albedo:

When astronomers observe asteroids, the brightness of the target depends largely on four factors: the asteroid's distance from the Sun, phase angle of observation, the asteroid's surface area, and albedo.

It was mentioned before that asteroid surfaces of different compositions may have differing reflectances as a function of wavelength. The fraction of radiation incident upon an object that is reflected over a range of wavelengths is an important concept, and is known as albedo. The most commonly-listed albedo in the characterization of asteroids is geometric albedo over the visible wavelength range or p_v. Visible geometric albedo is defined as the ratio of an object's brightness compared to the brightness of flat, fully reflecting, diffusely scattering disk of the same cross-sectional area observed at zero phase angle (see Figure 14). Asteroid

visible geometric albedos range from ~3 – 50% (0.03 – 0.50), with an average at about 14%, or 0.14 (Masiero et al., 2014).

In the example above, the asteroid's distance from the Sun and phase angle of observation are straightforward to calculate given its orbital elements. Although surface area can vary depending on the asteroid's shape and surface features, one can arrive at a reasonable estimate. Albedo, however, can be highly variable, and two asteroids of the same size, distance from the Sun, and phase angle can differ greatly in brightness due to differences in albedo. If the albedo of one asteroid was 0.05 and the other was 0.15, then the asteroid with the higher albedo would reflect three times as much light and thus appear three times brighter – over one H magnitude lower – than the low albedo asteroid, all else considered equal.

If an asteroid had uniform composition on its entire surface, then one should observe a uniform spectrum as the asteroid rotates about its axis. However, from studies by Szabo et al. (2004) and Carvano et al. (2010), some asteroids may have non-uniform surface composition, and this thesis will explore this subject in greater depth.

Size and H Magnitude:

Most times, astronomers discovering asteroids will not know the object's diameter initially and will thus calculate its H magnitude first (for reference, the H magnitude is the visual magnitude of an object at 1 AU away and at zero phase angle). This calculation will give a size range depending on the asteroid's albedo. Currently, there are many asteroids today that do not have known sizes because their albedos are not known. Figure 25 shows the currently known distribution of asteroid semi-major axis with respect to H magnitude. Because telescopes used in asteroid discovery programs today have a fixed limiting magnitude of detection, there is a clear

bias toward discovering higher-albedo asteroids as semi-major axis increases, as asteroids with higher albedo will be detected from further distances than will lower-albedo asteroids.

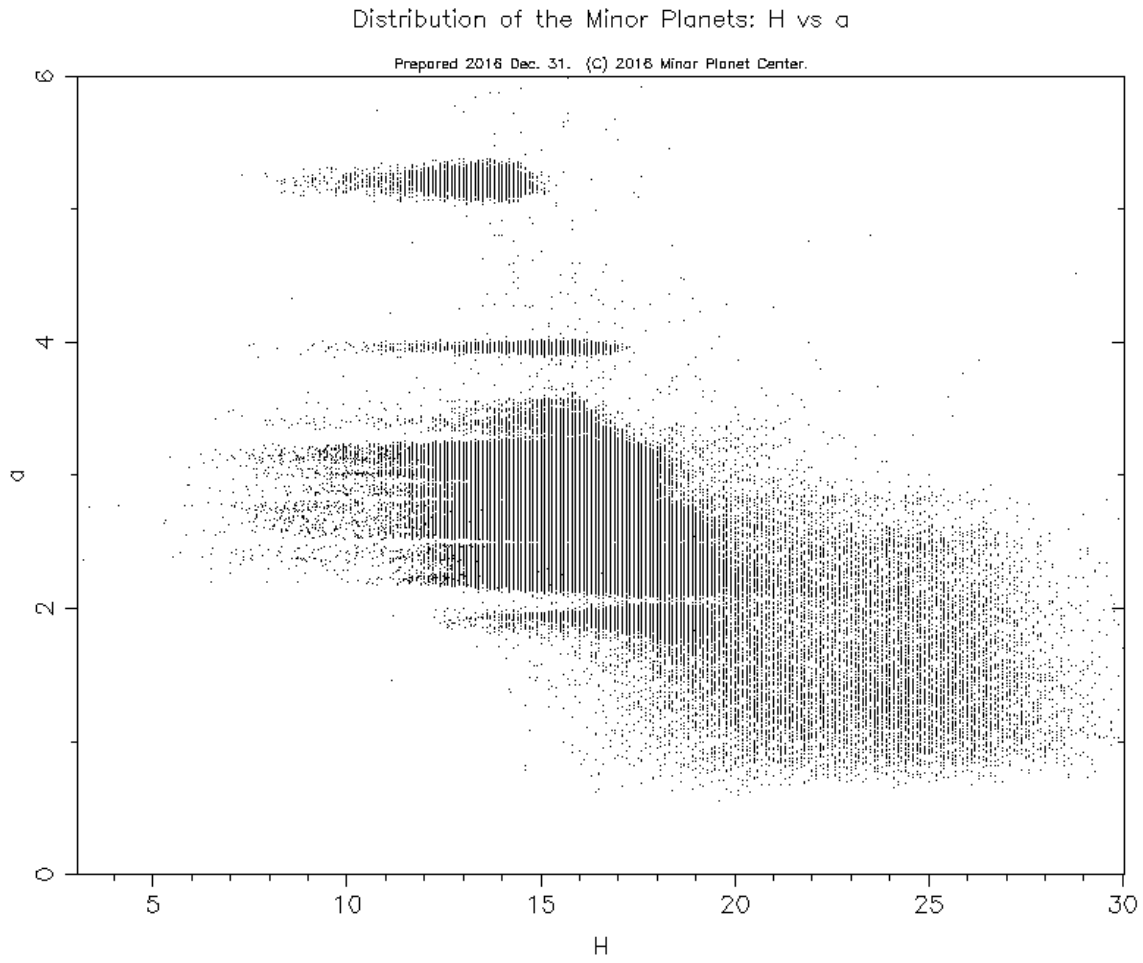

Figure 25: Distribution of the Minor Planets: semi-major axis vs H magnitude (IAU-H, 2018).

The size distribution of asteroids is still not well-constrained, both for Main Belt asteroids and NEAs, however, it is clear that there are many more smaller ones than larger ones (Masiero et al., 2014). As larger and better telescopes are used for discovery programs, more complete information will be uncovered. The Wide-Field Infrared Survey Explorer (WISE) and NEOWISE programs which have been discussed show that one of the benefits of this space-

based, mid-infrared (MIR, or thermal infrared (TIR)) observatory is that it was able to determine asteroid diameters to within 10%. This is because the MIR/TIR radiation emitted from asteroids is largely size-dependent, not albedo-dependent (Mainzer et al., 2011). Thus, asteroids that appeared brighter in the data were actually larger in reality and thus their sizes could be determined directly from MIR/TIR brightness because those two values were directly proportional.

However, prior to the Spitzer and WISE/NEOWISE missions, the primary method for determining an asteroid's size was to calculate its H magnitude. The H magnitude is the visual magnitude of an object at 1 AU away and at zero phase angle. H magnitude, of course, is highly dependent on an asteroid's albedo, which can range from 0.03 to above 0.50 (Masiero et al., 2014). If the asteroid's albedo is not known, as is usually the case especially for new discoveries, the calculated H magnitude will give a wide size range for the object. Figures 26 and 27 illustrate the known asteroids as a function of H magnitude and known NEAs as a function of H magnitude. The larger its H magnitude, the smaller the asteroid. Table 6 shows the H magnitude vs diameter vs albedo relationship for asteroids of various albedos (DeMeo & Carry, 2014), which makes it clear just how dependent on albedo these size determinations really are.

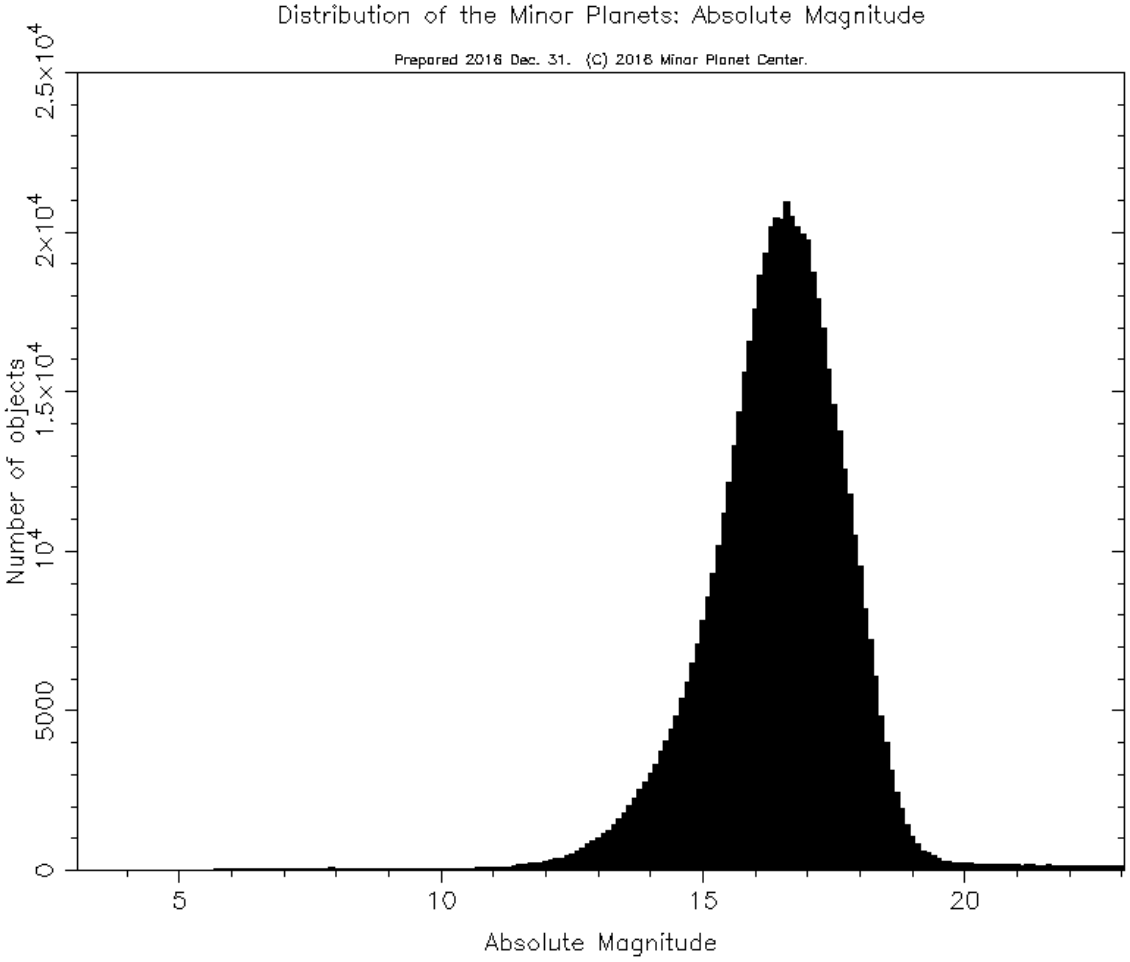

Figure 26: Distribution of the Minor Planets: number vs H magnitude for all asteroids (IAU-D, 2018).

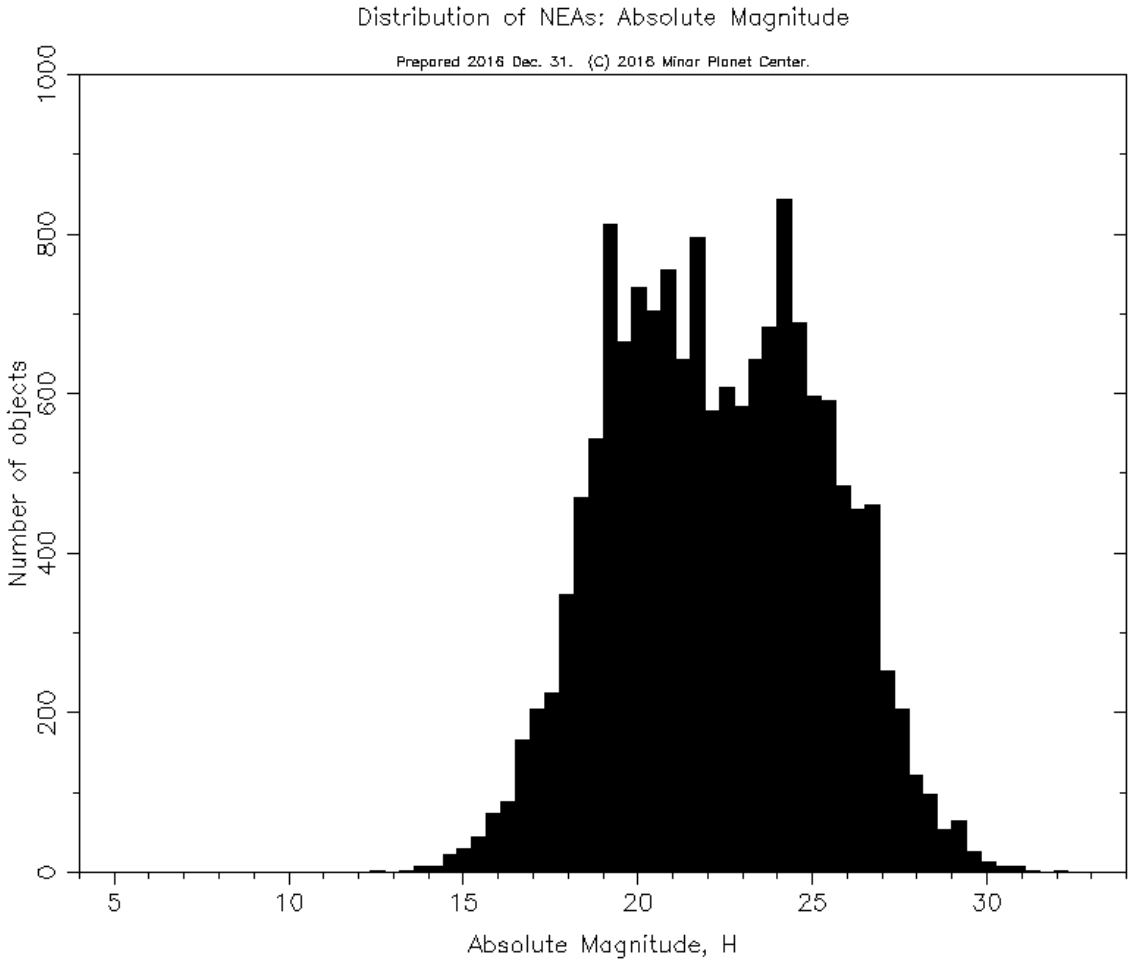

Figure 27: Distribution of the Minor Planets: absolute magnitude vs number for NEAs (IAU-I, 2018).

Taxonomic Class	Albedo	22	21	20	19	18	17	16	15	14	H Magnitude
A	0.20	0.118	0.188	0.297	0.471	0.746	1.183	1.875	2.972	4.710	
B	0.14	0.141	0.224	0.355	0.563	0.892	1.414	2.241	3.552	5.629	
C	0.06	0.216	0.342	0.543	0.860	1.363	2.160	3.423	5.426	8.599	
D	0.06	0.216	0.342	0.543	0.860	1.363	2.160	3.423	5.426	8.599	
K	0.14	0.141	0.224	0.355	0.563	0.892	1.414	2.241	3.552	5.629	
L	0.13	0.147	0.233	0.369	0.584	0.926	1.467	2.326	3.686	5.842	
Q	0.27	0.102	0.161	0.256	0.405	0.642	1.018	1.614	2.558	4.054	
S	0.23	0.110	0.175	0.277	0.439	0.696	1.103	1.748	2.771	4.392	
V	0.35	0.089	0.142	0.225	0.356	0.564	0.894	1.417	2.246	3.560	Diameter (km)

Table 6: H magnitude vs diameter as a function of albedo relationship for asteroids. Average albedo values from DeMeo and Carry (2013) were utilized. The equation to calculate diameter is $D = 1{,}329(10^{-0.2H}/\sqrt{(p_v)})$ km from Mainzer et al. (2011).

Biases certainly exist in the asteroid size dataset. First, most of the smaller asteroids discovered are NEAs simply because they would be too dim to find in the Main Belt with our current observational capabilities. Smaller asteroids likely exist as a population in the Main Belt as well. Second, even though the largest of the asteroids have probably been discovered, the drop off of asteroids with H magnitude > 17 is probably not indicative of reality either. Again, these asteroids likely have not been discovered yet. Finding these smaller asteroids will dramatically increase the known asteroid population.

Space Weathering:

Different spectral slopes may be due to an inherently different surface composition (and therefore albedo) or due to phase angle effects, but also may be due in part to a process called *space weathering*. Space weathering is the process of the space environment affecting the surface of an object. This concept actually first came about when samples of the Lunar surface were returned during the Apollo missions in the 1960s and 1970s. It was originally thought that space weathering could explain the difference in spectra between relatively neutral-sloped

ordinary chondrites and red-sloped S-type asteroids, as ordinary chondrites are the most common meteorites found and S-types were thought to be abundant. Lunar samples showed the same red spectral slope thought to be due to space weathering, so it seemed plausible this could happen to asteroids too.

Space weathering occurs on all objects in the Solar System without a protective atmosphere, and may increase spectral slope, reduce spectral absorption features, and lower albedo (Lantz et al., 2018). It is still a poorly-understood process, and it is unclear whether the spectral slope diversity in featureless, dark (low-albedo) asteroids is due to inherently different composition (and possibly origin) or due to space weathering effects.

As straightforward as it seems, Gaffey (2010) studied the surfaces of 243 Ida, 433 Eros, and the Moon, and found different band depth/albedo and spectral slope/albedo relationships for all three. On the Lunar surface, space weathering weakens absorption features, lowers albedo, and reddens the spectrum. This spectral reddening is likely caused by micrometeorite impacts vaporizing material on the surface and creating nanophase iron particles called sub-microscopic metallic iron (SMFe). These have been shown to darken and redden spectra in both models and laboratory experiments (Bus & Binzel, 2002B; Sanchez et al, 2012). The problem arises when meteoritic regolith breccias are studied. In them, spectrally significant space weathering is not observed. In addition, space weathering can mimic the appearance of phase reddening, which can complicate spectral analyses (Sanchez et al, 2012). This effect is discussed more in the section on phase angle effects.

For the Moon's surface, it was found that band depth decreased, albedo decreased, and spectral slope increased. For 243 Ida, band depth decreased, albedo did not change, and spectral slope increased. For 433 Eros, band depth remained constant, albedo decreased, and spectral

slope remained constant (Gaffey, 2010). Due to all these different effects, it can be concluded that space weathering probably is not due to a single type of process.

However, space weathering *may* be responsible for the diversity of slopes in S- and Q-type asteroids (Binzel et al., 2004). Both types of asteroids have the characteristic 1 and 2 μm absorption bands, but S-types have a moderately red spectral slope (5 – 12%/10^3 Å) whereas Q-types have a much more neutral spectral slope. Thus, space weathering may be the reason for the distribution of S- and Q-type asteroids, with S-types typically being larger and located in the Main Belt and Q-types typically being smaller, located in near-Earth space, and having "fresh" surfaces exposed due to impacts and collisional evolution (one must take into account observational bias and incomplete discovery statistics though; there *may* be many Q-types in the Main Belt that are too small to be discovered currently). This hypothesis is further strengthened when the meteorite collection is examined. Ordinary chondrite meteorites are the most common type and have neutral spectral slopes, very similar to Q-type asteroids. Thus, Q-types are perhaps the immediate parent bodies of ordinary chondrites, and S-types may be the parent bodies of Q-types having been collisionally disrupted and exposing fresh surfaces (Binzel et al., 2004). All in all, the band depth-albedo-spectral slope relationship inconsistencies are still problematic enough to prevent scientists from drawing significant conclusions about space weathering.

Dynamical Evolution of Asteroids:

So, how do asteroids from the Main Belt migrate into near-Earth space? Before answering this question, we must first explore properties of the Main Belt in more detail.

Hirayama Families:

Resonances and Kirkwood Gaps have already been discussed, but these are not the only way asteroids in the Main Belt are distributed. In 1918, the Japanese astronomer Kiyotsugu Hirayama discovered groups of asteroids with very similar orbital elements (Hirayama, 1918). He called these "asteroid families" or "Hirayama families." He theorized that these families are remnants of larger asteroids which were subjected to catastrophic collisions. These families can be identified by observing many asteroids grouped together with similar values in orbital-element space (Zappala et al, 1990).

The method used for determining asteroid families from values in orbital element-space is called Hierarchical Cluster Modeling (HCM) (Zappala et al, 1990). The age of the asteroid family – and thus probably how long ago the catastrophic collision occurred – is determined by when the family joins back as a single point. This location is then the location of the parent body which suffered the catastrophic collision (Zappala, 1995; Zappala et al, 2002; Bendjoya & Zappala, 2002). Once disrupted, these individual smaller asteroids are then subjected to the Solar System environment. Thus, individual members of asteroid families have smaller exposure ages than the age of the parent body, which according to theories of Solar System formation should be close to the age of the Solar System itself (Zappala, 1995; Zappala et al, 2002; Bendjoya & Zappala, 2002). Asteroid families are also useful for studying Solar System dynamics and non-gravitational forces such as Yarkovsky and YORP effects.

With the advent of modern computing power and the exponential increase in discovered asteroids, more and more asteroid families are being discovered. Zappala (1990) studied 4,100 asteroids and identified 21 asteroid families. Monthe-Diniz et al. (2005) combined SMASS II and S3OS2 data – resulting in a 12,487-asteroid sample size – to update the 21 known families,

determining that only about one-third of the families could be distinguished from the background asteroid population. For Main Belt asteroids, identifying a family assumes that smaller members will travel further away from the initial impact and larger members will stay closer (Zappala et al., 2002). However, they should all share similar orbital elements. But there are often "interlopers" – asteroids which are not part of the family but happen to have similar orbital elements. Interlopers may be singled out if they have different taxonomies, but it is not impossible for different pieces of a parent body to have different taxonomies, or interlopers to have a similar taxonomy to asteroid family members. An important concept to remember is that asteroid taxonomy does not indicate composition; taxonomies simply group asteroids based on features that their spectra indicate. Different taxonomies may have different compositions, or may have similar compositions, and similar taxonomies may have wildly different compositions. This makes positive identification of asteroid family members an arduous task.

Currently, 122 asteroid families are known (Nesvorny et al., 2015). Families may include just a few asteroids or may consist of many thousands of asteroids. Current and future surveys will undoubtedly uncover more families, and enable a better picture of asteroid families and their relation to the next topic – collisional evolution.

Collisional Evolution:

Collisions are the proverbial "mixing spoon" of the Main Belt; they create Hirayama families and spread asteroidal material throughout the region. Collisional evolution may be the reason for the aforementioned mass deficit of the Main Belt, but this is still theoretical conjecture and may not be the only factor at play. Planetary migrations early in Solar System history may

have played a larger factor (Walsh et al., 2011). Nonetheless, collisional evolution has played an important role in the evolution of the Main Belt and the creation of NEAs (Bottke et al., 2015).

Collisions in the Main Belt have three primary consequences: they eject material from the Main Belt by sending it into different orbits (there will be more on this subject later), they decrease the mean sizes of asteroids in the Main Belt, and they create more and more smaller asteroids. A collision may simply produce a crater with some ejected debris, as asteroids have very low surface gravity, or it may cause the complete breakup of an asteroid (Bottke et al., 2015). Collisions can also resurface the top layers of asteroids, exposing fresher, less space-weathered material. This can be detected from observations, as the older, weathered material that has been subjected to the radiation environment and micrometeorites will have different spectral properties and albedo than the fresher material. In fact, a physical collision need not even occur; a close pass may be enough to overturn the top few centimeters of the asteroid's surface (Richardson et al., 1998; Pravec & Harris, 2000). Recall that vis/NIR observations cannot penetrate deeper that these top few centimeters into an asteroid.

Collisions can eject material into a wide range of new orbits and rotation axes. These newly-created or newly-disturbed asteroids can in turn be affected by non-gravitational forces. Non-gravitational forces include interactions with the Solar radiation environment and absorption and re-emission of radiation. The first one we will explore is the Yarkovsky Effect.

Yarkovsky Effect:

As interesting as the Yarkovsky effect is, it was not discovered by an astronomer or a physicist. Rather, the Polish civil engineer Ivan Osipovich Yarkovsky proposed it around the year 1900 (Beekman, 2005). The Yarkovsky effect occurs due to the fact that photons carry

momentum and can exert a force on an object. The first case is the diurnal Yarkovsky effect. As an asteroid is rotating on its axis, one side of it is illuminated by the Sun and is being heated. The surface of the asteroid has thermal inertia, so it will take some time to heat up when first illuminated and will take some time to cool down once illumination stops. The asteroid will re-emit some energy received from the Sun as thermal radiation. However, for an object rotating counter-clockwise (the most common direction of rotation in the Solar System) the hottest point on the object will be in the early afternoon. Thus, this re-emitted thermal radiation imparts a force on the asteroid and increasing its semi-major axis. If the object rotates clockwise, then from this effect its semi-major axis will decrease (Farinella et al., 1998; Bottke et al., 2006).

There is also a seasonal Yarkovsky effect, which occurs over the course of an object's orbit. As an asteroid makes its way around the Sun, the recent "day" side will continually move toward the *direction* the asteroid is revolving. This causes the re-emitted thermal radiation to impart a force opposite to the asteroid's revolution, and thus decrease its semi-major axis. This effect is only significant if the diurnal Yarkovsky effect is small enough. The seasonal Yarkovsky effect increases as axial tilt increases (Bottke et al., 2006).

The Yarkovsky Effect is significant because it can change the semi-major axes of asteroids' orbits, especially smaller ones created from collisions. If the collision occurred near a secular or mean-motion resonance, then over time the Yarkovsky effect may impart enough force to bring the asteroid *into* that resonance.

Migration into Near-Earth Space:

As covered before, Jupiter is the largest and most massive planet in the Solar System, and its gravitational influence can be observed in the Main Belt through Kirkwood Gaps, which

correspond to semi-major axes that have small whole integer mean-motion resonances with Jupiter's orbital period. The most notable mean-motion resonances in the Main Belt are the 3:1 and 5:2 resonances, although there are many more, including some that have a stabilizing effect on orbits (Bottke et al., 2002). Orbital diagrams of the Main Belt are shown in Figures 28 and 29, and they include major mean-motion resonances. In addition, secular resonances which depend on the alignment of the arguments of perihelia of two objects exist in the Main Belt (Bottke et al., 2002). A good example is the υ_6 resonance. These resonances are mostly devoid of asteroids, but it has been shown that a combination of orbital dispersion from collisional disruptions and non-gravitational forces such as the Yarkovsky effect can drive some asteroids into these resonances (Farinella et al., 1998; Binzel et al., 2004). Once in a resonance, the eccentricity of an asteroid will be increased through repeated gravitational interactions with Jupiter (or Saturn). Eventually, its eccentricity will be large enough so that it crosses the orbit of one or more terrestrial planets. A close encounter with one of these planets can perturb its orbit and effectively remove it from that resonance (Pater & Lissauser, 2010). Thus, the Main Belt asteroid has now become a near-Earth asteroid.

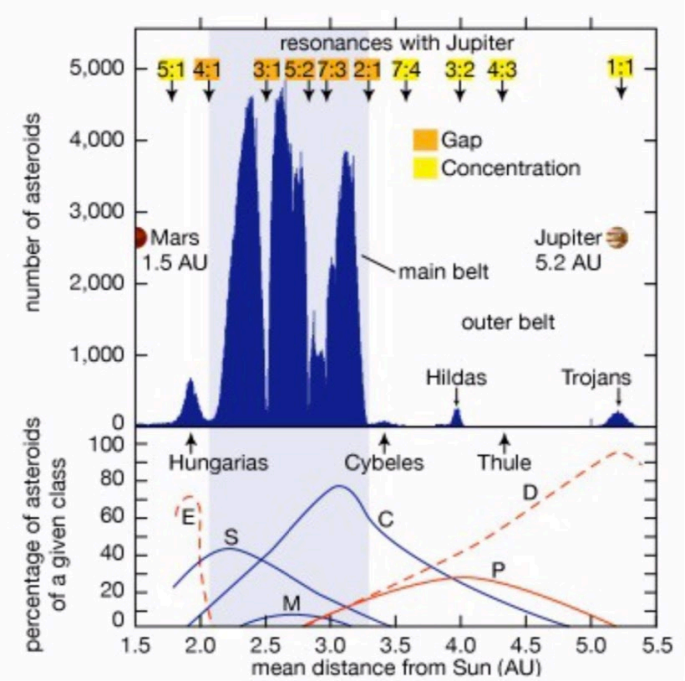

Figure 28: The currently-known structure of the Main Belt. Major resonances, planets, and populations are shown. The majority of mass in the Main Belt exists from ~2.0 – 3.5 AU. (www.brittannica.com/science/asteroid).

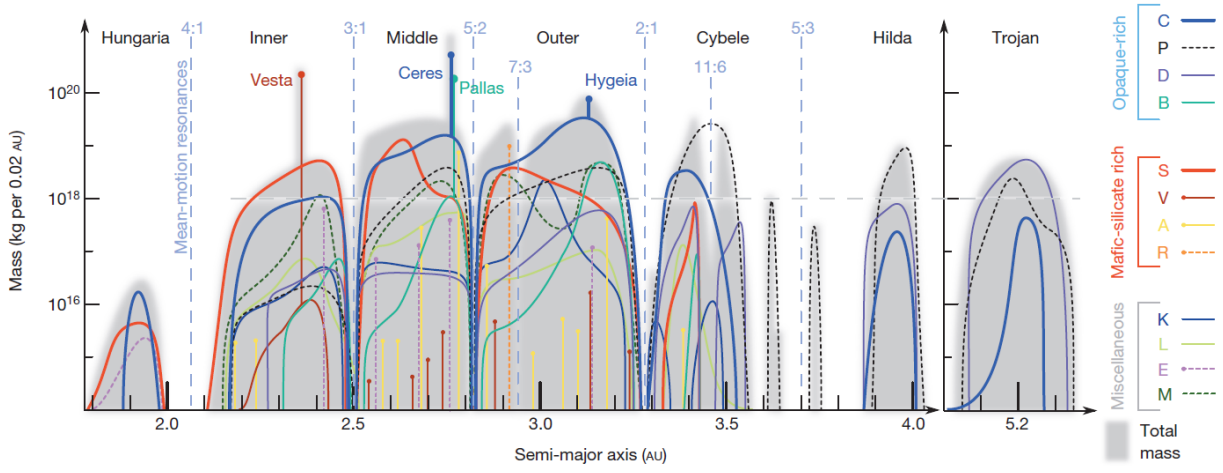

Figure 29: The compositional mass distribution of the Main Belt built from results of the SDSS MOC (DeMeo & Carry, 2014).

Many originally believed the majority of NEAs were extinct comet nuclei (Wetherill, 1976), but theory and computational methods have shed light on their origins. Wetherill (1979) postulated that resonances in the Main Belt could increase the eccentricities of asteroids and force them into planet-crossing orbits. Using Monte-Carlo methods, he also hypothesized that these resonances were resupplied by collisions of asteroids near these resonances, with their debris migrating into these resonances (Wetherill, 1979, 1985; Gladman et al., 1997; Bottke et al., 2002), which is consistent with our current understanding.

Since NEAs exist and have lifetimes of only ~10 – 15 Myr in near-Earth space, they must be resupplied from elsewhere, most likely the Main Belt and the aforementioned Jupiter-Family comet population (Gladman et al., 1997; DeMeo & Binzel, 2008). Ancient craters exist on both the Earth-Moon system and other terrestrial planets, so we know that objects have been migrating into near-Earth orbits for most of the age of the Solar System (Shoemaker, 1983; Bottke et al., 2002). Scientists have extensively used computational methods to numerically model the evolution of SSSBs (Farinella et al., 1994; Levison & Duncan, 1994; Gladman et al., 1997; Bottke et al., 2002; Greenstreet et al., 2012). The development of symplectic integrators have made these computational modeling efforts much more efficient.

One of the seminal papers in the field of SSSB computational dynamics is primarily authored by William Bottke (Bottke et al., 2002). In this paper, they modeled the dynamics of SSSBs in four regions of the Main Belt: the υ_6 secular resonance, the 3:1 mean motion resonance, the Mars-crosser population, and the outer Main Belt population, and one region beyond the Main Belt called the Jupiter-family comet population. These reservoirs are shown schematically in Figure 30. This was a continuation of work from Bottke et al. (2000a), in which

only three NEA reservoirs were considered (υ_6, 3:1, and Mars-crossers). Objects within these resonances can have their eccentricities pumped up so that their orbits begin to intersect Mars' orbit, then Earth's, then perhaps even Venus's or Mercury's (Bottke et al., 2002). A list of mechanisms causing near-Earth migrations is also listed in Table 7 and the resulting dynamical classes are shown in Table 8. The orbital elements of the NEO determine the class of NEO to which it belongs.

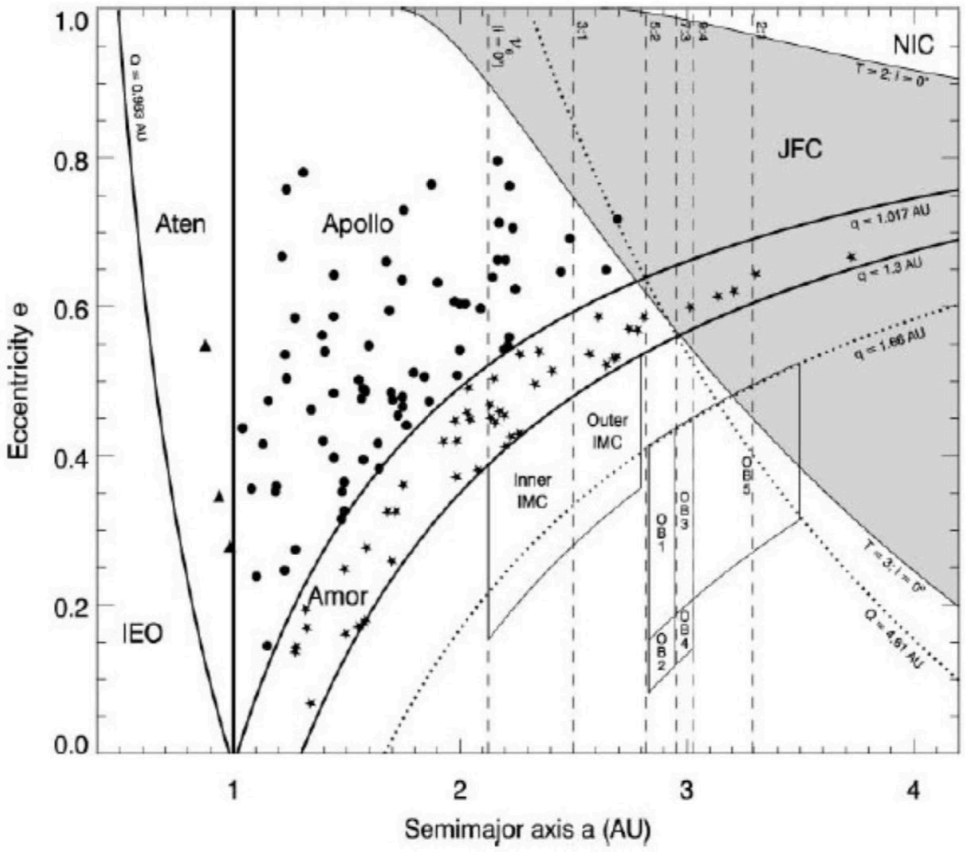

Figure 30: Eccentricity vs semi-major axis graph of the inner Solar System (Bottke et al., 2002). Different dynamical classes of NEOs are defined as well as the different source regions for NEOs. The Jovian Tisserand Parameter lines are also defined, and are useful for dynamically discriminating between asteroids, Jupiter-family comets, and Nearly-isotropic comets. Acronyms: NIC (Nearly-isotropic comets), JFC (Jupiter-family comets), OB (outer Main Belt), IMC (intermediate-source Mars-crossers), IEO (Interior-to-Earth objects).

Source Region	a range (AU)	e range	i range (degrees)	Mean time in NEA Region (Myr)	% Attaining a < 2 AU	Migration Mechanisms
3:1	2.48 < a < 2.52	< 0.35	< 15	2.2	38	Mean-motion resonance with Jupiter pumps up eccentricity
υ6	~2 < a < 2.4	< 0.1	0 < i < 15	6.5	70	Secular resonance with Saturn, peroidic e oscillations increase eccentricity
MC	2.06 < a < 2.48; 2.52 < a < 2.8	0 < e < ~0.5	0 < i < 15	3.85	53	Mean-motion resonances with Mars, 3-body Jupiter-asteroid-Sun interactions
OMB	2.8 < a < 3.5	X	0 < i < 15	0.14	6	5:2, 7:3, 9:4, 2:1 mean-motion resonaces, 3-body Jupiter-asteroid-Sun interactions
JFC	< 7.4	X	X	X	X	Terrestrial planet encounters, non-gravitational forces

Table 7: Orbital properties and migration mechanisms of NEO reservoirs compiled from Bottke et al. (2002). The JFC source region, as can be seen, required different dynamical criteria to define it than the other source regions. JFCs are defined as having Jovian Tisserand parameters of $2 < T_J < 3$. Acronyms: MC (Mars-crossers), OMB (outer Main Belt), JFC (Jupiter-family comets).

NEO Class	a (AU)	Q (AU)	q (AU)
Amor	> 1.017	N/A	1.017 < q < 1.3
Apollo	> 1	N/A	< 1.017
Aten	< 1	> 0.983	N/A
Apohele/Atira/IEO	< 0.983	< 0.983	N/A

Table 8: Dynamical classes of NEOs with their defining orbital characteristics. Acronyms: IEO (Interior-to-Earth objects).

So, the four classes of NEOs are: Amors, Apollos, Atens, and Apoheles/Atiras (Bottke et al., 2002; Greenstreet et al., 2012). Apoheles/Atiras may also be referred to as Interior-to-Earth objects (IEOs). Amors have perihelia less than 1.3 AU but greater than Earth's aphelion at 1.017 AU. Apollos have perihelia less than 1.017 AU but semi-major axis greater than 1 AU. Atens have aphelia greater than Earth's perihelion of 0.983 AU, but semi-major axis less than 1 AU. Atiras/Apoheles have aphelia less than 0.983 AU. Thus, Apollos and Atens have orbits that could cross Earth's orbit. In addition, Greenstreet et al. (2012) proposed another class of objects dubbed "Vatiras" which have orbits entirely interior to Venus's orbit.

In addition to these resonances, objects can be influenced by Kozai-Lidov interactions, in which an object in a two-body system – for example the Sun and an asteroid – is perturbed by a distant third body – for example Jupiter – causing the object's argument of perihelion to oscillate around a certain value, leading to an exchange between the object's eccentricity and inclination (Kozai, 1962). Bottke et al. (2002) found that the majority of NEAs originate in the inner Main Belt, and those that originate in the outer Main Belt tend to have higher perihelia. Only 6 ± 4% of NEOs from the simulations of Bottke et al. (2002) came from the Jupiter family region, much less than previous authors such as Wetherill (1976) indicated. Bottke et al. (2002), however, did

not include nearly-isotropic comets (NICs) in their simulations, so the cometary contribution to the NEO population may be higher, especially since it has been suggested that 10 – 30% of planetary impacts come from NICs (Shoemaker, 1983; Fernandez & Ip, 1991).

Rotation:

It was thought that asteroids rotate, and rotation can contribute to the Yarkovsky effect, but rotation periods of asteroids were not well-characterized until recently. Still, very few asteroids have measured rotation periods (Warner et al., 2009). An asteroid's rotation period is determined by creating a light curve over a short period of time. If the asteroid is non-spherical, as most asteroids are, or has a non-uniform albedo, the light reflected as a function of time will vary. Radar observations have shown most asteroids observed have *relatively* uniform surface albedo, so any change in brightness is probably due a non-spherical shape. From there the asteroid's rotation period can be determined by identifying key features that repeat at a specific frequency. Observations are usually performed over several nights.

Pravec and Harris (2000) analyzed the distribution of asteroid rotation periods vs size. They found many fast and slow rotators among the population they studied, especially below ~10 km size, which were mainly NEAs. Many slow rotators had periods of < 0.8 revolutions per day, and fast rotators had periods of > 7 revolutions per day. They also found a 2.2 hour rotation period "barrier" among asteroids with H < 22 magnitude and that fast rotators also had more spheroidal shapes. Most of the asteroids with H < 22 had rotational light curve amplitudes of ~0.5 – 1.0 magnitudes. They concluded that most asteroids larger than ~300 m are likely loosely-bound "rubble piles" while smaller fast-rotators are likely to be monolithic or close to it. Also, nearly half of all fast-rotators were found to be binary systems, meaning the original

asteroid's rotation period was spun-up so that loosely-bound fragments flung off or from a close encounter with a planet. It is theorized that rotational spin-up can cause an asteroid to be active (Jewitt, 2012). A graph of their results is shown in Figure 31. How this process occurs will be covered in the next couple sections.

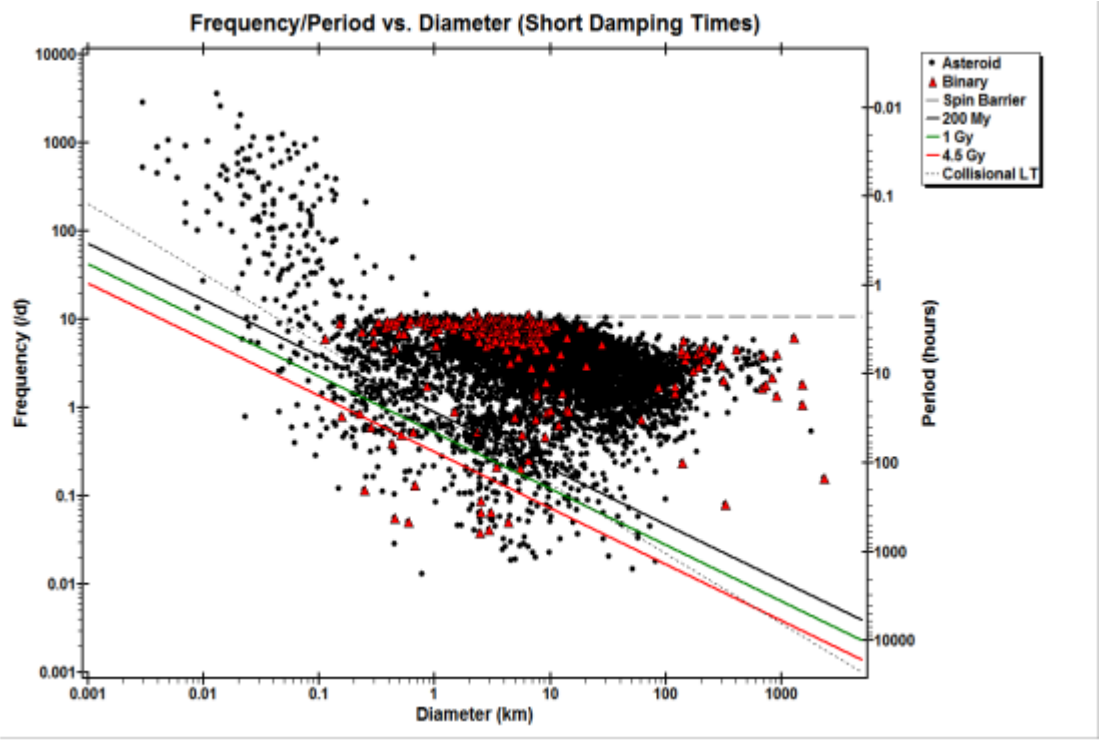

Figure 31: Graph of asteroid rotation periods vs diameters (Warner et al., 2009). Notice the ~2.2 hour "barrier" for asteroids larger than ~300 m.

Over the past few decades, rotation periods of asteroids have become more well-characterized, aided by more cost-effective sub-1 m telescopes and modeling techniques. Warner et al. (2009) created the Asteroid Light Curve Database (LCDB) with rotation periods for ~7,500 asteroids. Wasczak et al. (2015) studied an additional ~54,000 asteroids and determined rotation periods for ~8,300 of them. All in all, ~15,800 asteroids have known

rotation periods. This sounds optimistic, but actually is just ~2% of the known 800,000+ asteroids.

Asteroid rotation is relevant to this thesis because in order to detect any non-homogeneity in spectrophotometry, the asteroid's rotation period must first be determined. That way, one will know over what periods of time to take spectrophotometric observations.

YORP Effect:

An asteroid's rotation period is not static throughout time. Collisions can alter the rotation period and axis of rotation for an asteroid, and can create new asteroids from the impact event with unique rotation periods of their own. A key non-gravitational effect influences rotation period as well. It is called the Yarkovsky-O'Keefe-Radzievski-Paddack (YORP) effect and has the same physical mechanism as the Yarkovsky effect: the fact that photons carry momentum. However, in the YORP effect, it is the asteroid's non-uniform surface from which radiation is re-emitted that actually causes a torque on the object, thus changing its period of rotation and possibly even its axis of rotation (Rubincam, 2000).

The YORP effect can spin up asteroids to the point where their surfaces begin to slough off. This can cause the asteroid to lose mass. Many of the fast rotators and binary asteroids are thought to be asteroids that have undergone this process (Rubincam & Paddock, 2007). In addition, this sloughing off of mass could be a cause for some of the newly-discovered active asteroids (Jewitt, 2012).

Additionally, the YORP effect can create asteroids that have multiple axes of rotation and appear to "tumble" throughout their orbits (Rubincam & Paddock, 2007). This can complicate finding the period(s) of an asteroid's rotation.

Multiple-Asteroid Systems:

Asteroids with moons or binary asteroids are appearing to be more and more commonplace throughout the Solar System. In fact, the number of known NEAs with moons or that are binary has increased by a factor of more than four since 2005; this figure has doubled for Main Belt asteroids (Margot et al., 2015). It is thought that collisions and the YORP effect are the chief causes of binary asteroid systems. A collision may eject material, or the YORP effect may spin up an asteroid so much that it loses cohesion. Either way, the debris then may coalesce into a moon or a ring. Margot et al. (2002) found that in a survey of NEA binary systems, the primary (more massive) object was rotating with a period near the limits of its cohesion, giving strong evidence for this theory. A close planetary encounter could also cause objects rotating near their cohesion limit to break up due to tidal effects.

Binary asteroids are interesting to study because they can allow a direct mass measurement of the system, which is otherwise not possible without either a spacecraft flyby or close planetary encounter. Knowledge about the mass of an asteroid gives clues as to its internal composition and structure. This information is interesting from a scientific perspective, but also is relevant for those working in planetary defense and extraterrestrial resources applications.

Asteroid Shapes:

An asteroid's light curve gives its rotation period, but by examining its amplitude minima and maxima and the uniformity of the curve, the elongation of the asteroid can be determined. More observations lead to a light curve with less uncertainty and a more tightly-constrained elongation. Currently, only several hundred asteroids have enough data for a reasonable shape

model to be produced using the light curve method. However, radar observations can give detailed shape models with high resolution (Benner et al., 2015). In the case of NEAs, however, the object must pass very close to Earth for radar to be an effective method.

Asteroid End States:

After their injection into near-Earth space, NEAs have three possible end states: ejection from the Solar System, impact with a terrestrial planet, and impact with the Sun. Simulations by Farinella et al. (1994) have shown that impact with the Sun is actually the most likely outcome for a NEA, followed by ejection from the Solar System, then lastly collision with a terrestrial planet. The lifetimes of NEAs are astronomically short; half-lives in near-Earth space are estimated to be only ~10 – 15 million years (Bottke et al., 2002; DeMeo & Binzel, 2008). So, an asteroid can orbit the Sun for billions of years in the Main Belt, but once perturbed into near-Earth space, it is in its death spiral.

Summary:

This literature review could have gone deeper into any of the above topics, however, its purpose was to give a general scope of subjects relevant to this thesis, which center around NEA photometry, spectroscopy, asteroid data collection efforts, taxonomies, the Sloan Digital Sky Survey Moving Objects Catalog and its questionable reliability as a source of asteroid photometry, and the physical and dynamical evolution or asteroids. The next sections will discuss the data analysis, results, conclusions, and future work of this research.

CHAPTER VI

ANALYSIS AND DISCUSSION

Analysis

Sloan Digital Sky Survey Analysis

2059 Baboquivari and 96744 (1999 OW3) were observed by SDSS once each. 2059 Baboquivari was observed on 30 March 2003 and 96744 (1999 OW3) on 21 October 2005. By converting their g, r, i, and z calibrated magnitudes in the MOC4 into reflectances, the following photometric spectra were constructed.

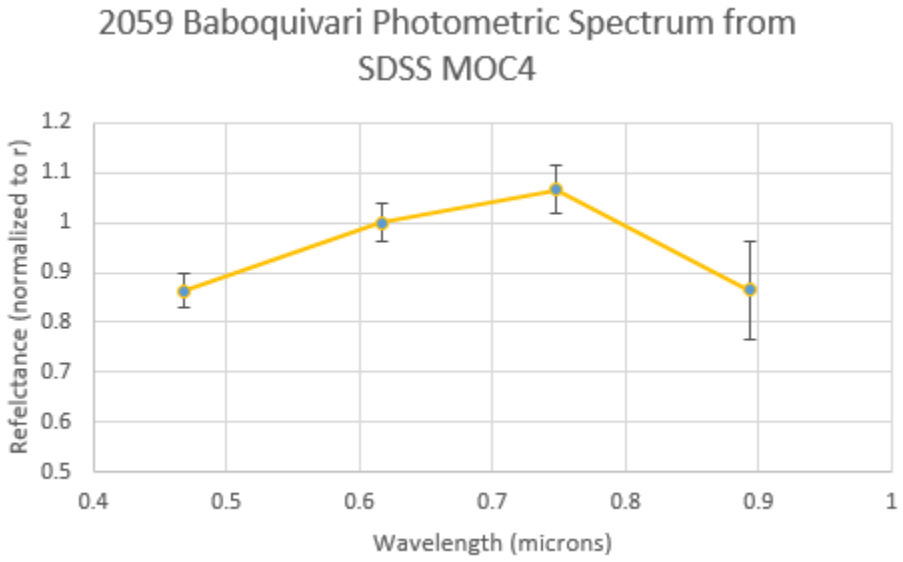

Figure 32: Photometric spectrum built from calibrated magnitudes of 2059 Baboquivari in SDSS MOC4.

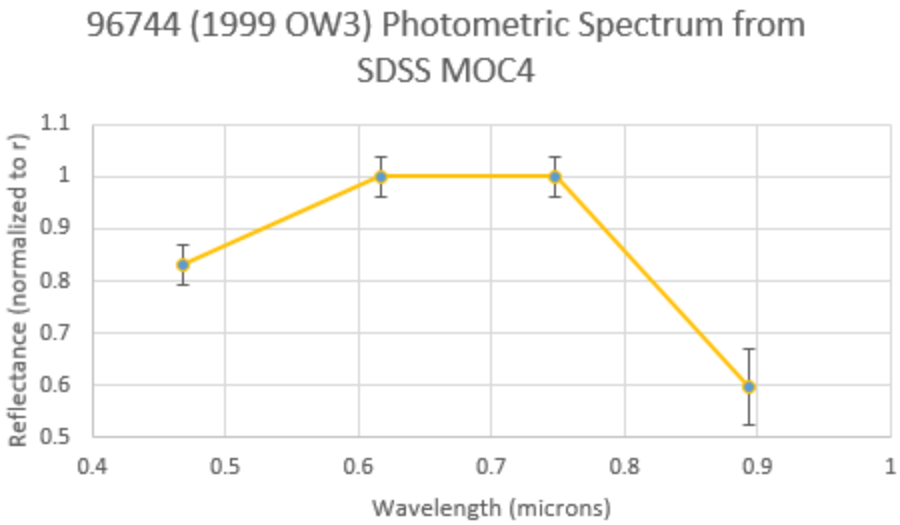

Figure 33: Photometric spectrum of 96744 (1999 OW3) calculated from calibrated magnitudes found in SDSS MOC4.

2059 Baboquivari			
Filter	Wavelength (microns)	Reflectance	Error
g	0.4686	0.863	0.034
r	0.6165	1.000	0.039
i	0.7481	1.067	0.049
z	0.8931	0.865	0.098

96744 (1999 OW3)			
Filter	Wavelength (microns)	Reflectance	Error
g	0.4686	0.832	0.038
r	0.6165	1.000	0.039
i	0.7481	1.000	0.039
z	0.8931	0.598	0.073

Table 9: Table of filters, reflectances, and associated errors for 2059 Baboquivari and 96744 (1999 OW3) calculated from calibrated magnitudes for each object in the SDSS MOC4 database.

It is obvious from these reflectance graphs that both 2059 Baboquivari and 96744 (1999 OW3) have 1 μm absorption features. 2059 Baboquivari's taxonomy has not been determined, but 96744 (1999 OW3) was assigned to the V-type taxonomy by Carry et al. (2016). This assignment was done based only on its spectrophotometry in the MOC4. Thus, it is good to know an independent construction of 96744 (1999 OW3)'s photometric spectrum based on the

same data leads to an agreeable result, and the same goes for 2059 Baboquivari. These reflectances will be the "baseline" to which independent observations of these two NEAs will be compared.

Spectrophotometric Observations

2059 Baboquivari and 96744 (1999 OW3) were observed using the Yale/SMARTS 1.0 m telescope at CTIO in October/November 2019 and January 2020, respectively. This telescope is a f/10.5 reflector. The 2048x2048-pixel CCD used 4x4 binning (which means the CCD operates as 512x512), and at -30 degrees Celsius has dark current of 0.2 electrons/pixel/second. It has a scale of 1.05 arcseconds/pixel, and a 9'x9' field-of-view. Tables 10 and 11 show the orbital and observational data for each object.

Object	Semi-major axis (AU)	Eccentricity	Inclination (degrees)	Perihelion (AU)	Aphelion (AU)	Jovian Tisserand Parameter	NEO Dynamical Class
2059 Baboquivari	2.644	0.531	11.014	1.240	4.048	3.154	Amor
96744 (1999 OW3)	2.092	0.780	34.945	0.460	3.724	3.138	Apollo

Table 10: Orbital data for 2059 Baboquivari and 96744 (1999 OW3).

Object	Date (Calendar)	Date (Julian)	Right Ascension	Declination	Sun-Object Distance (AU)	Earth-Object Distance (AU)	Phase Angle (degrees)	Airmass	Apparent V Magnitude
2059 Baboquivari	31 October 2019 / 00:53:12 UT	2458787 .53694	22:02:09	-09:34:13	1.260	0.486	46.874	1.092	16.71
2059 Baboquivari	15 November 2019 / 00:42:14 UT	2458802 .52933	22:49:46	-11:38:19	1.241	0.512	49.544	1.089	16.86
2059 Baboquivari	18 November 2019 / 00:39:39 UT	2458805 .52753	23:00:17	-11:48:09	1.241	0.519	49.811	1.090	16.90
2059 Baboquivari	21 November 2019 / 00:42:28 UT	2458808 .52949	23:11:01	-11:52:50	1.240	0.527	49.995	1.091	16.94
96744 (1999 OW3)	8 January 2020 / 4:00:56 UT	2458856 .66731	08:07:18	-62:55:21	1.274	0.744	50.326	1.246	16.45
96744 (1999 OW3)	10 January 2020 / 1:25:07 UT	2458858 .55911	08:03:50	-64:41:27	1.249	0.724	51.816	1.680	16.39
96744 (1999 OW3)	11 January 2020 / 1:07:46 UT	2458859 .54706	08:01:41	-65:39:17	1.236	0.713	52.652	1.660	16.36

Table 11: Observational data for 2059 Baboquivari and 96744 (1999 OW3).

Repeated observations were made in g, r, i, z, and C filters for both objects. Observations in the u filter were not obtained due to the high errors of u filter observations in the MOC4. In addition, observations of 2059 Baboquivari were obtained in B, V, R, and I. Observations were made in the following order: g, r, i, z, and C (then B, V, R, and I for 2059 Baboquivari only). Exposure times were 60 seconds for all filters except for z and B which both required 150 second exposure times with the goal of obtaining signal-to-noise ratio (SNR) of > 100 (~10,000 counts from the object).

The images were saved as Flexible Image Transport System (FITS) files. Biases, darks, and flat-field images were applied to the observational images for each night to create reduced images. Next, the instrumental magnitudes of each source were determined using Source Extractor (SExtractor). Instrumental magnitudes using the aperture photometry method and

using the Kron algorithm method were calculated. It was found that for aperture photometry, depending on the aperture size used, sources' instrumental magnitudes varied, so, a 2.5" aperture was decided on. Instrumental magnitudes using the Kron method were used to determine calibrated magnitudes.

2059 Baboquivari Analysis

Calibrated magnitudes for 2059 Baboquivari were determined using the following steps. First, only calibrated magnitudes for g, r, i, and z filters were calculated. 5 – 7 stars for each image were selected, each with SNR > 100 (~10,000 counts from the object), to use for calculating the NEA's calibrated magnitude. The same stars were used for each image in each filter for this process in order to reduce sources of error. This was possible because the background star field remained the same for the duration of the observation runs. PanSTARRS Kron magnitudes were queried for the calibration stars, and the following equation was used to calculate the zero point for each star and its associated error.

$$ZP = m_{catalog} - Im$$

$$\sigma_{ZP} = (m_{catalog}^2 + Im^2)^{1/2}$$

These zero points were averaged, then inspected to ensure they fell within 2 standard deviations of the average. If an outlier was determined, other calibration stars were selected. This process was repeated until all zero points fell within 2 standard deviations of the average zero point. The zero point values did change throughout the observation runs, but the associated errors were ~0.01 – 0.03 magnitudes. Some z filter images used fewer calibration stars than associated g, r, and i filter images due to the z filter's lower sensitivity. A trade-off needed to

occur, so stars with SNR less than 100 were not used in order to keep errors as low as possible for the z filter.

Next, the calibrated magnitude and associated error for 2059 Baboquivari was calculated using the following equation.

$$m_{calibrated} = Im + ZP$$

$$\sigma_{m\text{-}calibrated} = (Im^2 + ZP^2)^{1/2}$$

Thus, a calibrated magnitude for each observation of 2059 Baboquivari was calculated.

Next, calibrated magnitudes were converted into reflectances using the following equation from Alvarez-Candal (2013). For Solar colors, g – r = 0.40, r – r = 0, i – r = -0.11, and z – r = 0.128 (Sloan Digital Sky Survey, 2020).

$$F_j = 10^{-0.4[(mj - mr) - (mj' - mr')]}$$

$$\sigma_{Fj} = [\sigma_{mj}^2(F_j(\ln(10)(-0.4))^2 + \sigma_{mr}^2(F_j(\ln(10)(0.4))^2)]^{1/2}$$

Again, a reflectance value of each observation of 2059 Baboquivari was calculated. Reflectances were normalized to unity in the r filter.

Then, photometric spectra were created. Photometric spectra were created using each "series" of g, r, i, and z images. In addition, reflectances were averaged in each filter over the observation run. These graphs are shown below in Figures 34a – f. The photometric spectra obtained from SDSS observations is also shown, for comparison.

Figures 34a – f:

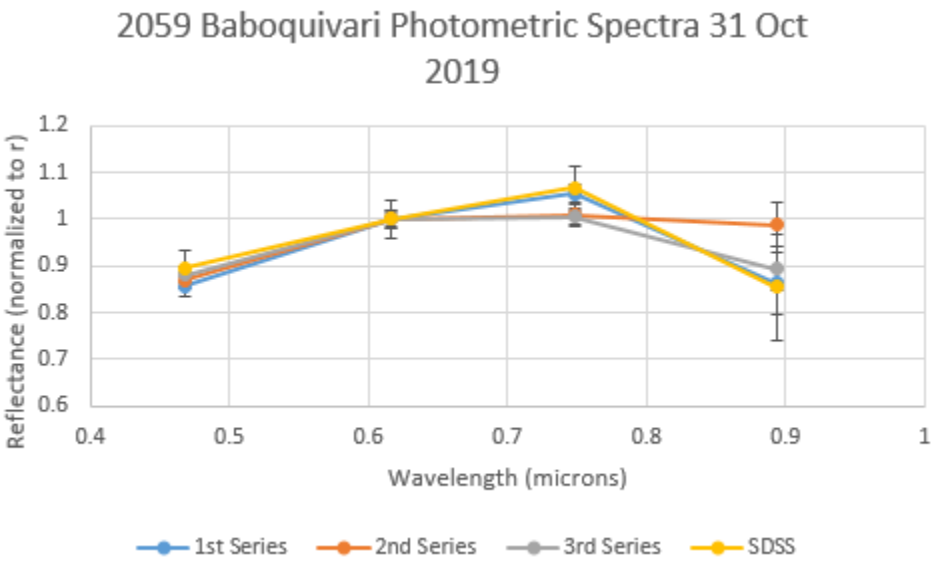

34a: 2059 Baboquivari photometric spectra 31 Oct 2019.

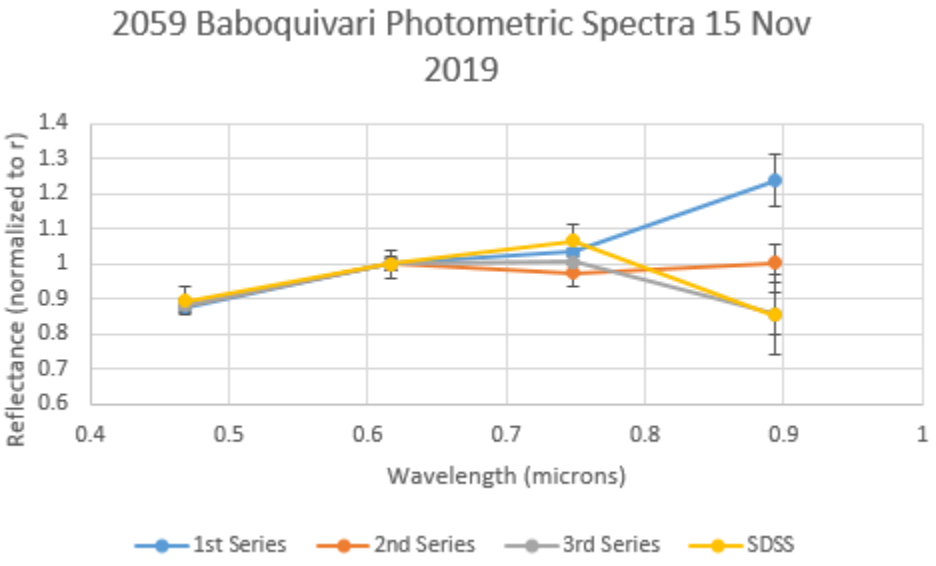

34b: 2059 Baboquivari photometric spectra 15 Nov 2019.

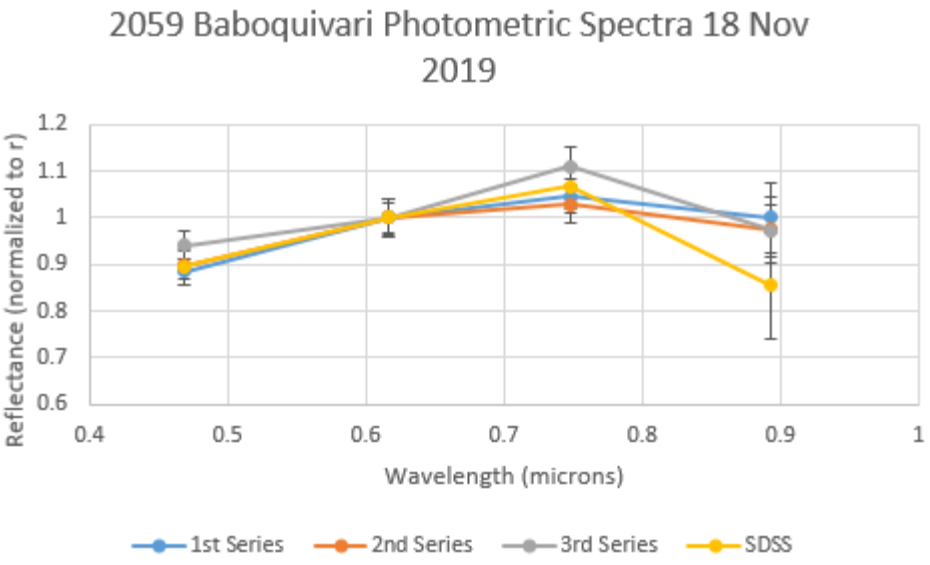

34c: 2059 Baboquivari photometric spectra 18 Nov 2019.

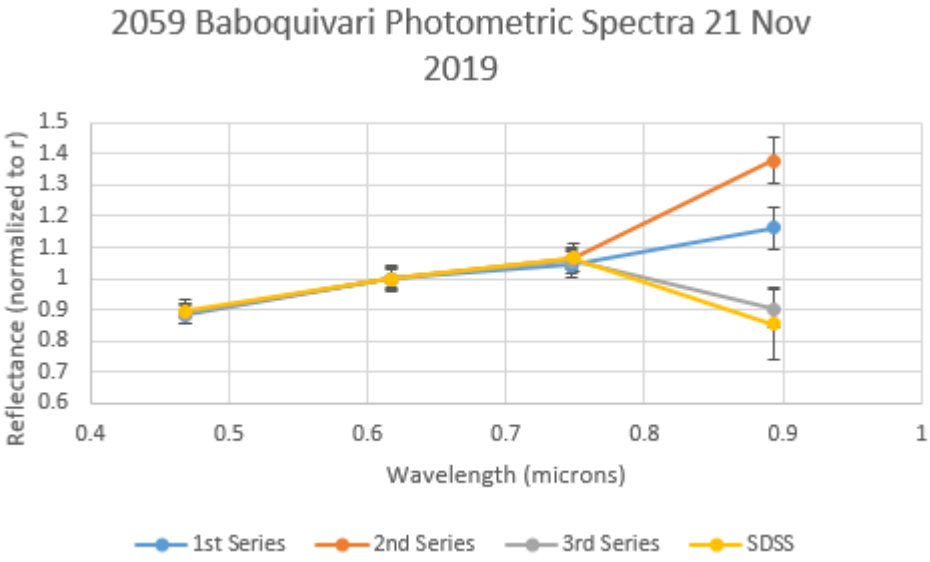

34d: 2059 Baboquivari photometric spectra 21 Nov 2019.

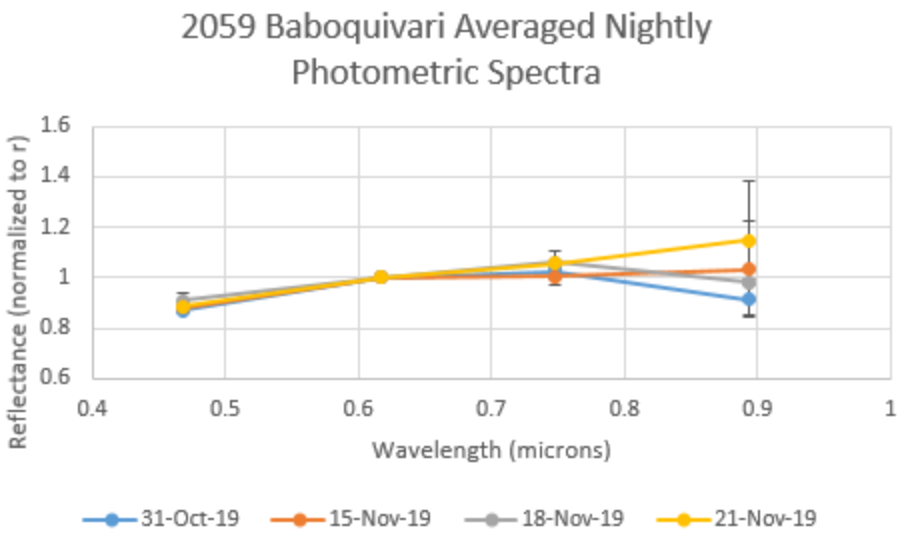

34e: 2059 Baboquivari averaged nightly photometric spectra.

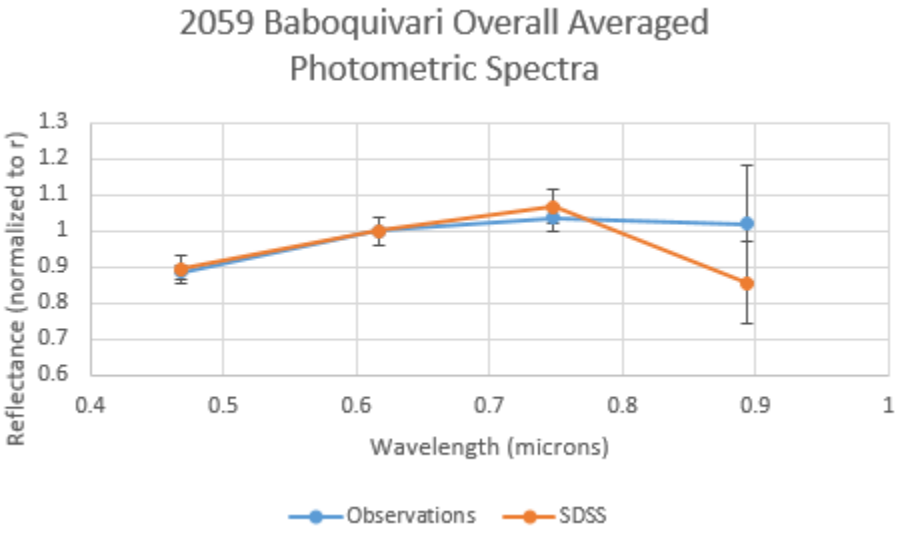

34f: 2059 Baboquivari overall averaged photometric spectra.

It is clear from these figures that 2059 Baboquivari exhibits a large variation in z filter reflectance and smaller variations in i filter reflectance. Comparing to the photometric spectrum from SDSS, 2059 Baboquivari's z filter reflectance is significantly higher – above 1.1 and one case at 1.37 – in 3 of 12 photometric spectra. Also, 3 of 12 i filter reflectances are somewhat

lower at ~1.0, while at the same time the z filter exhibits a slightly higher than average reflectance at ~1.0. Thus, from a majority (7 of 12) photometric spectra, 2059 Baboquivari's photometric spectrum qualitatively agrees with that from SDSS and appears to be a S-/Q-type asteroid, while for 3 of 12 it appears as more of a X-/P-/D-type asteroid, and in 2 of 12 it appears more similar to a C-complex asteroid. The determination of rough taxonomic assignment was done based on z – i and z filter reflectance primarily. If z – i was clearly negative, then that photometric spectrum was placed in the S-/Q-type category, and if z – i was near zero or positive the photometric spectrum was placed in either the C-complex or X-/P-/D-type categories. Then, if z filter reflectance was at or near unity, the photometric spectrum was placed in the C-complex category, but if higher than ~1.1 then the photometric spectrum was placed in the X-/P-/D-type category. These assignments are tabulated in Table 12. Keep in mind that these are rough taxonomic assignments, and must be taken with a hefty "grain of salt."

Date	Image Numbers (Series)	z – i Reflectance	z Reflectance	Taxonomic Assignment
31 Oct 2019	0-1-2-3 (1)	< 0	< 1	S/Q
31 Oct 2019	9-10-11-12 (2)	~ 0	~ 1	C
31 Oct 2019	18-19-20-21 (3)	< 0	< 1	S/Q
15 Nov 2019	0-1-2-3 (1)	> 0	> 1.1	X/P/D
15 Nov 2019	9-10-11-12 (2)	~ 0	~ 1	C
15 Nov 2019	18-19-20-21 (3)	< 0	< 1	S/Q
18 Nov 2019	0-1-2-3 (1)	< 0	~ 1	Weakly S/Q
18 Nov 2019	9-10-11-12 (2)	< 0	< 1	Weakly S/Q
18 Nov 2019	18-19-20-21 (3)	< 0	< 1	S/Q
21 Nov 2019	0-1-2-3 (1)	> 0	> 1.1	X/P/D
21 Nov 2019	9-10-11-12 (2)	> 0	> 1.1	X/P/D
21 Nov 2019	18-19-20-21 (3)	< 0	< 1	S/Q

Table 12: Rough taxonomic assignments for photometric spectra of 2059 Baboquivari.

Better fidelity in spectral assignment could not be achieved due to the resolution of these constructed photometric spectra. This variability diminishes as the reflectances are averaged over the entire night, and diminishes even further as the reflectances are averaged overall. Averaging over all observations, 2059 Baboquivari's photometric spectrum does not appear to match SDSS observations, and appears to have only a slight 1 μm absorption feature. It is clear that while for the majority of observations, 2059 Baboquivari's photometric spectra are similar to

the photometric spectrum from SDSS, there are striking variations. This will be explored further in the Discussion section.

In addition, C filter images were used to measure the total brightness change of 2059 Baboquivari through observing runs in order to create light curves. Since individual observation runs were only ~25 min, a rotation period could not be determined. However, significant total brightness changes can indicate rotation of 2059 Baboquivari. 5 – 10 calibration stars were used to calculate brightness changes due to changes in airmass or sky conditions, then 2059 Baboquivari's C filter instrumental magnitudes were subtracted from the average Δ(instrumental magnitude) of the calibration stars. This analysis is shown in Figures 35a – d.

Figures 35a – d:

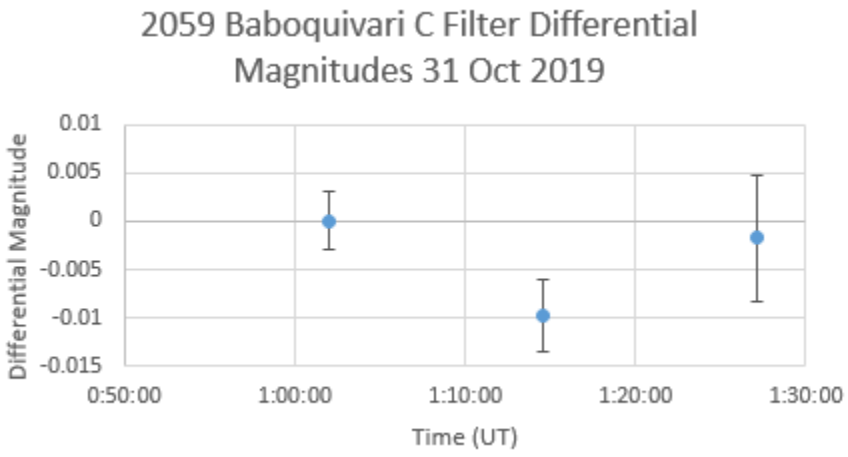

35a: 2059 Baboquivari C filter differential instrumental magnitudes from 31 Oct 2019.

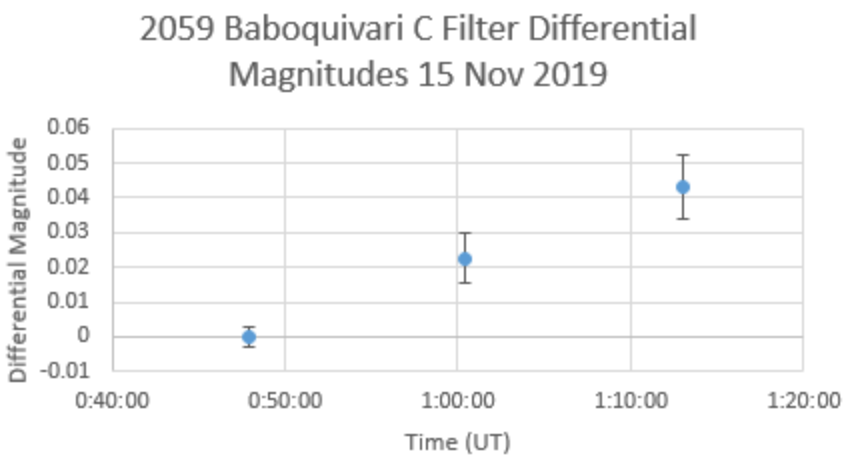

35b: 2059 Baboquivari C filter differential instrumental magnitudes from 15 Nov 2019.

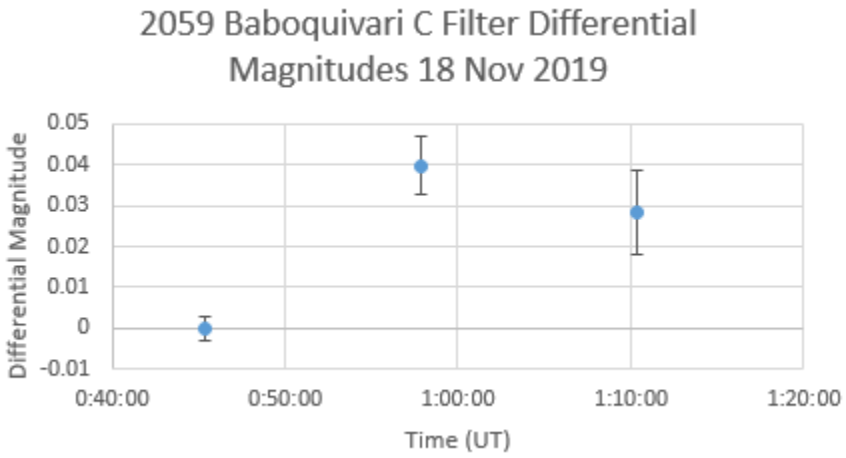

35c: 2059 Baboquivari C filter differential instrumental magnitudes from 18 Nov 2019.

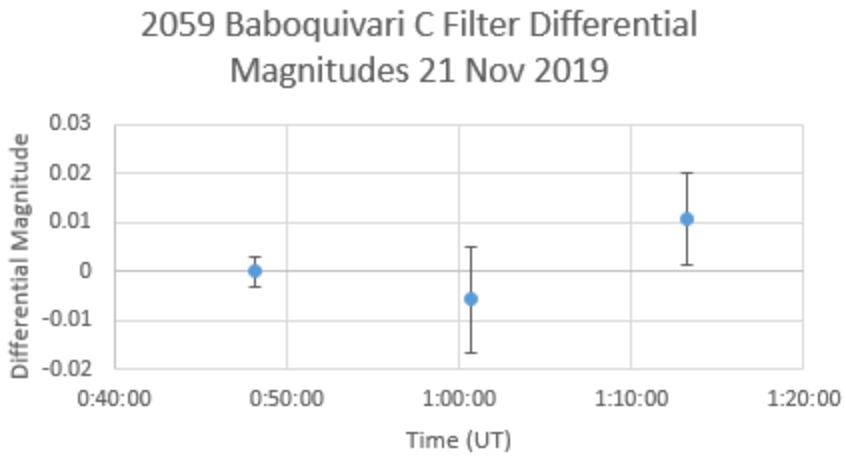

35d: 2059 Baboquivari C filter differential instrumental magnitudes from 21 Nov 2019.

As one can see, the light curves show only small variations (~0.05 mag max) through each ~25 min observing run. Thus, a rotation period cannot be reliably determined from these data, but 2059 Baboquivari's rotation period is likely much longer than each observation run. Since most H < 22 asteroid light curves vary between 0.5 – 1.0 magnitudes during a complete rotation (Pravec & Harris, 2000), 2059 Baboquivari probably did not exhibit significant rotation during each observation run.

Another observation worthy to note is that from 31 Oct through 18 Nov, 2059 Baboquivari's calibrated magnitudes generally increase (2059 Baboquivari gets dimmer in each filter) by ~0.5 magnitudes, then on 21 Nov calibrated magnitudes decrease by ~0.5 magnitudes (closer to ~0.7 magnitudes for the z filter). The reasons for this are not clear, but will be discussed.

The i – g slope and z – i band depth of 2059 Baboquivari's spectrum were also compared to its phase angle of observation (Carvano & Davalos, 2015). Since SDSS observed 2059 Baboquivari at a phase angle of 22.1 degrees and these observations were performed at phase

angles of ~45 – 50 degrees, any significant dependence of slope or band depth on phase angle should be observed. The graphs are shown in Figures 36a – b.

Figures 36 a – b:

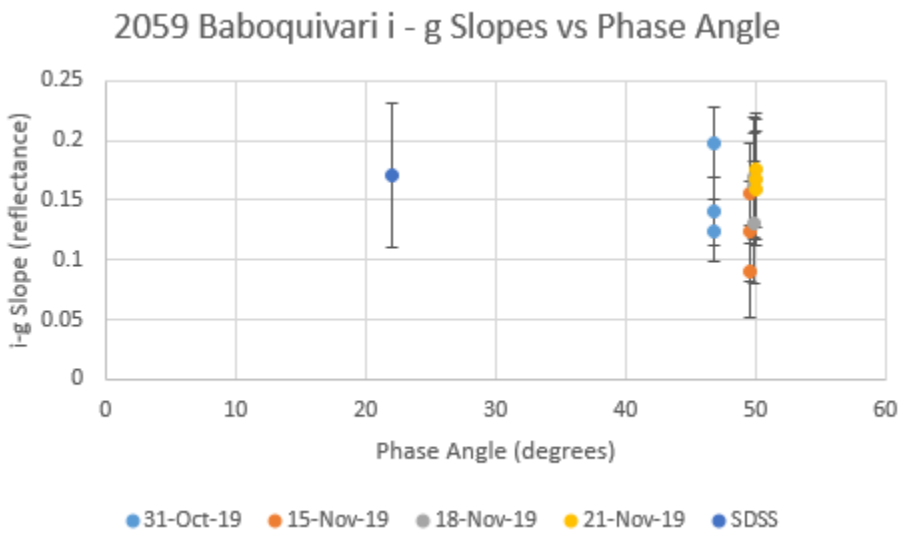

36a: 2059 Baboquivari i – g slope vs phase angle.

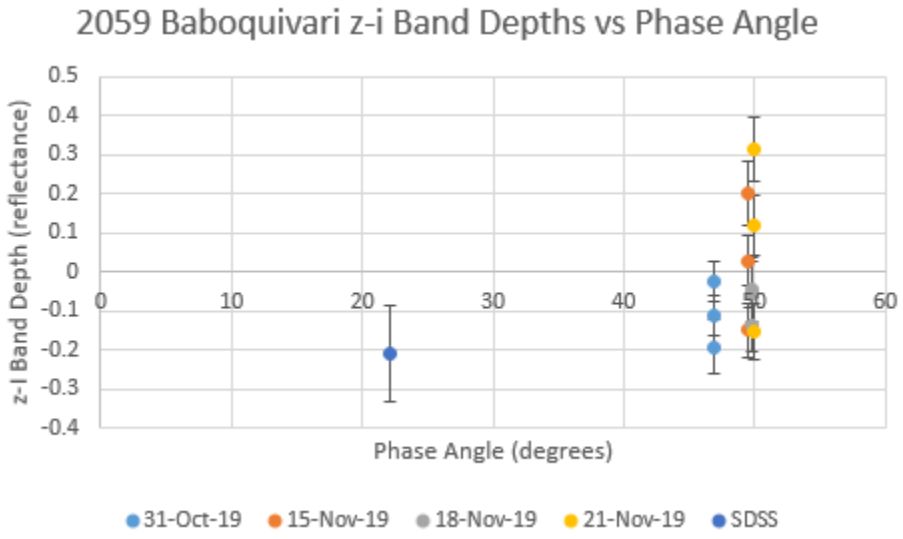

36b: 2059 Baboquivari z – i band depth vs phase angle.

Although the data are somewhat sparse, these figures show that there is no significant dependence of i – g slope on phase angle. In fact, i – g slope slightly anti-correlates with phase angle. In addition, z – i band depth vs phase angle shows a small anti-correlation; as phase angle increases, z – i band depth decreases slightly. This is an interesting result, as a minority of asteroids have neutral or negative relationships between visible spectral slope and phase angle (Carvano & Davalos, 2015). This will be discussed further in the Discussion section.

96744 (1999 OW3) Analysis

Moving on to 96744 (1999 OW3), the first item to note is that the analysis of observational data was done differently from 2059 Baboquivari. Since 96744 (1999 OW3) was observed at declinations of ~-65 degrees, and no photometric survey has reliably obtained magnitudes of stars that far south, only instrumental magnitudes could be used for the analysis. Thus, only differential photometry was performed. Differential photometry, however, can offer clues to 96744 (1999 OW3)'s properties.

The same biases, darks, and flats procedures were applied to raw images of 96744 (1999 OW3), with the image files in the FITS format. The same procedures in Source Extractor were also used for 96744 (1999 OW3). So, each image of 96744 (1999 OW3) resulted in a list of instrumental magnitudes for each source. C filter images were used to measure the total brightness change of 96744 (1999 OW3) through observing runs in order to create a light curve. 5 – 10 calibration stars were used to account for changes in airmass and sky conditions, then 96744 (1999 OW3)'s C filter instrumental magnitudes were subtracted from the average Δ(instrumental magnitude) of the calibration stars. Since observation runs for 96744 (1999 OW3) were much longer than those for 2059 Baboquivari, significant changes in brightness

should have been detected. This is indeed that case. Light curves for 96744 (1999 OW3) are shown in Figures 37a – c.

Figures 37a – c:

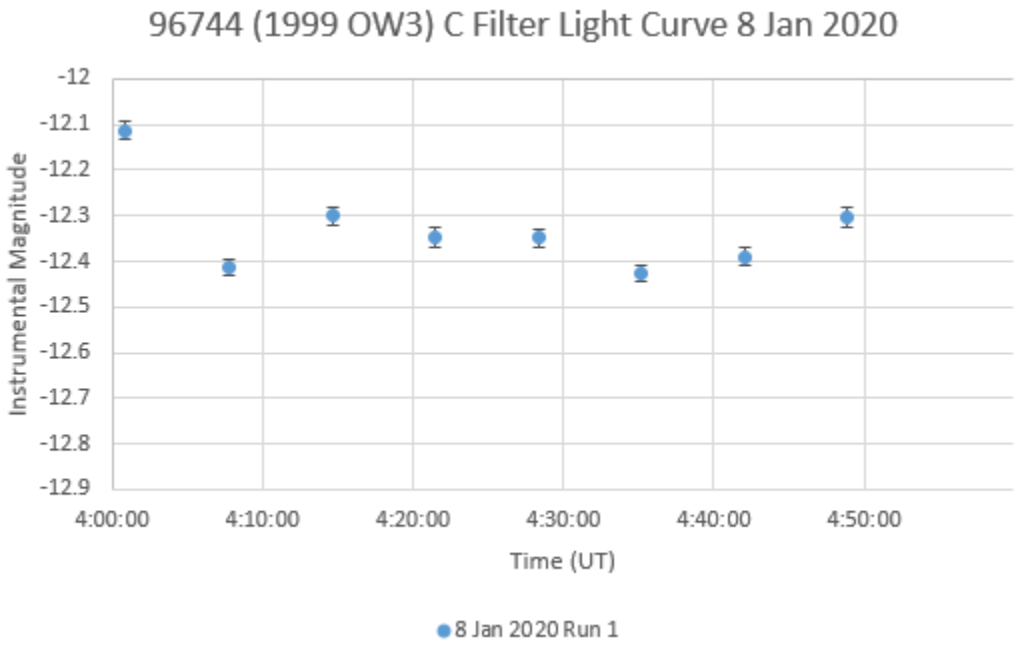

37a: 96744 (1999 OW3) C filter light curve from 8 Jan 2020. Observing run lasted for 00:54:49.

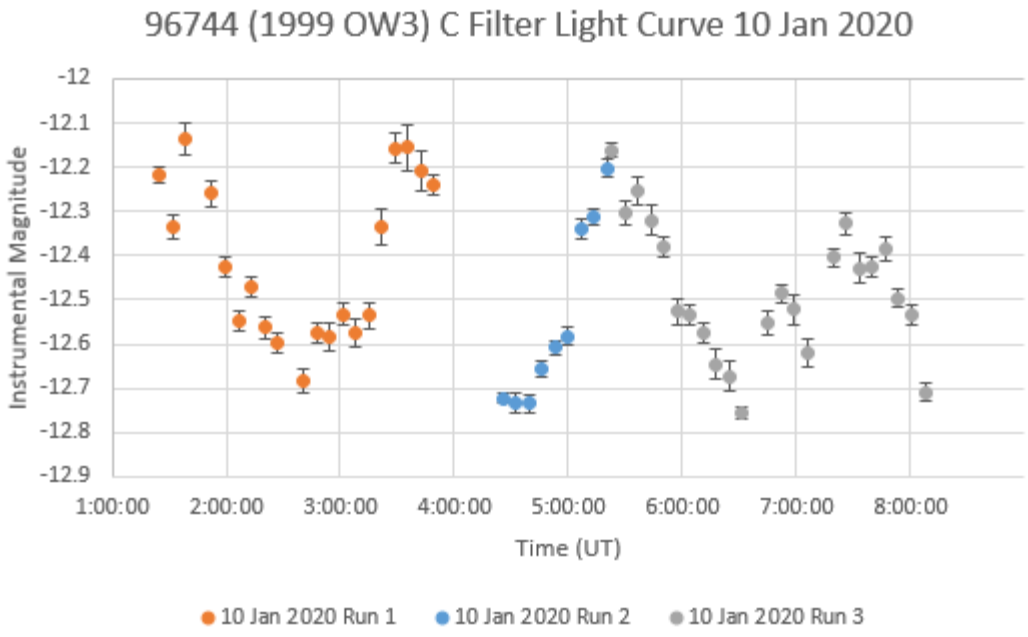

37b: 96744 (1999 OW3) C filter light curve, combined from 3 observing runs on 10 Jan 2020.

Observing runs lasted 2:24:08, 00:54:53, and 2:44:39, respectively.

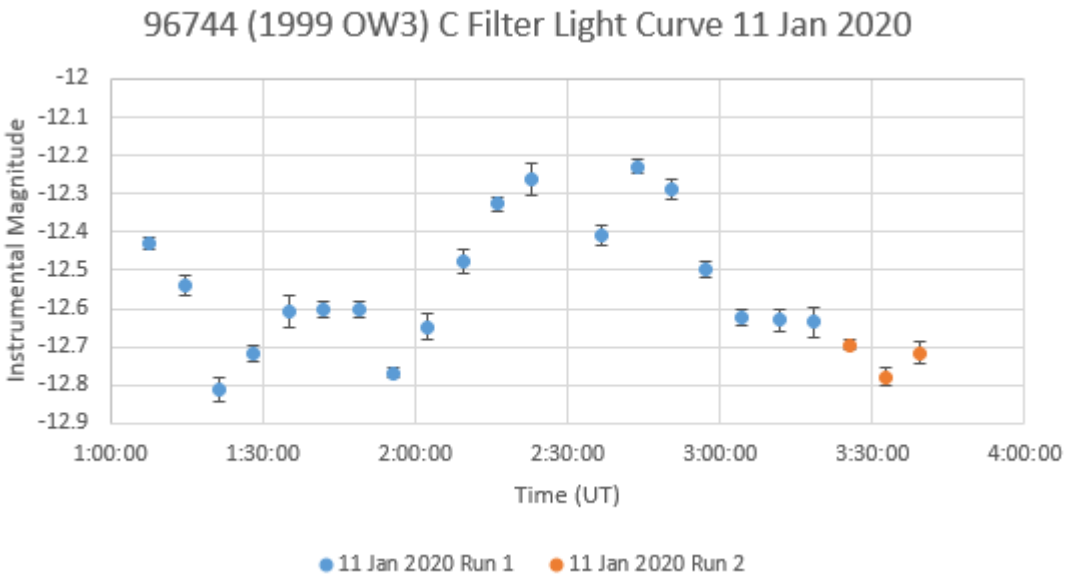

37c: 96744 (1999 OW3) C filter light curve, combined from 2 observing runs on 11 Jan 2020.

Observing runs lasted 2:10:42 and 00:13:42, respectively.

As can be seen, 96744 (1999 OW3) indeed shows a significant change in total brightness of ~0.5 – 0.6 magnitudes throughout the observation runs. By combining observation runs on 10 Jan, a ~0.65 – 0.70 magnitude variation is evident. A rotation period cannot be reliably determined at this point, but by visual inspection 96744 (1999 OW3) *possibly* has a rotation period of ~4 hours. This was determined by measuring the time between maxima and minima in 96744 (1999 OW3)'s light curve. The times between max-to-max and min-to-min in 96744 (1999 OW3)'s light curve are ~2 hours, so 96744 (1999 OW3) could have a rotation period of ~2 hours, but more likely has a rotation period of ~4 hours or another multiple of ~2 hours. 96744 (1999 OW3) *could* have a more complex shape, however, so this visual inspection is only preliminary.

Next, an analysis of 96744 (1999 OW3) was performed in g, r, i, and z filters. The same methods used in building C filter light curves were also used in building light curves in g, r, i, and z filters. The g, r, i, and z light curves are shown below in Figures 38a – c.

Figures 38a – c:

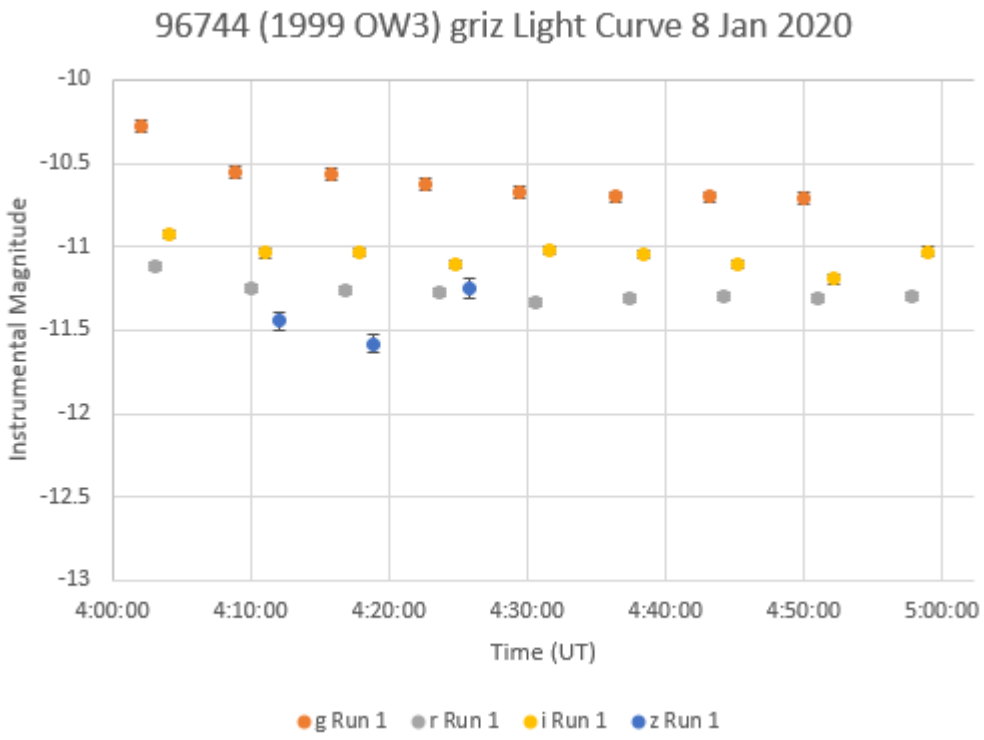

38a: Light curve of 96744 (1999 OW3) from 8 Jan 2020. Displayed in this figure are the g, r, i, and z filters. Only one observing run was taken this night.

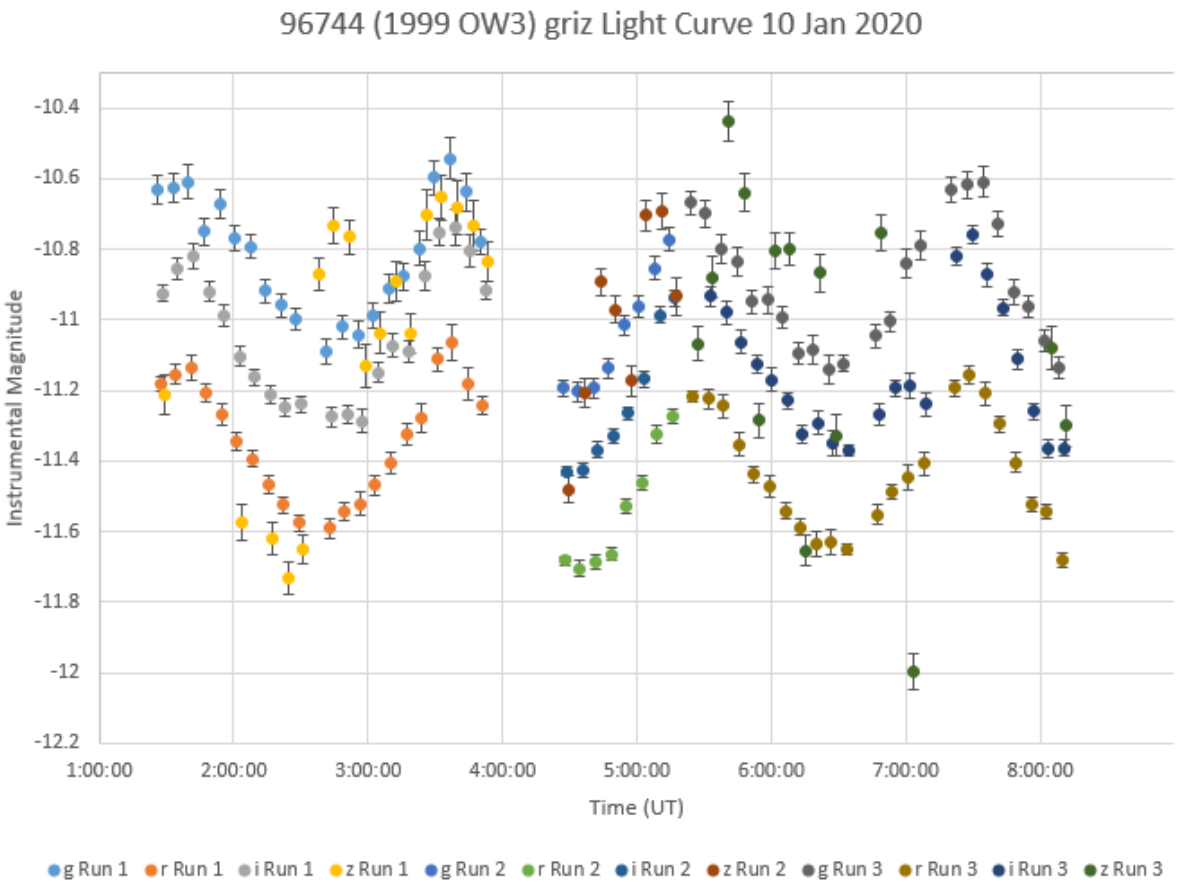

38b: g, r, i, and z light curves of 96744 (1999 OW3) from 10 Jan 2020. This graph was with data from 3 different observing runs.

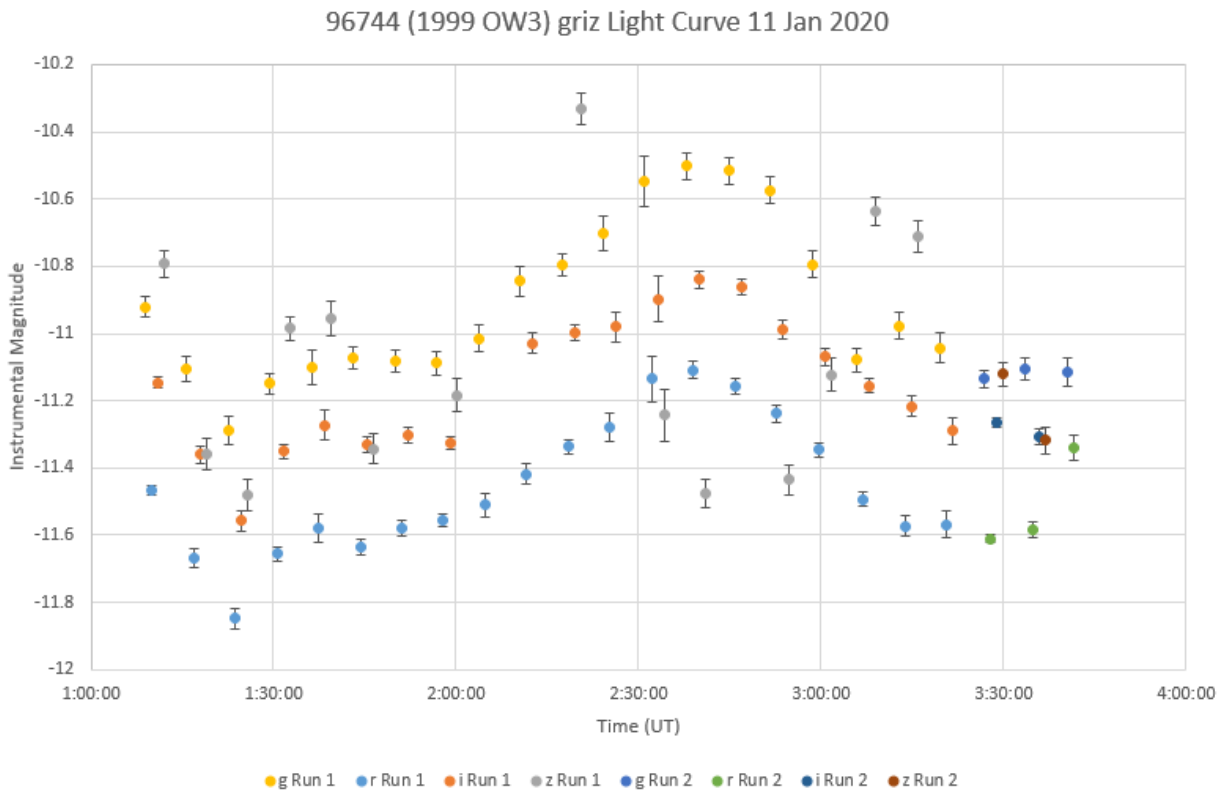

38c: g, r, i, and z light curve of 96744 (1999 OW3) from 11 Jan 2020. This graph was with data from 2 different observing runs.

It appears that for the majority of the time the z filter instrumental magnitudes are less negative than the i filter instrumental magnitudes. In addition, it appears that i filter instrumental magnitudes are generally more negative than g filter instrumental magnitudes. This gives support for these observations being similar to observations by SDSS. However, the magnitudes in question are instrumental magnitudes and are not calibrated, so caution must be used in extracting any information from these. These light curves will be analyzed further in the Discussion section in an attempt to determine more properties of 96744 (1999 OW3). An analysis of i – g and z – i colors with respect to time and its light curve will be performed.

Discussion

Going back to the original thesis question, did these observations of 2059 Baboquivari and 96744 (1999 OW3) consistently replicate the observations done by the Sloan Digital Sky Survey? The answer to this question for 2059 Baboquivari appears to be no. For 96744 (1999 OW3), given the analyses that could be performed, the answer is not clear. Because 96744 (1999 OW3) was observed at ~-65 degrees declination, calibrated magnitudes in g, r, i, and z filters could not be determined. However, a further analysis of 96744 (1999 OW3) will shed more light and will hopefully enable at least a partial answer to the question.

2059 Baboquivari Discussion

First, 2059 Baboquivari will be discussed. Recall, all analyses must point to the Statement of the Problem:

- Is the photometry found in the SDSS MOC4 database for 2059 Baboquivari and 96744 (1999 OW3) consistently repeatable?
- If not consistently repeatable, what are the reason(s) for their photometric variability?

In order to explore photometric variability more, Figures 39a – l are displayed to show how 2059 Baboquivari's z filter brightness varies. They show 2059 Baboquivari's time-resolved instrumental magnitude, calibrated magnitude, and reflectances.

Figures 39a – l:

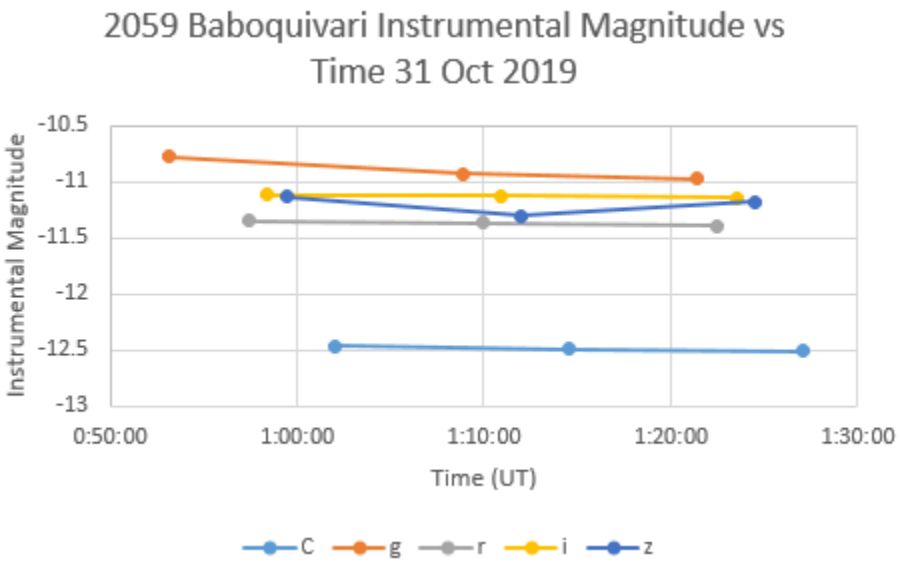

39a: 2059 Baboquivari instrumental magnitude vs time graph for 31 Oct 2019. Instrumental magnitudes were calculated using Kron photometry.

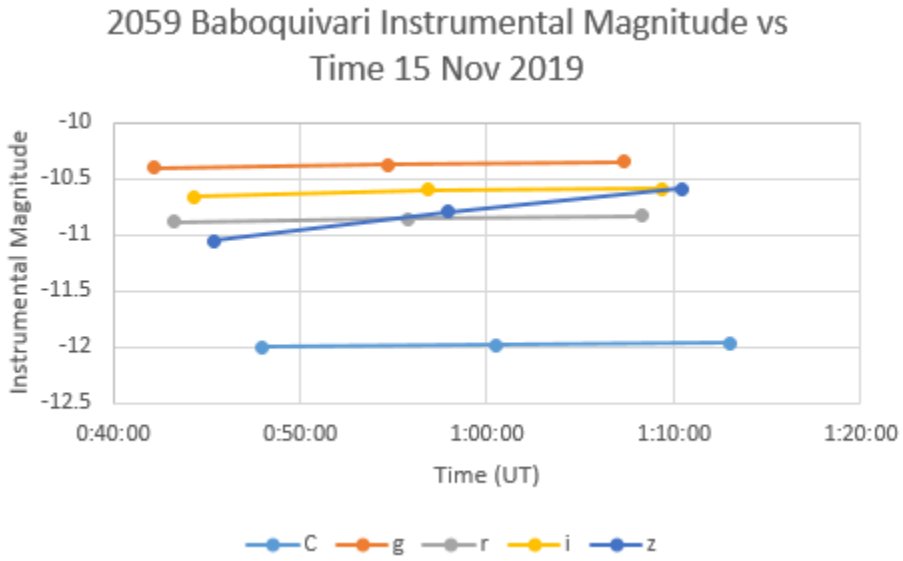

39b: 2059 Baboquivari instrumental magnitude vs time graph for 15 Nov 2019. Instrumental magnitudes were calculated using Kron photometry.

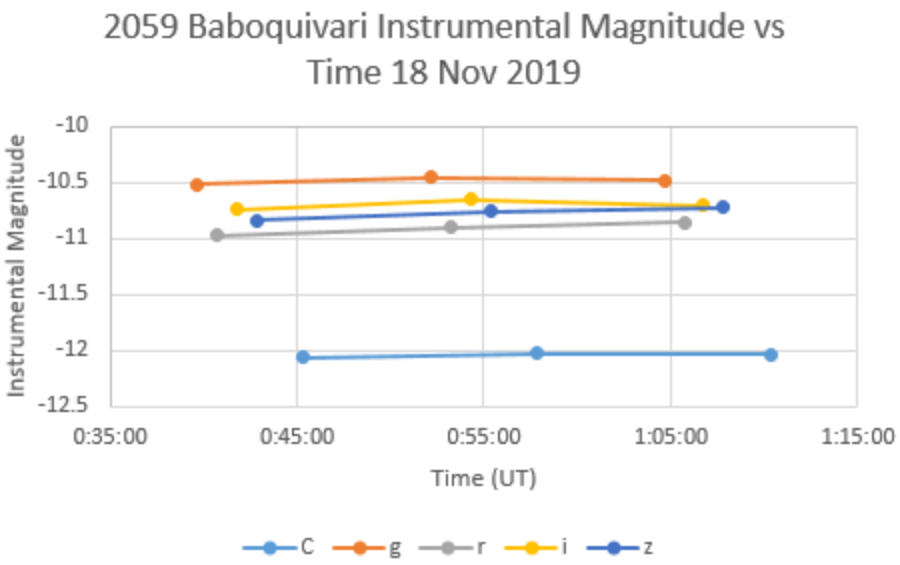

39c: 2059 Baboquivari instrumental magnitude vs time graph for 18 Nov 2019. Instrumental magnitudes were calculated using Kron photometry.

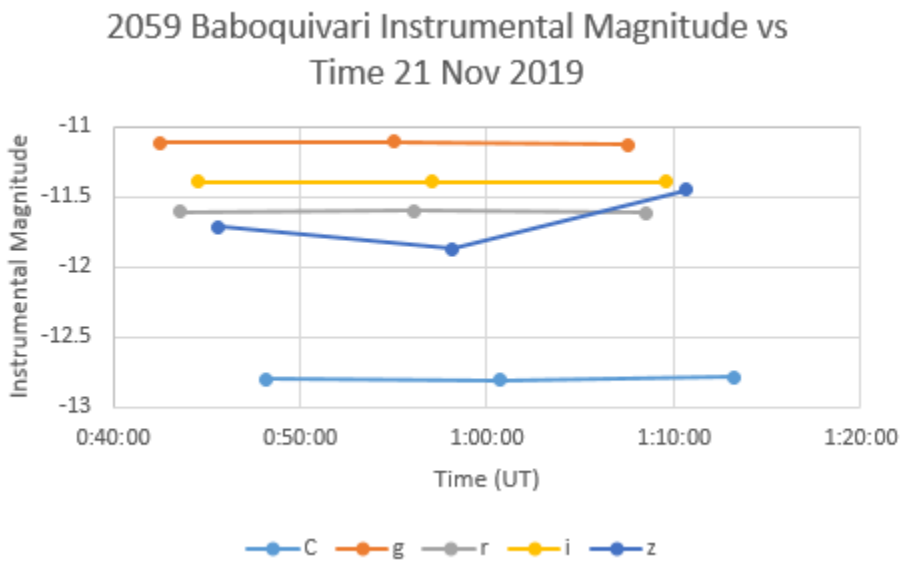

39d: 2059 Baboquivari instrumental magnitude vs time graph for 21 Nov 2019. Instrumental magnitudes were calculated using Kron photometry.

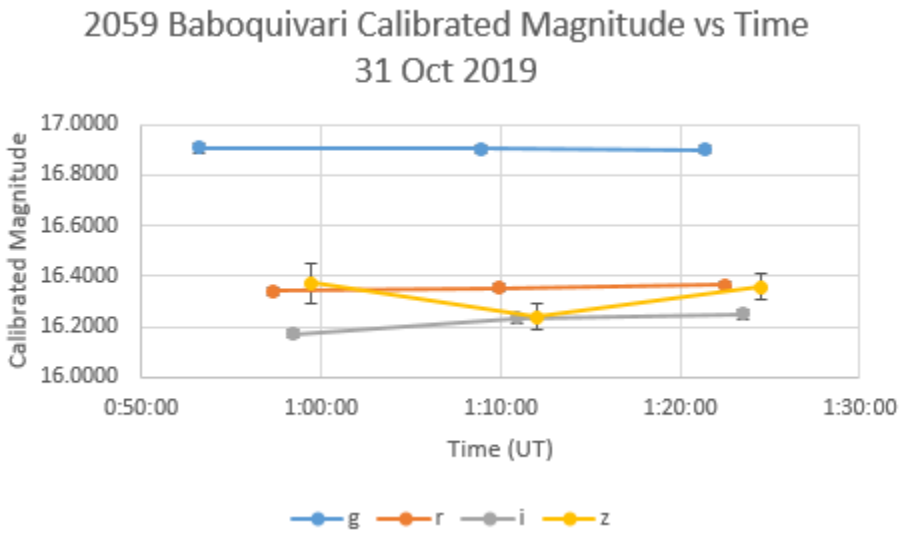

39e: 2059 Baboquivari calibrated magnitude vs time graph for 31 Oct 2019.

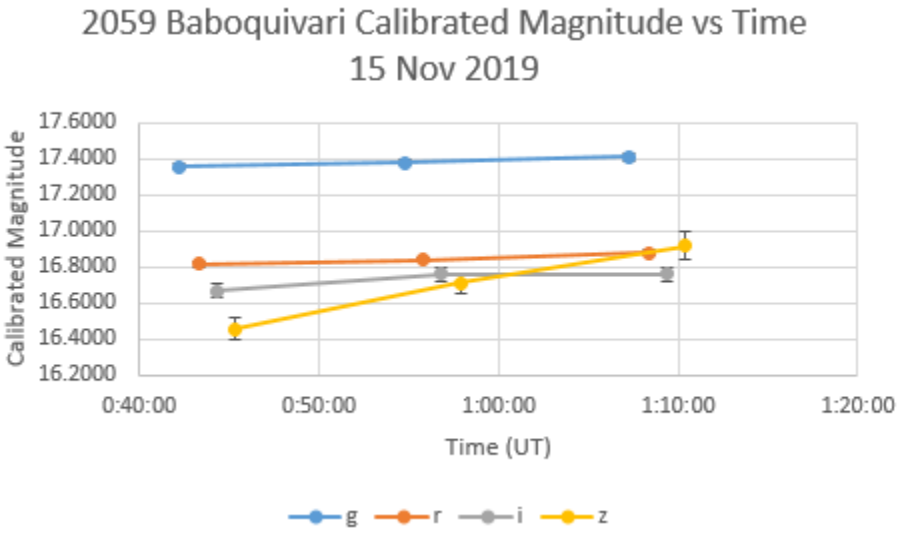

39f: 2059 Baboquivari calibrated magnitude vs time graph for 15 Nov 2019.

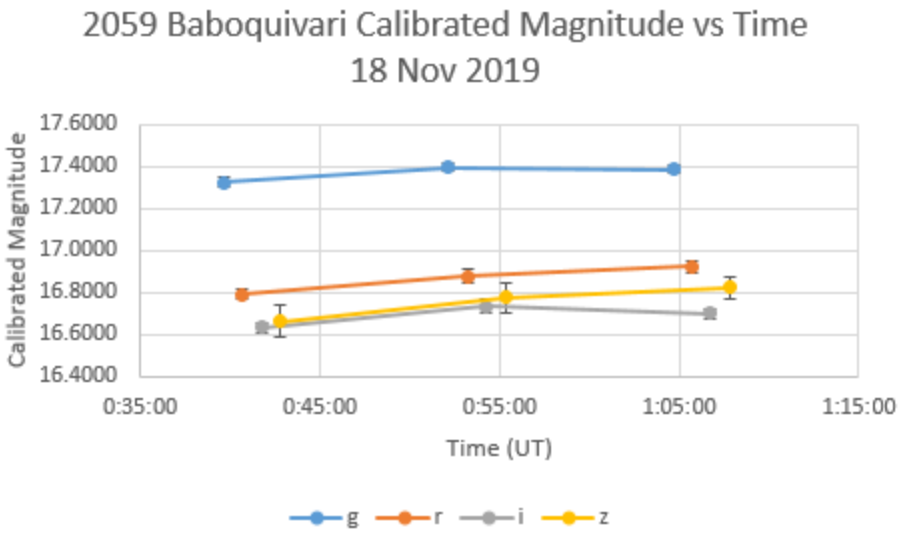

39g: 2059 Baboquivari calibrated magnitude vs time graph for 18 Nov 2019.

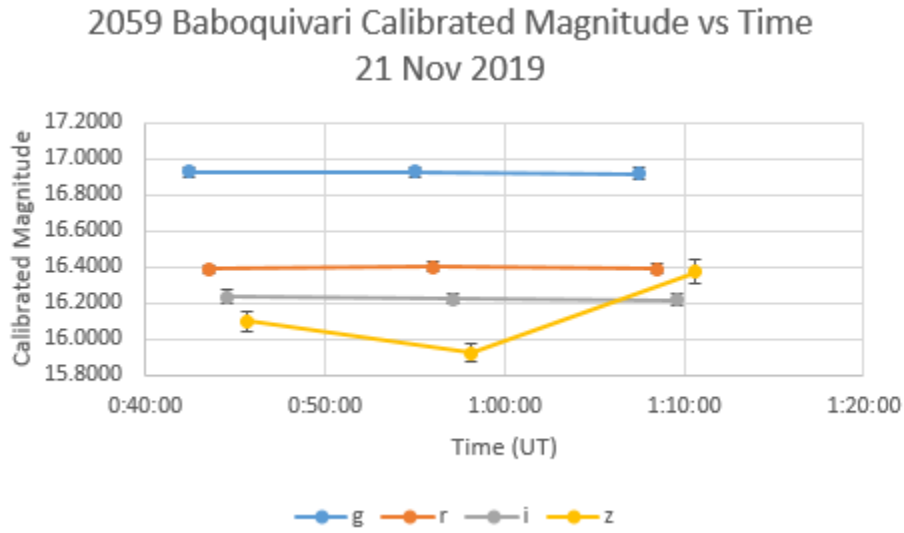

39h: 2059 Baboquivari calibrated magnitude vs time graph for 21 Nov 2019.

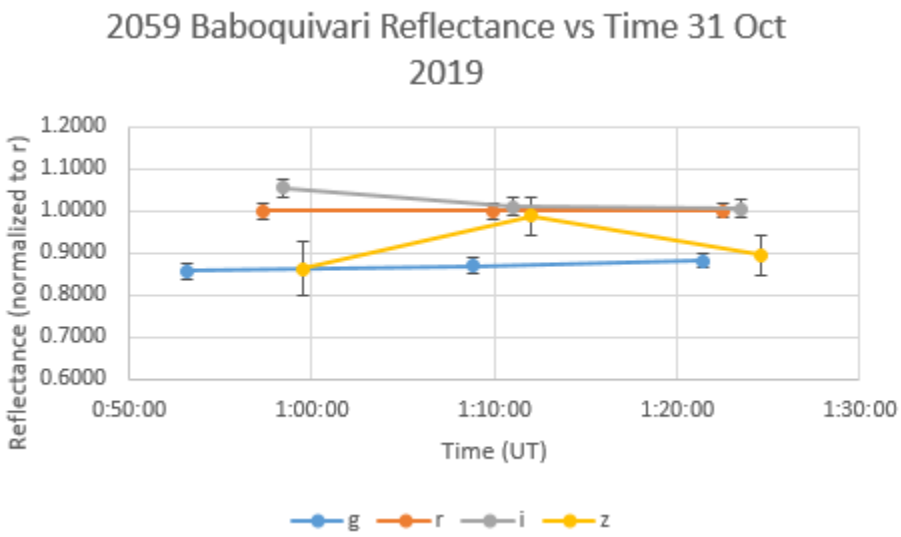

39i: 2059 Baboquivari reflectances vs time graph for 31 Oct 2019. Notice that this graph shows a time-resolved photometric spectrum.

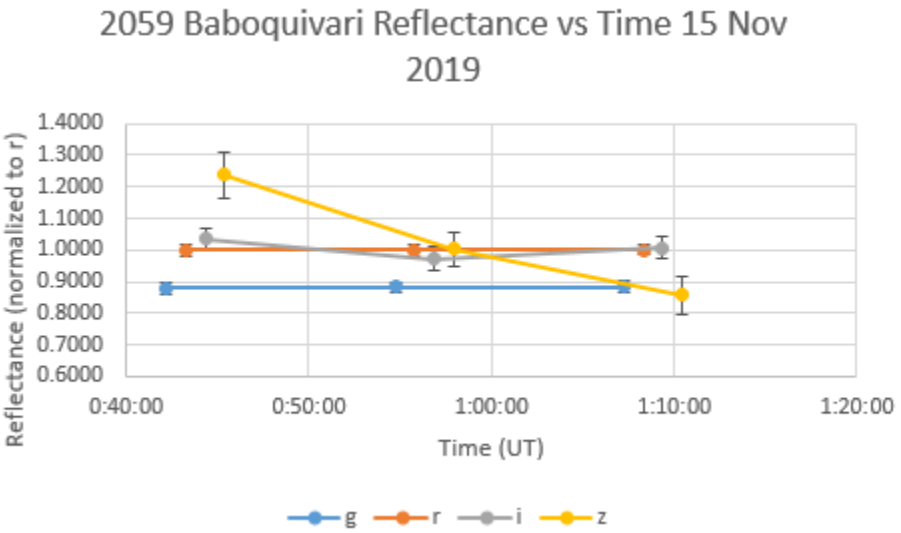

39j: 2059 Baboquivari reflectances vs time graph for 15 Nov 2019. Notice that this graph shows a time-resolved photometric spectrum.

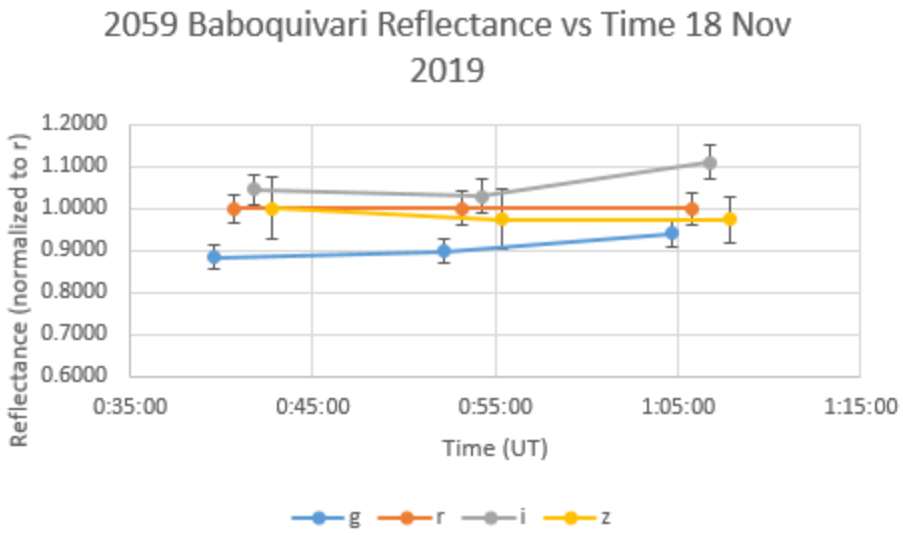

39k: 2059 Baboquivari reflectances vs time graph for 18 Nov 2019. Notice that this graph shows a time-resolved photometric spectrum.

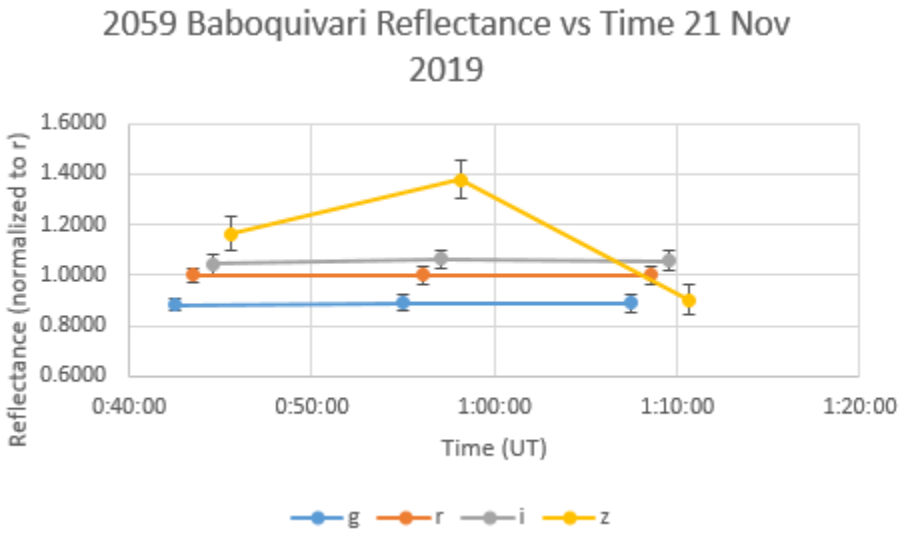

39l: 2059 Baboquivari reflectances vs time graph for 21 Nov 2019. Notice that this graph shows a time-resolved photometric spectrum.

2059 Baboquivari exhibits significant variability in the z filter and with only small variability in the g, r, and i filters. The causes for this variability are not known, but some

reasons can be considered and others can be ruled out. In addition, as mentioned in the Analysis section, 2059 Baboquivari's g, r, and i calibrated magnitudes generally increase (get dimmer) by ~0.5 magnitudes from 31 Oct to 18 Nov. Then on 21 Nov, the g, r, and i calibrated magnitudes decrease (get brighter) by ~0.5 magnitudes. The z filter calibrated magnitudes exhibit generally the same behavior, except on 21 Nov they decrease by ~0.7 – 0.8 magnitudes. This can be seen above in Figure 38.

What is the statistical significance regarding 2059 Baboquivari's z filter variability? In order to examine this, 2059 Baboquivari's z filter reflectance from these observations will be compared to its z filter reflectance from SDSS observations. In order to reduce the bias in the analysis, the corrected sample standard deviation will be used, which is defined as

$$s = \sqrt{\frac{1}{N-1}\sum_{i-1}^{N}(x_i - \bar{x})^2}.$$

The following test will be performed, in which $\sigma_{difference}$ is the number of σ the two values – observations vs. the SDSS observation – differ from each other.

$$\sigma_{difference} = [(z_{RMS} - z_{SDSS})^2/(s^2 + \sigma_{SDSS}^2)]^{1/2}$$

In this equation, z_{RMS} is the z filter reflectance root mean square (RMS) value of the observations, z_{SDSS} is the z filter reflectance value in the SDSS observation, s is the corrected sample standard deviation of observations, and σ_{SDSS} is the z filter reflectance uncertainty in the SDSS observation.

This equation can also be used for comparing individual z filter reflectance values and their uncertainties with 2059 Baboquivari's z filter reflectance value and uncertainty from SDSS.

$$\sigma_{difference} = [(z_{observation} - z_{SDSS})^2/(s^2 + \sigma_{SDSS}^2)]^{1/2}$$

The $\sigma_{Difference}$ values are shown below in Tables 13 and 14.

z_{RMS}	s	z_{SDSS}	σ_{SDSS}	$\sigma_{difference}$
1.031	0.160	0.855	0.114	0.895

Table 13: Results of statistical test with 2059 Baboquivari z filter reflectance RMS value from observations and from SDSS.

Date	Series	z Reflectance	$\sigma_{difference}$
31 Oct 2019	1	0.863	0.057
31 Oct 2019	2	0.988	1.080
31 Oct 2019	3	0.895	0.321
15 Nov 2019	1	1.237	2.801
15 Nov 2019	2	1.002	1.169
15 Nov 2019	3	0.857	0.018
18 Nov 2019	1	1.001	1.066
18 Nov 2019	2	0.975	0.895
18 Nov 2019	3	0.974	0.936
21 Nov 2019	1	1.163	2.328
21 Nov 2019	2	1.379	3.829
21 Nov 2019	3	0.903	0.375

Table 14: Results of statistical test with 2059 Baboquivari z filter reflectances from observations and from SDSS.

As can be seen, 2059 Baboquivari's observed RMS z filter reflectances vary from its SDSS z filter reflectance at the 0.895σ level, and individual z filter reflectance measurements vary from its SDSS z filter reflectance up to the 3.8σ level. A 3σ level is considered statistically significant. Thus, 2059 Baboquivari's observed RMS z filter reflectances actually do not vary at a statistically significant level from 2059 Baboquivari's z filter reflectance from SDSS, but individual measurements may. This can be at least partly attributed to 2059 Baboquivari's relatively high z filter uncertainty in SDSS (0.11).

This same test was performed for 2059 Baboquivari's z – i reflectance values, and are tabulated below in Tables 15 and 16.

$z - i_{RMS}$	s	$z - i_{SDSS}$	σ_{SDSS}	$\sigma_{difference}$
0.151	0.157	-0.212	0.123	1.819

Table 15: Results of statistical test with 2059 Baboquivari z – i filter reflectance RMS value from observations and from SDSS.

Date	Series	z – i Reflectance	$\sigma_{difference}$
31 Oct 2019	1	-0.192	0.138
31 Oct 2019	2	-0.022	1.418
31 Oct 2019	3	-0.111	0.756
15 Nov 2019	1	0.203	2.787
15 Nov 2019	2	0.029	1.738
15 Nov 2019	3	-0.149	0.439
18 Nov 2019	1	-0.045	1.120
18 Nov 2019	2	-0.055	1.062
18 Nov 2019	3	-0.137	0.530
21 Nov 2019	1	0.120	2.270
21 Nov 2019	2	0.315	3.540
21 Nov 2019	3	-0.153	0.412

Table 16: Results of corrected sample standard deviation statistical test with 2059 Baboquivari z filter reflectances.

Similarly to the previous test, 2059 Baboquivari's observed RMS z – i filter reflectances vary from its SDSS z – i filter reflectance at the 1.8σ level, and individual z filter reflectance measurements vary from its SDSS z filter reflectance up to the 3.5σ level. Thus, 2059 Baboquivari's observed RMS z – i values actually do not vary at a statistically significant level from 2059 Baboquivari's z – i value from SDSS, but individual measurements may. Again, this

can be at least partly attributed to 2059 Baboquivari's relatively high z filter uncertainty in SDSS (0.11) and z – i uncertainty (0.12).

What are the reasons for 2059 Baboquivari's variability? There could be any number of reasons, but the most likely are (not necessarily in any order):

1. Sky Conditions
2. Rotational Heterogeneities
3. Dust Cloud
4. Moon or Moonlet
5. Kron Photometry Issues
6. Filter Wheel Error

These reasons are discussed below.

1. Sky Conditions

First, a check of the sky conditions during observation runs is necessary, especially concerning z filter observations. This is because 1) the z filter displays the greatest photometric variability, and 2) the z filter lies on the boundary between optical and infrared wavelengths. Patchy, light cirrus clouds can cause changes in sky conditions over short time intervals. The following figures show the instrumental magnitudes of several bright stars as a function of image number (corresponding to time).

Figures 40a – d:

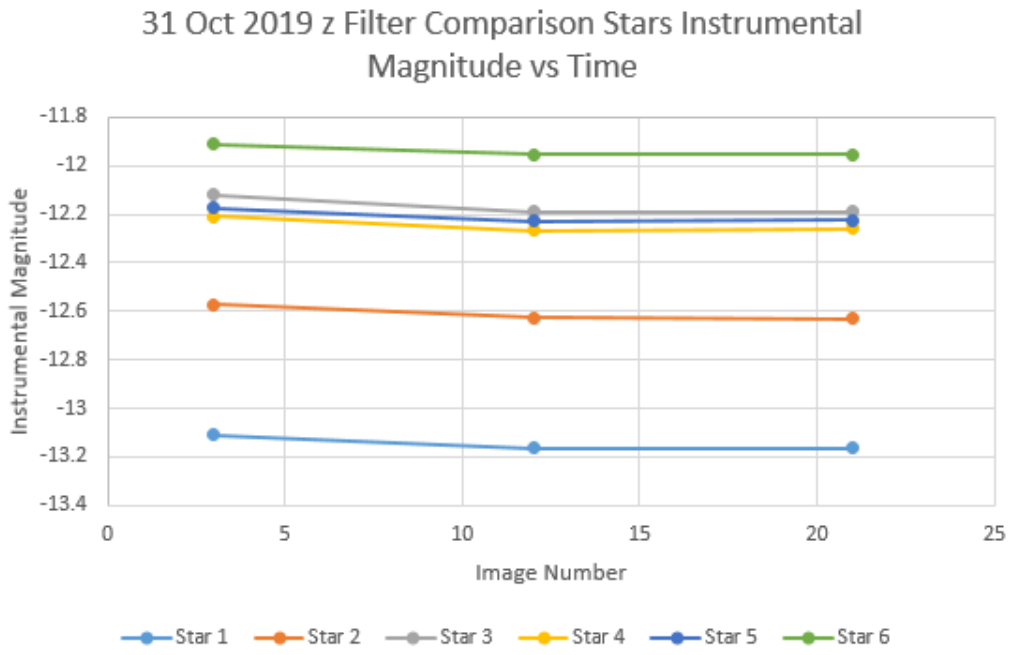

40a: 31 Oct 2019 z filter comparison stars instrumental magnitude vs. time.

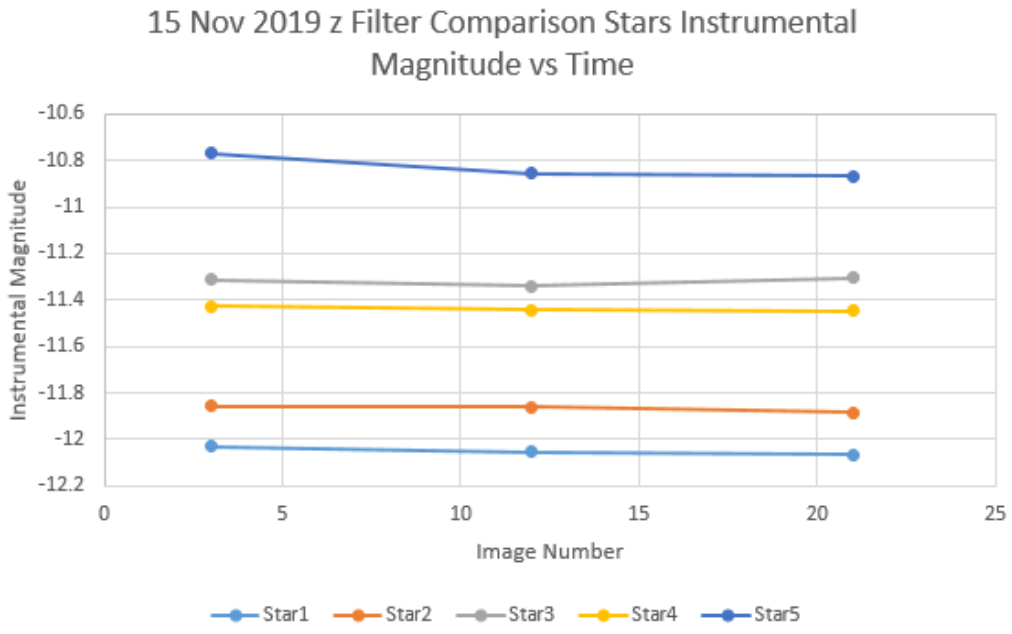

40b: 15 Nov 2019 z filter comparison stars instrumental magnitude vs. time.

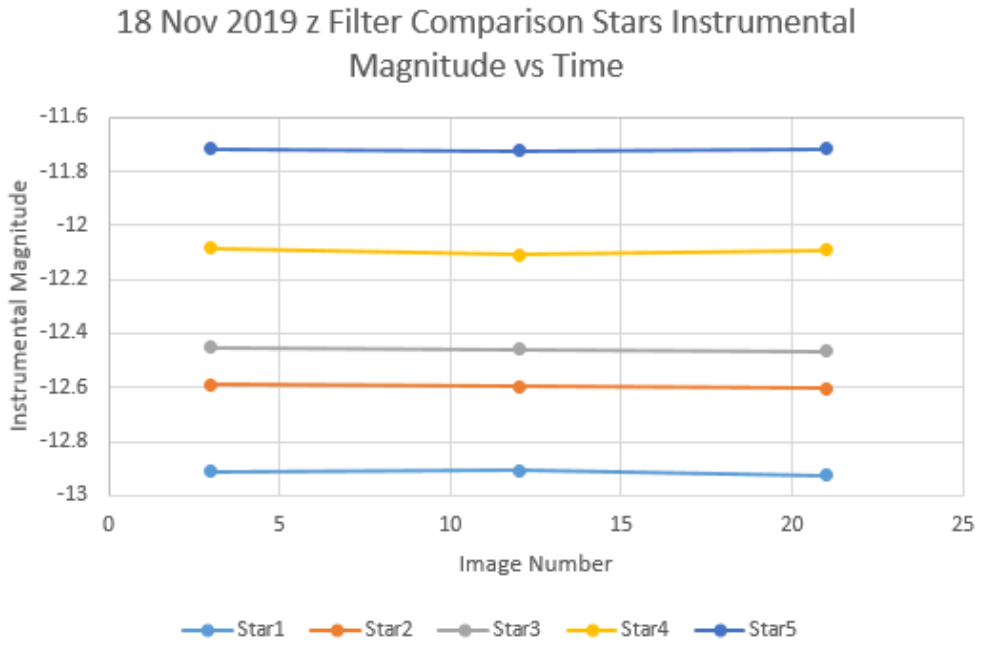

40c: 18 Nov 2019 z filter comparison stars instrumental magnitude vs. time.

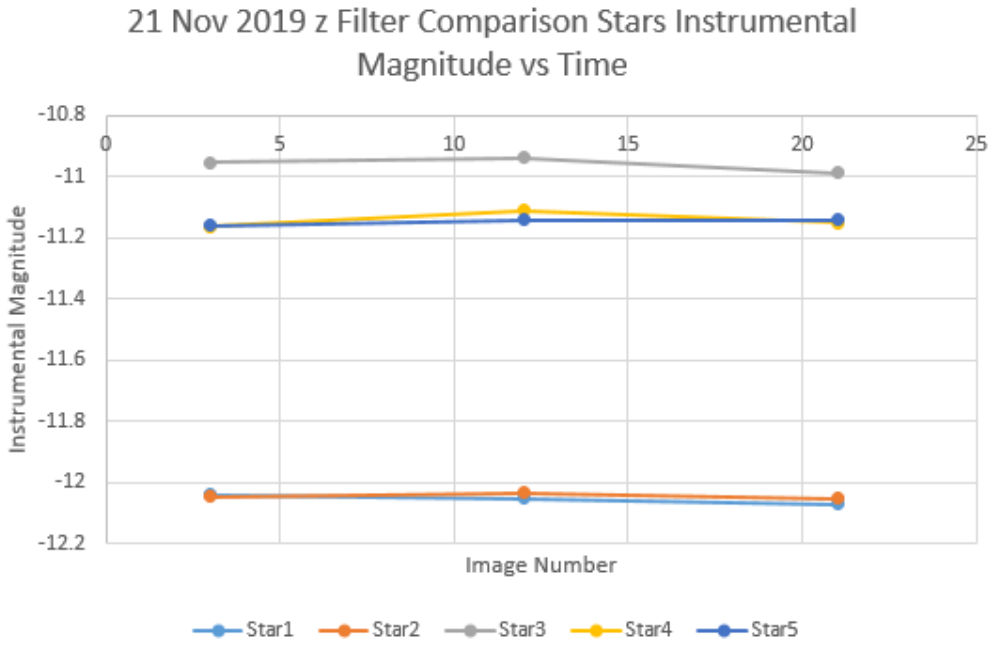

40d: 21 Nov 2019 z filter comparison stars instrumental magnitude vs. time.

As can be observed from these figures, there are minor changes in instrumental magnitude of these bright stars as a function of time. However, the instrumental magnitude changes are small (~0.05 magnitudes) and generally trend in the same direction. Thus, changes in sky conditions can be ruled out as a source of 2059 Baboquivari's z filter variability.

2. Rotational Heterogeneities

Another reason for 2059 Baboquivari's photometric variability to consider is variability due to its rotation. Since observation runs of 2059 Baboquivari lasted only ~25 minutes, only a fraction of its rotational period could be observed through the course of each run. C filter light curves of 2059 Baboquivari showed only small changes of ~0.05 magnitudes through each ~25 minute observation run. From these data, a rotational period could not be determined, but it could be concluded that 2059 Baboquivari likely has a rotational period much greater than the lengths of observation runs. This can be reasoned by two pieces of knowledge: 1) most H < 22 asteroids' light curves vary between 0.5 – 1.0 magnitudes and 2) for an asteroid of absolute magnitude similar to 2059 Baboquivari's (16.0) it would be unlikely for its rotation period to be less than ~2 hours (Pravec & Harris, 2000). If 2059 Baboquivari's rotation period were near 2 hours, then one would expect to see its light curve change at least ~0.2 – 0.3 magnitudes through the ~25 min observing run, and this is clearly not observed. Due to these reasons, photometric variability due to rotation is not likely for 2059 Baboquivari.

Another factor to consider, however, is that in theory higher phase angles of observation could exaggerate rotational heterogeneities. An increase in phase angle would decrease the fraction of the asteroid that is *both illuminated by the Sun and visible from Earth*. This is the

same effect that one observes as the Moon changes its phases. Any rotation therefore would lead to a higher *percent change of surface that is illuminated by the Sun and visible from Earth*, and a non-spherical surface would exaggerate this effect due to cratering and shadowing. For example, if an asteroid has a 3 hour rotation period, a 30 minute observation run covers 1/6 of a rotation period. The asteroid would rotate 60 degrees during the observing run. If the asteroid is observed at a phase angle of 45 degrees, the illuminated and visible fraction of the asteroid is 135 degrees (this is assuming the asteroid is spherical). Thus, through the observing run, 44% of the asteroid's *illuminated and visible surface* would change (60 degrees rotation/135 degrees surface illuminated and visible = 0.44). If a crater or other feature with different composition exists on the asteroid's surface, then that feature's spectral properties will be exaggerated, and thus the spectrum of the asteroid would exhibit variability.

However, this is probably not the case for 2059 Baboquivari. Although 2059 Baboquivari was observed at phase angles of ~45 – 50 degrees, C filter light curves show only a ~0.05 magnitude change in total brightness over ~25 min observing runs, much less than average $H < 22$ asteroid brightness change of ~0.5 – 1.0 magnitudes through a light curve. Therefore, 2059 Baboquivari's surface area was probably not highly sampled through each observation run. Since 2059 Baboquivari is probably ~2 km in diameter, its rotation period is likely longer than ~2 hours, giving more evidence that its surface area was not highly-sampled. In conclusion, z filter variability on ~12 minute timescales is probably not caused by 2059 Baboquivari's rotation. Rotational heterogeneities are thus ruled out for 2059 Baboquivari, at least from these observations.

3. Dust Cloud

Another reason for 2059 Baboquivari's photometric variability is that it may have a dust/debris cloud/ring (hereafter referred to as a dust cloud) surrounding it. From SDSS observations and from the majority of this study's observations, the surface of 2059 Baboquivari appears to be most likely olivine-/pyroxene-dominated. But there could be a cloud or ring of particles of different composition and/or optical depth surrounding 2059 Baboquivari. The validity of this hypothesis must be analyzed in terms of composition of the hypothetical particles, causes of a dust cloud, and criticisms of each.

In terms of composition, the simplest explanation is that these orbiting particles are olivine-/pyroxene-dominated, similar to the likely surface composition of 2059 Baboquivari. However, a 1 μm absorption feature is not detected (high z filter reflectances), but this could be due to particle size effects. Particles of a certain average size could have scattering properties that, although olivine-/pyroxene-dominated, could be scattering or re-radiating much of the incident light resulting in a higher reflectance. The particles could also be composed of more primitive materials such as ices and organics. This would lend their spectra to be lacking a 1 μm absorption feature, and perhaps have extremely red spectra, which is observed in 2059 Baboquivari's abnormally high z reflectances. This hypothesis has issues, too, however. First, 2059 Baboquivari's dynamical properties differ from most other objects containing primitive materials. If 2059 Baboquivari had a more comet-like orbit, the primitive ices or organics hypothesis would deserve more credit, but 2059 Baboquivari's orbit is distinct from Jupiter-family comets, as its Jovian Tisserand parameter of $T_J = 3.154$ and aphelion of only $Q = 4.048$ AU indicate. Second, 2059 Baboquivari's 1 μm absorption feature in the majority of its spectra implies its surface is olivine-/pyroxene-dominated and it is unlikely that an olivine-/pyroxene-dominated asteroid would contain appreciable amounts of primitive materials, although hydrated

silicates are possible (Vernazza & Beck, 2017). It is also possible that if these particles are primitive in composition, they could have originated under the surface of 2059 Baboquivari.

What about causes for 2059 Baboquivari's hypothetical dust cloud? A recent collision could have unearthed previously-subsurface materials. The ejected materials could be both silicate-dominated and/or primitive materials, depending on 2059 Baboquivari's surface composition, sub-surface composition, and the hypothetical impactor's composition. This is a somewhat likely cause, and it has been determined as a cause for some active asteroids such as 596 Scheila's activity (Jewitt, 2012). Thermal fracturing is also possible. Asteroid and rock-comet 3200 Phaethon is a prime example of how thermal fracturing near perihelion causes material to be ejected. In fact, because of this Phaethon is considered to be the parent body of the Geminids meteor stream (Li & Jewitt, 2013). Creation of a dust cloud could occur this way in 2059 Baboquivari as well, though the thermal effects would be much less extreme, as 2059 Baboquivari's perihelion is only q = 1.240 AU compared to Phaethon's q = 0.14 AU. Interestingly though, asteroid 101955 Bennu – which has orbital elements very similar to Earth (that is, it does not have a very low perihelion value) – has been observed to eject particles on a periodic basis as well, possibly from thermal fracturing due to dehydration of hydrated silicates and/or volatile release (Lauretta et al., 2019). This piece of evidence lends support to the hypothesis that 2059 Baboquivari could be releasing debris due to thermal fracturing. The only issue is that neither Phaethon nor Bennu are S-/Q-type asteroids (they belong to the C-complex), and the photometry indicates that 2059 Baboquivari has S-/Q-type features. Put another way, 2059 Baboquivari likely does not belong to the same taxonomic type that has been observed to exhibit this behavior.

Another potential cause for activity in asteroids is called "rotational instability" (Jewitt, 2012). If the centripetal acceleration of particles on the surface of an asteroid exceed the gravitational acceleration due to the asteroid's mass, material can begin to "slough off" the asteroid. The following equation from Jewitt (2012) describes the rotation rate of a strengthless object in which the centripetal acceleration equals the gravitational acceleration at its surface.

$$P_{critical} \sim 3.3k(1{,}000/\rho)^{1/2} \text{ hours}$$

$P_{critical}$ is measured in hours, k is the a/b dimension for an ellipsoidal body, and ρ is the density of the body. If 2059 Baboquivari's surface regolith has zero tensile strength (which is a good starting assumption), is spherical (k = a/b = 1), and ρ = 2,000 kg/m^3, then $P_{critical} \sim 2.33$ hours. However, if 2059 Baboquivari is ellipsoidal with k = a/b = 2 and all else being equal, $P_{critical} \sim$ 4.67 hours. Even if k = 1.5 (all else being equal), $P_{critical} \sim 3.50$ hours. So, if 2059 Baboquivari is an ellipsoidal body with strengthless regolith on its surface, it does not require a rotation rate near the "2.2 hour barrier" (Pravec & Harris, 2000; Warner et al., 2009) in order to slough off material. The rotation rate can be considerably longer (3.5+ hours) and still slough off material. How could this occur?

As mentioned earlier, YORP effects can change the rotation rate of an asteroid, so YORP effects can in theory contribute to rotational instability. So, material sloughing off due to rotation of 2059 Baboquivari could also be a cause, as the surface gravity of 2059 Baboquivari is undoubedly very low (Jewitt, 2012). This material could accumulate around 2059 Baboquivari as time passes, resulting in a relatively opaque dust cloud. This hypothesis is favorable, as it does not necessarily require one specific event (i.e., an impact) to create the dust cloud. In addition, this material will not be ejected at high speeds and therefore can accumulate, thus resulting in a relatively opaque cloud. This hypothesis also does not necessitate any particular

spectral taxonomy or surface composition; it only requires an asteroid with surface regolith or a rubble pile asteroid. It also does not necessitate any special orbital parameters outside of being a NEO; the rotational instability hypothesis actually favors NEOs due to them receiving greater Solar flux. There are two detractors to this hypothesis, however. First, no significant C filter magnitude changes were detected, so it cannot be determined that 2059 Baboquivari's rotation period is short enough to cause rotational instability. But, since light from 2059 Baboquivari includes both the asteroid and the hypothetical cloud, the cloud *could* obscure 2059 Baboquivari's surface and complicate determining brightness changes. The second detractor is that from Jewitt (2012) rotational instability is most favorable for only smaller < ~1 km diameter asteroids, and 2059 Baboquivari's H magnitude of 16.0 implies a diameter of ~2 km. However, Pravec and Harris (2000) noted that due to their fast rotation and relatively flat light curves most < ~1 km asteroids are monolithic and spheroidal, implying they could have lost significant mass due to rotational spin-up. Could 2059 Baboquivari be in the beginning stages of this? All in all, this hypothesis is the most appealing out of the dust cloud causes due to its simplicity.

Either of these explanations could explain why 2059 Baboquivari exhibits z filter photometric variability on short ~12 minute timescales while C filter magnitudes remain relatively constant, as well as a stark increase in brightness from 18 Nov to 21 Nov on the order of at least ~0.5 magnitudes. All explanations still have issues that could only be resolved by further study, but at this time the most likely reason is a dust cloud surrounding 2059 Baboquivari composed of either pyroxene/olivine or more primitive materials that has a period of revolution different from 2059 Baboquivari's rotation period.

4. Moon or Moonlet

A moon or moonlet with a different composition from 2059 Baboquivari would also cause a variable spectrum, depending on the moon's composition, size, and orbital properties. This hypothesis, in order to be valid, requires stringent conditions to be met. First, the moon would have to have a distinct and different surface composition than that of 2059 Baboquivari. In this case, the moon would have a red, featureless spectrum not unlike that of a X-/P-/D-type asteroid. Unless the moon was serendipitously captured into orbit around 2059 Baboquivari, a collision-ejection-coalescence event would not be likely and still meet the compositional requirement. Second, the moon would have to be large enough and have a specific orbital period, semi-major axis, and inclination to at least partially obscure 2059 Baboquivari in the 2059 Baboquivari-Earth line-of-sight. Put all together, the moon hypothesis is not very likely, although not totally out of the question.

5. Kron Photometry Issues

Another reason why z filter photometry may be highly variable is due to the methods used for photometry. There is a correlation here, as g, r, and i filter images were taken in 60 second exposures and exhibit low photometric variability, and z filter images were taken in 150 second exposures and exhibit high photometric variability. Thus, there could be an issue with the Kron algorithm and how it performs photometry on the asteroid. Although this is not likely because the Kron algorithm was developed to perform photometry for extended, dim objects like galaxies (Kron, 1980), it will take further analysis to rule out.

The first step is to perform a "sanity check" and examine how 2.5" aperture photometry compares to Kron photometry for 2059 Baboquivari. The Kron instrumental magnitude vs time

graphs are shown in Figures 39a – d., while the aperture photometry instrumental magnitude vs time graphs are shown below in Figure 41.

Figures 41a – d:

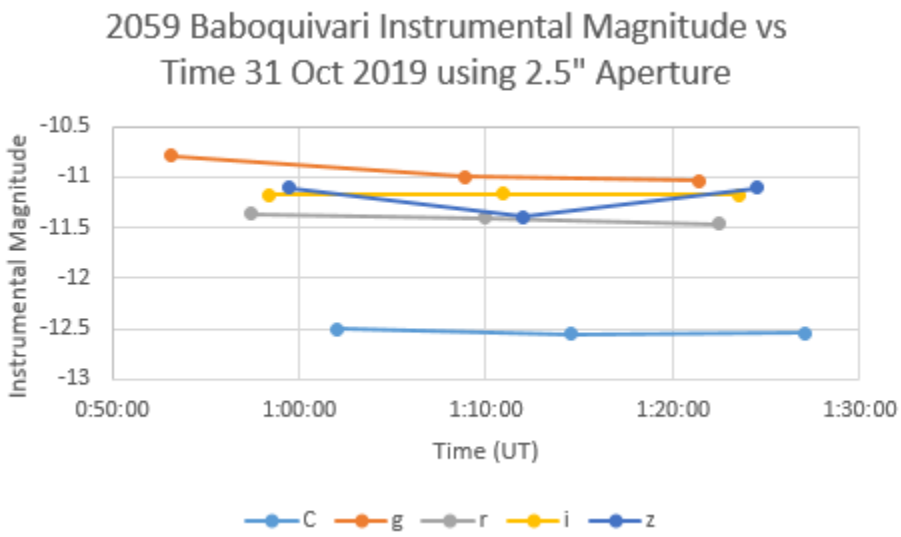

41a: 2059 Baboquivari instrumental magnitude vs time graph for 31 Oct 2019. These instrumental magnitudes were calculated using 2.5” aperture photometry.

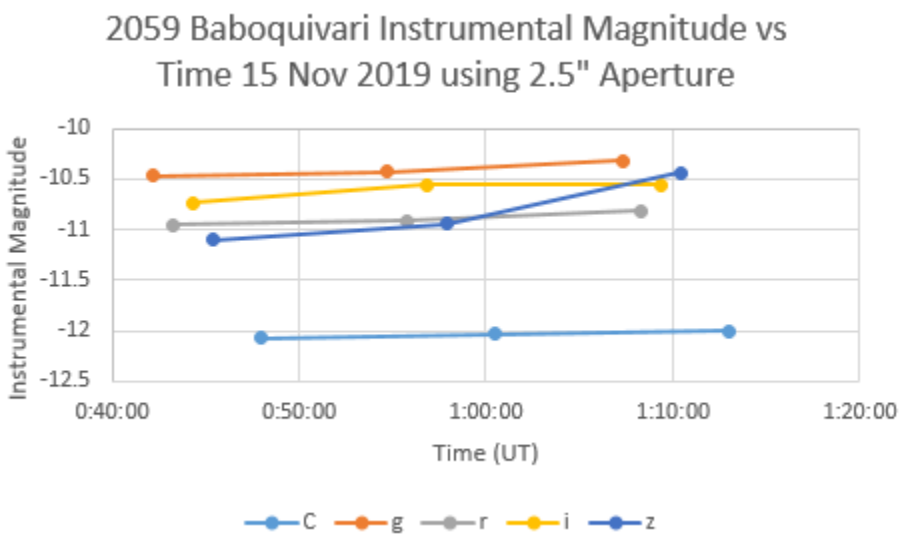

41b: 2059 Baboquivari instrumental magnitude vs time graph for 15 Nov 2019. These instrumental magnitudes were calculated using 2.5" aperture photometry.

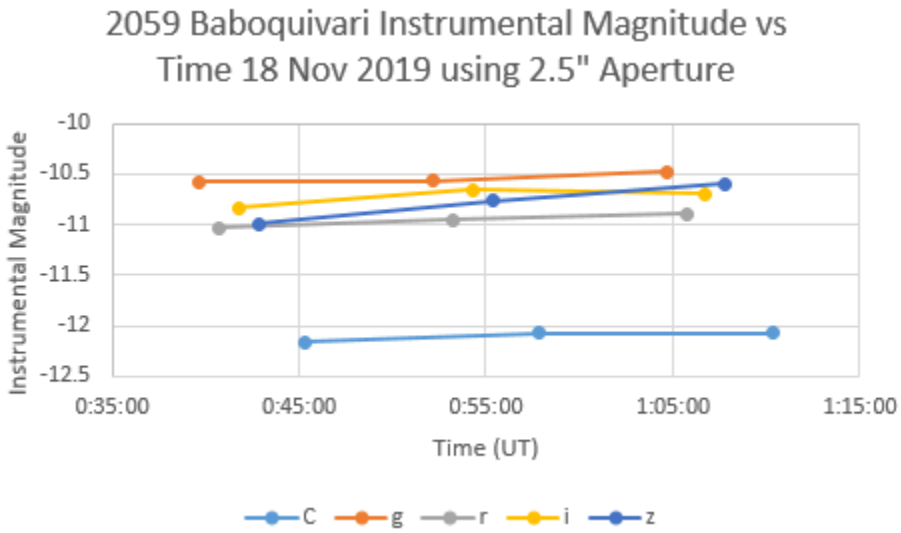

41c: 2059 Baboquivari instrumental magnitude vs time graph for 18 Nov 2019. These instrumental magnitudes were calculated using 2.5" aperture photometry.

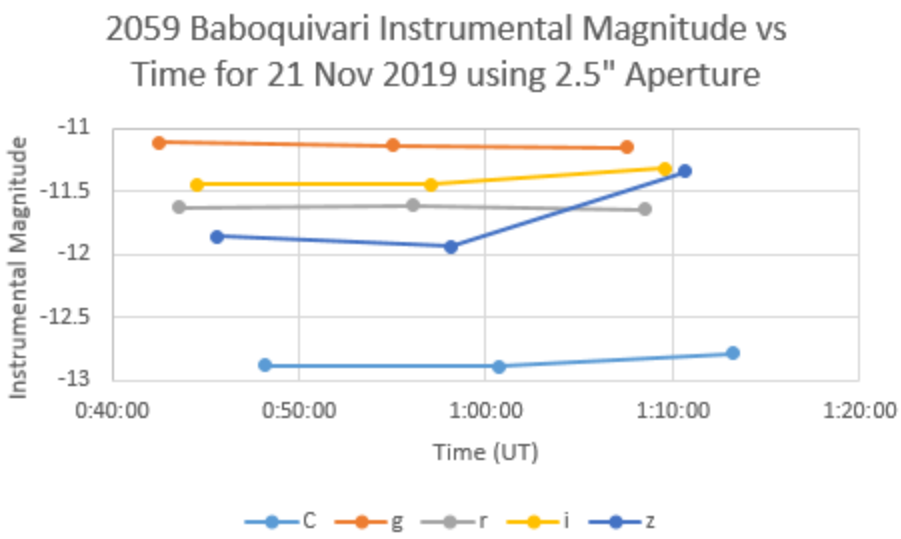

41d: 2059 Baboquivari instrumental magnitude vs time graph for 21 Nov 2019. These instrumental magnitudes were calculated using 2.5" aperture photometry.

It is evident that the aperture photometry method produces higher variability than Kron photometry, but qualitatively the two methods agree with each other. Thus, either both aperture photometry and Kron photometry are incorrect methods to use on 2059 Baboquivari, or both are "right" but Kron may be more precise.

The next step is to look at another set of images that were taken using 150 second exposures: B filter images. BVRI instrumental magnitudes are compared below in Figures 42a – d.

Figures 42a – d:

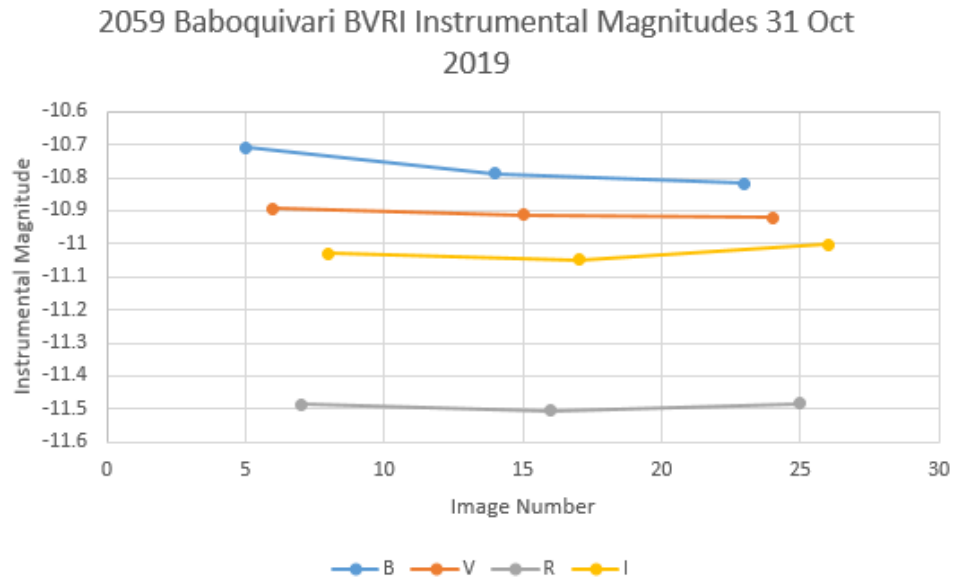

42a: 2059 Baboquivari BVRI instrumental magnitude vs time graph for 31 Oct 2019.

Instrumental magnitudes were calculated using Kron photometry.

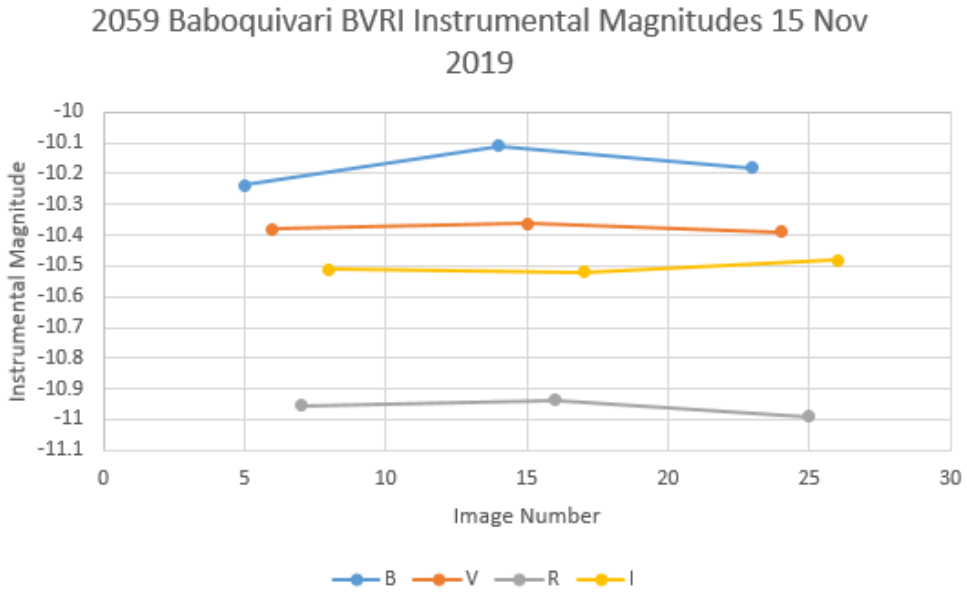

42b: 2059 Baboquivari BVRI instrumental magnitude vs time graph for 15 Nov 2019.

Instrumental magnitudes were calculated using Kron photometry.

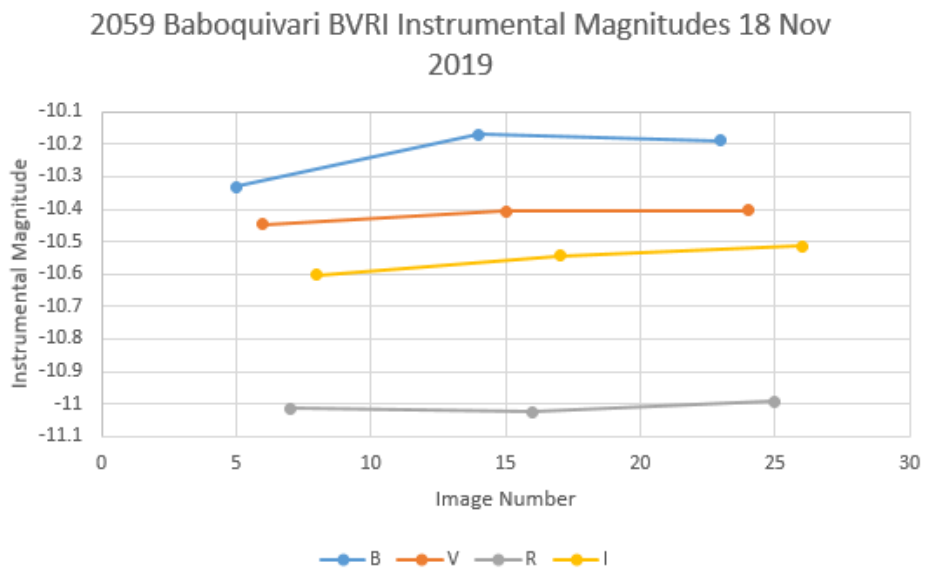

42c: 2059 Baboquivari BVRI instrumental magnitude vs time graph for 18 Nov 2019.

Instrumental magnitudes were calculated using Kron photometry.

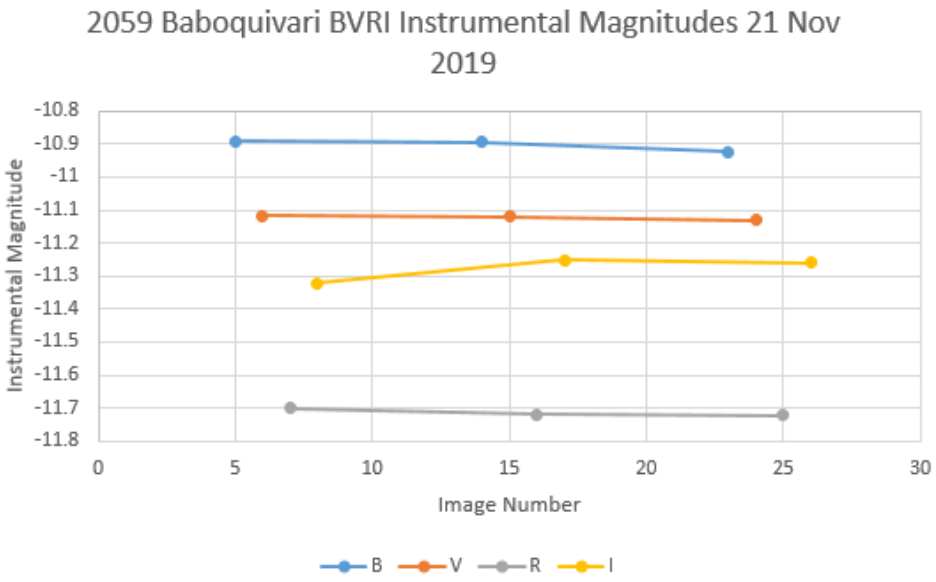

42d: 2059 Baboquivari BVRI instrumental magnitude vs time graph for 21 Nov 2019.

Instrumental magnitudes were calculated using Kron photometry.

By examining these graphs it is clear that B filter images indeed exhibit higher variability than V, R, and I filter images. V, R, and I filter images used 60 second exposures, similarly to g, r, and i. From these, V, R, and I filter instrumental magnitudes typically vary by only ~0.05 magnitudes, although I filter instrumental magnitudes on 18 Nov and 21 Nov vary by 0.09 and 0.06 magnitudes, respectively. The B filter instrumental magnitudes vary by considerably more. On 15 Nov the B filter instrumental magnitude varied by ~0.13 magnitudes and on 18 Nov the instrumental magnitude varied by ~0.16 magnitudes. Although this is significant, this variability is still much smaller than the ~0.4 magnitude variability in z filter images from 15 and 21 Nov. This analysis shows that the Kron algorithm is probably not solely responsible for 2059 Baboquivari's photometric variability.

It is also useful to examine the directions in which these magnitude changes occur through different filters. Generally, all filters (including B) except for z trend in the same direction with their magnitude changes. Magnitude changes in the z filter, however, are sporadic and lack any discernable pattern.

So, there is a positive correlation between exposure time and photometric variability when using Kron photometry on images of 2059 Baboquivari. It is not substantiated that this variability is a result of the Kron algorithm, though. In longer images, light from the asteroid will cover more pixels than in shorter images and will appear more "streaked," but the Kron algorithm was created to accurately perform photometry on extended objects like these. Thus, it cannot be ruled out that the Kron algorithm used *contributes* to 2059 Baboquivari's photometric variability. But since z filter variability is much larger than B filter variability, this fact puts into doubt that the Kron algorithm is solely or even primarily responsible. It should also be mentioned that the Kron algorithm has been used successfully on extended objects like galaxies

and that Source Extractor (in which both aperture and Kron photometry were performed) is a peer-reviewed and accepted method for asteroid photometry. In addition, photometric variations are smaller using Kron-derived instrumental magnitudes versus using aperture photometry-derived instrumental magnitudes. As a result, issues with using Kron photometry are not very likely.

In addition, the Kron algorithm does not capture all the light from an object while performing photometry. This effect is also magnitude-dependent. In order to understand this more fully, Figure 43 is shown below.

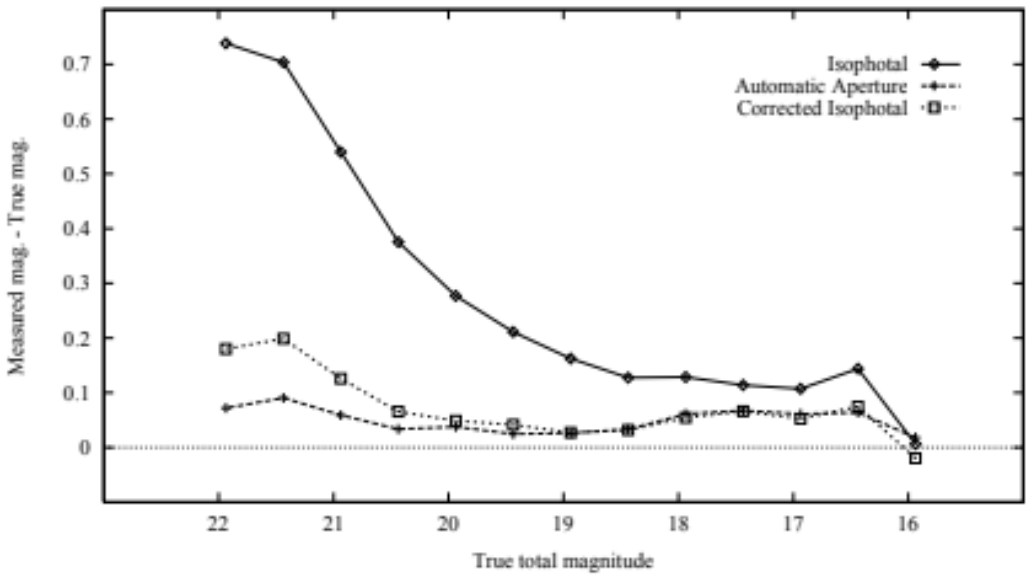

Figure 43: Comparison of true magnitude vs. measured magnitude for photometric algorithms used in Source Extractor. The Kron algorithm is labelled as "Automatic Aperture" (Source Extractor Manual).

Fortunately, the calibrated magnitudes of 2059 Baboquivari calculated from Kron photometry fall within 16 – 17.5 magnitudes. The values for measured magnitude vs. true

magnitude all fall within 0.02 – 0.07. As a result, this offset can be defined as roughly systematic. Comparisons between photometric spectra with and without this correction are shown below in Figures 44a – c.

Figures 44a – c:

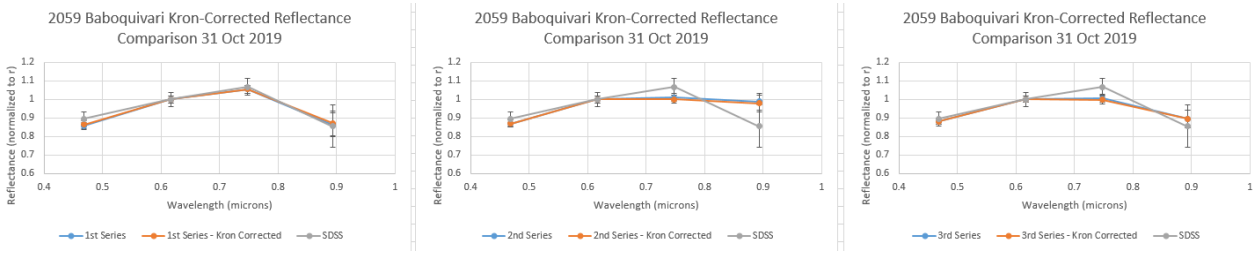

44a: Photometric spectra of 2059 Baboquivari with and without the Kron algorithm magnitude correction from 31 Oct 2019.

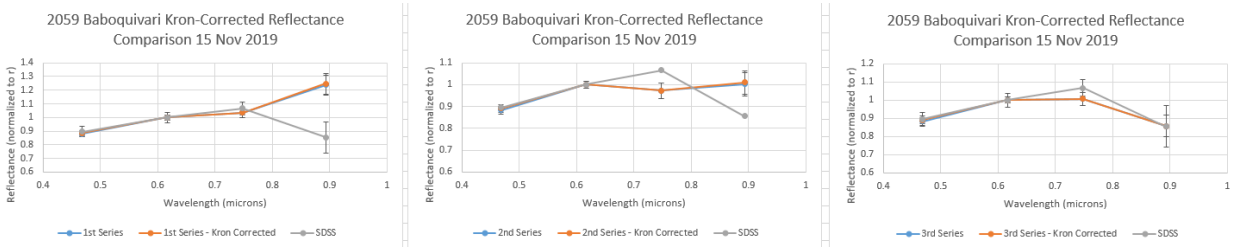

44b: Photometric spectra of 2059 Baboquivari with and without the Kron algorithm magnitude correction from 15 Nov 2019.

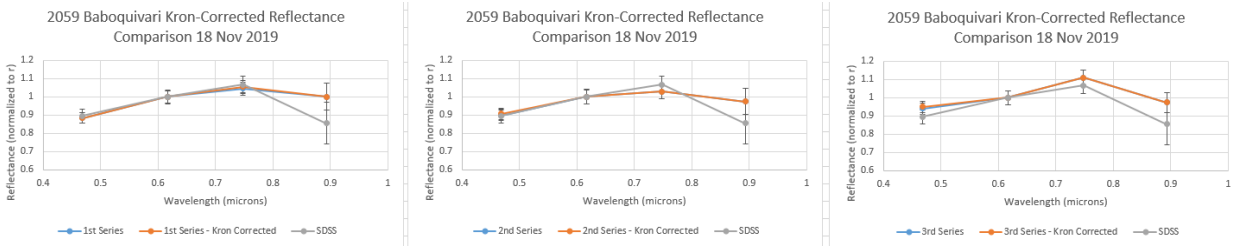

44c: Photometric spectra of 2059 Baboquivari with and without the Kron algorithm magnitude correction from 18 Nov 2019.

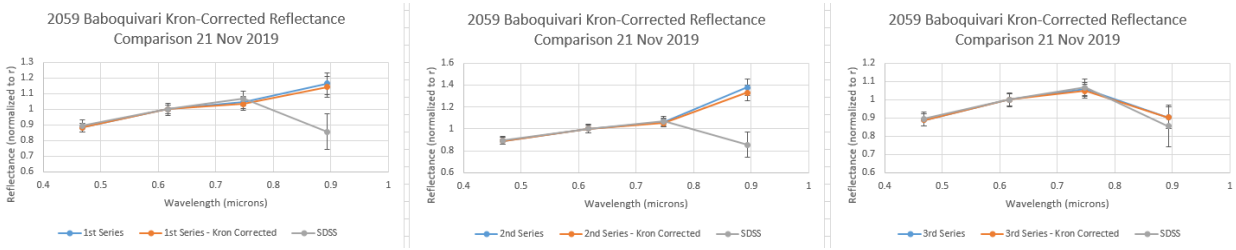

44d: Photometric spectra of 2059 Baboquivari with and without the Kron algorithm magnitude correction from 21 Nov 2019.

It is clear from these figures that the Kron algorithm magnitude correction is minor for all filters, and roughly systematic. Performing this correction does not appreciably change 2059 Baboquivari's photometric spectra.

6. Filter Wheel Error

Another possibility for 2059 Baboquivari's variability is a filter wheel error in the telescope. Perhaps images labelled as z filter images were actually taken in a different filter. How likely is this, and is there a way to rule this out?

Fortunately, this is rather simple to test. The z filter has low quantum efficiency, and so requires longer exposure times to create high enough SNR for reliable photometry. The other

filters, save for B, have higher quantum efficiencies and thus need less time to achieve the same SNR. If an image labelled as z filter was actually taken in g, r, i, V, R, or I, one would expect to see much higher counts in these "z filter images." Indeed, one should see ~2.5x higher counts in these erroneously-labelled z filter images as the exposure times were 2.5x as long (150 seconds vs 60 seconds). So, a raw counts analysis was performed on all images of 2059 Baboquivari and are shown below in Figures 45a – d, Tables 17a – d, Figure 46, and Figure 47.

Figures 45a – d:

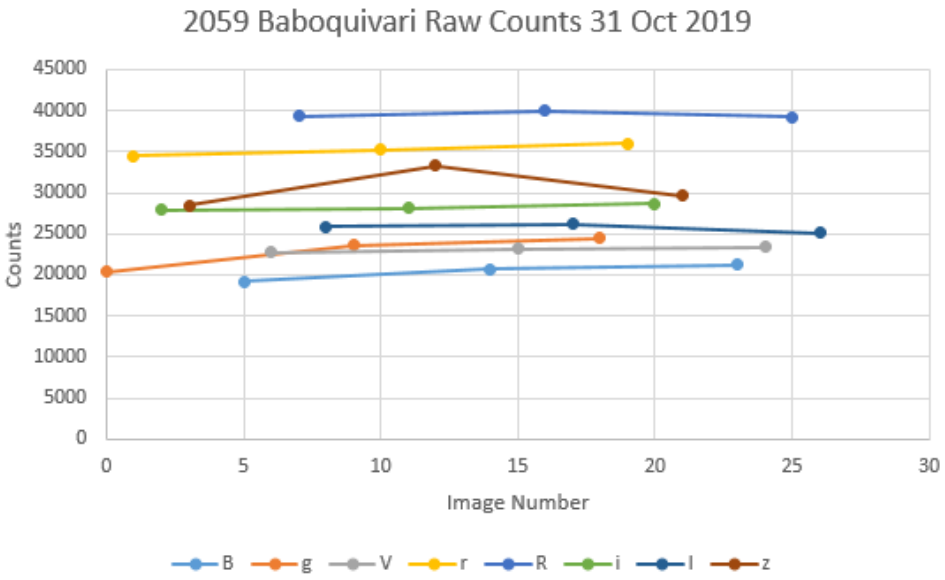

45a: Counts per image number for 2059 Baboquivari on 31 Oct 2019. Note changes in counts for B and g, but especially for z. The z filter magnitudes exhibited some variability during this night.

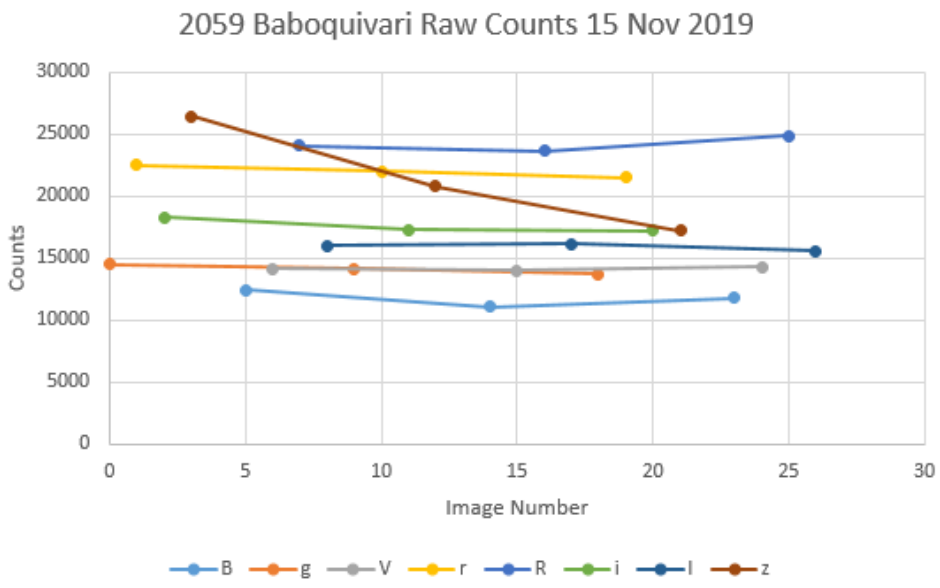

45b: Counts per image number for 2059 Baboquivari on 15 Nov 2019. Note changes in counts for B and g, but especially for z. The z filter magnitudes exhibited significant variable this night.

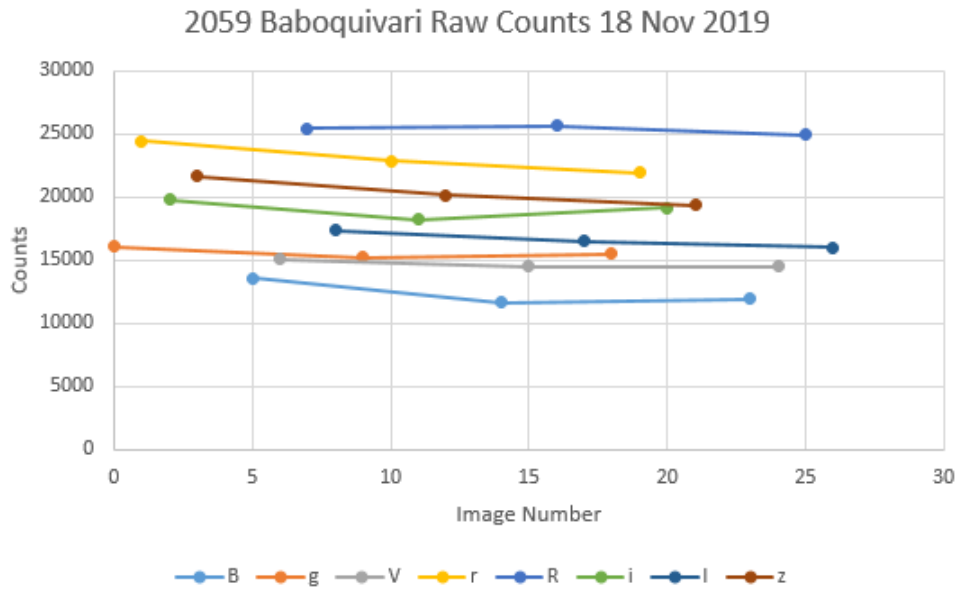

45c: Counts per image number for 2059 Baboquivari on 18 Nov 2019. Note changes in counts for B and g, but especially for z. The z filter magnitudes did not exhibit significant variability during this night.

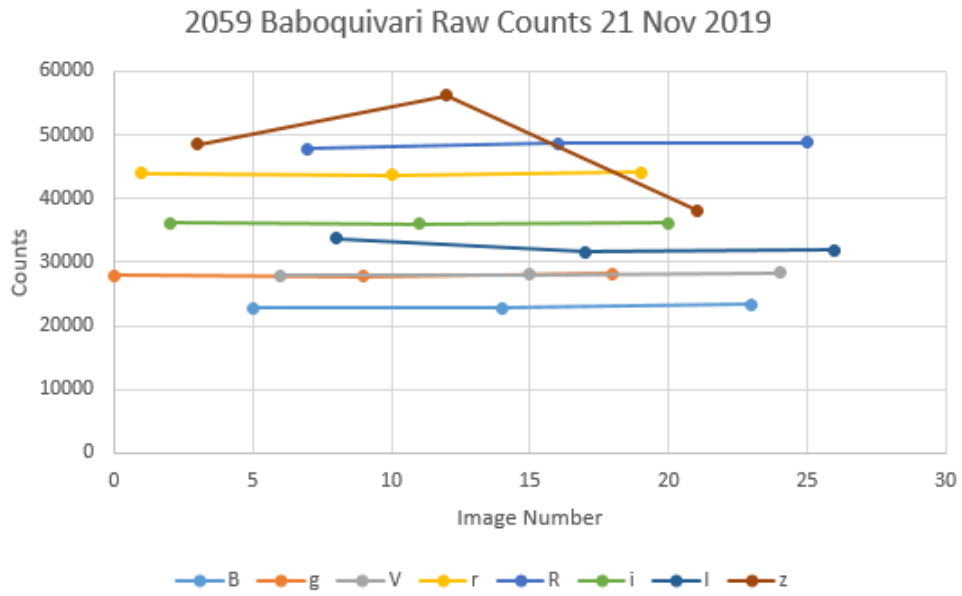

45d: Counts per image number for 2059 Baboquivari on 21 Nov 2019. Note changes in counts for B and g, but especially for z. The z filter magnitudes exhibited very significant variability during this night.

Tables 17a – d:

31-Oct	Delta Counts	Average Counts	% Change
B	2020.719879	20372.62039	9.918802
g	4038.009465	20755.51205	19.45511851
V	620.2283591	21732.11292	2.85397173
r	1474.766189	22787.43444	6.471839528
R	795.2422929	23579.77435	3.372561081
i	731.9714142	23448.44837	3.12161983
I	1076.710271	23101.52791	4.660775142
z	4830.537248	27029.38241	17.87143033

17a: Table of Δcounts, average counts in each filter, and the percent change in counts from 2059 Baboquivari on 31 Oct 2019.

15-Nov	Delta Counts	Average Counts	% Change
B	1374.456922	11767.14981	11.68045741
g	728.3025748	12452.20803	5.848782586
V	350.7349688	13484.18784	2.60108338
r	1004.604504	14133.72028	7.107856129
R	1222.275019	14032.05923	8.710589078
i	1103.644979	13974.61734	7.897496955
I	570.1690445	14165.62389	4.025018939
z	9191.750376	16936.96586	54.27034837

17b: Table of Δcounts, average counts in each filter, and the percent change in counts from 2059 Baboquivari on 15 Nov 2019. Notice the percent change for the z filter.

18-Nov	Delta Counts	Average Counts	% Change
B	1880.710624	12383.59455	15.18711402
g	802.0435022	13218.8674	6.06741469
V	580.3809331	14413.69595	4.026593423
r	2480.898854	15620.15076	15.88268188
R	193.07701	15292.70677	1.262543073
i	1543.773829	15052.52721	10.25591123
I	1371.435043	14710.57703	9.322782109
z	2250.764332	17830.30649	12.62325094

17c: Table of Δcounts, average counts in each filter, and the percent change in counts from 2059 Baboquivari on 18 Nov 2019.

21-Nov	Delta Counts	Average Counts	% Change
B	677.8006545	22979.72257	2.94955978
g	456.4505719	24696.26424	1.848257564
V	362.8496633	26354.40477	1.376808418
r	444.9080078	27960.42781	1.59120601
R	947.8993989	27986.14336	3.387031169
i	209.2940292	28074.38088	0.745498289
I	2102.64468	28105.63139	7.481222003
z	18096.30588	33464.4007	54.07628855

17d: Table of Δcounts, average counts in each filter, and the percent change in counts from 2059 Baboquivari on 21 Nov 2019. Notice the percent change in z filter counts.

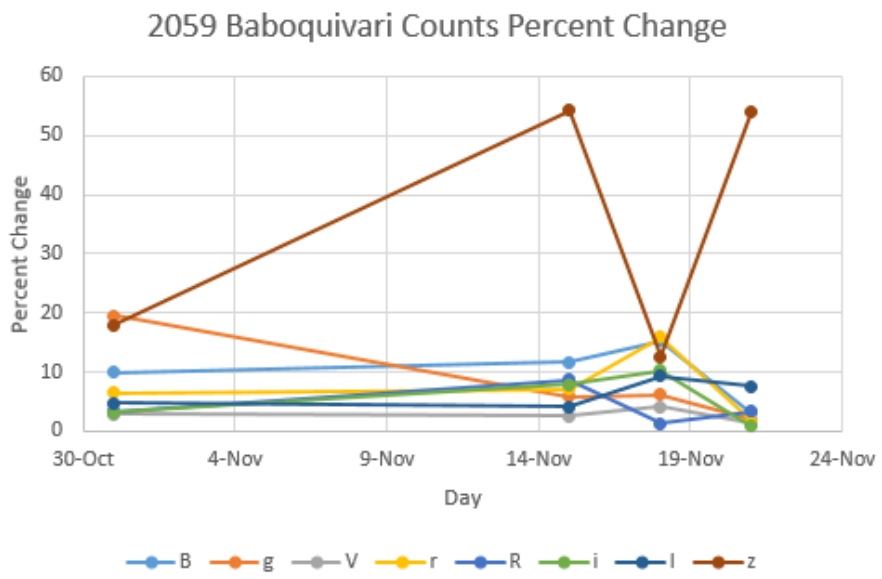

Figure 46: This graph illustrates the percent changes of counts per filter per night for 2059 Baboquivari. Counts from all filters exhibit variability, but the z filter's variability dwarfs all others.

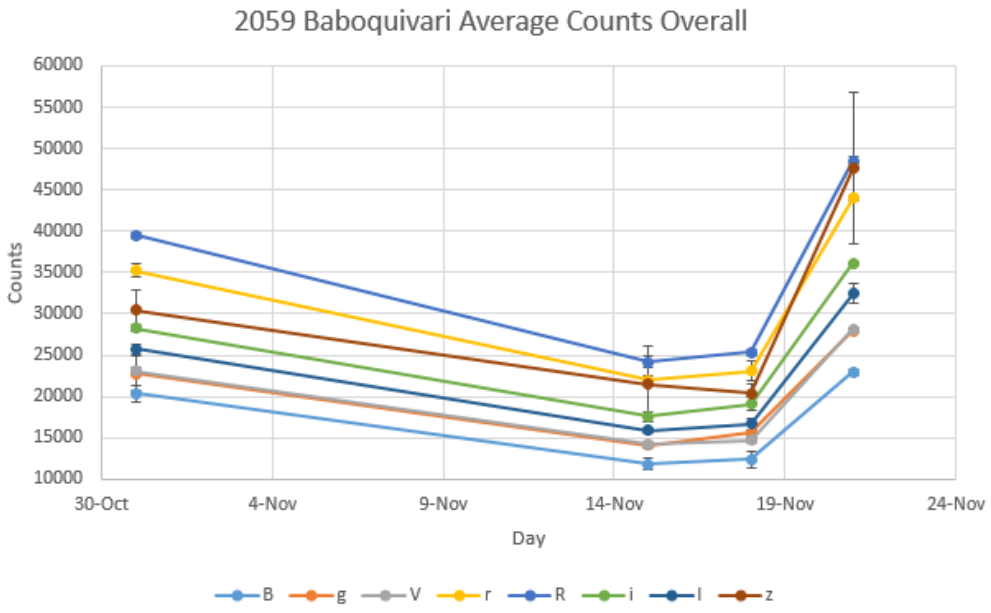

Figure 47: This graph shows the average counts per filter, per night for 2059 Baboquivari. Note the general decrease in counts for each filter from 31 Oct – 18 Nov, then a drastic increase in counts for all filters on 21 Nov.

It is clear that the z filter images exhibit high variability in raw counts, but never nearly as high as the 2.5x required to prove a filter wheel error plausible, and one can see that the variability in counts for the z filter dwarfs all other filters, even the B filter. That is not to say there is not *some* variability in B, but z filter counts variability is much larger, in particular, on 15 Nov and 21 Nov. In addition, in most filters if there are changes in counts, they trend the same direction, while the z filter does not necessarily do the same. Also, note that in terms of percent change over one night of observing, z filter counts dwarf all other filters' counts (Figure 42). Lastly, one can see the general decrease in counts from 2059 Baboquivari from 31 Oct – 18 Nov, then a drastic increase in counts on 21 Nov 2019.

As a result, filter wheel errors have been ruled out as the source of 2059 Baboquivari's z filter variability.

All in all, the reason(s) for 2059 Baboquivari's z filter variability are not solved, but some can be ruled out. Rotational heterogeneities, a moon/moonlet system, and filter wheel errors are likely not the source of 2059 Baboquivari's variability. The Kron algorithm used for photometry *could* have contributed to the variability, but since the Kron algorithm has been used successfully on extended objects like galaxies and that Source Extractor (in which both aperture and Kron photometry were performed) is a peer-reviewed and accepted method for asteroid photometry, errors in data analysis methods are not likely. The presence, composition, and cause(s) of a dust/debris cloud/ring around 2059 Baboquivari cannot be constrained further, but this hypothesis has some appeal, as it could account for the rapid change in z filter reflectance; thus it is the most likely source of 2059 Baboquivari's mysterious photometric variability.

2059 Baboquivari Phase Angle Relationships

The i – g slope and z – i band depth of 2059 Baboquivari's spectrum were also compared to its phase angle of observation (Carvano & Davalos, 2015). Since SDSS observed 2059 Baboquivari at a phase angle of 22.1 degrees and this study's observations were performed at phase angles of ~45 – 50 degrees, any significant dependence of slope or band depth on phase angle should be observed. The graphs are shown in Figures 48a – b.

Figures 48a – b:

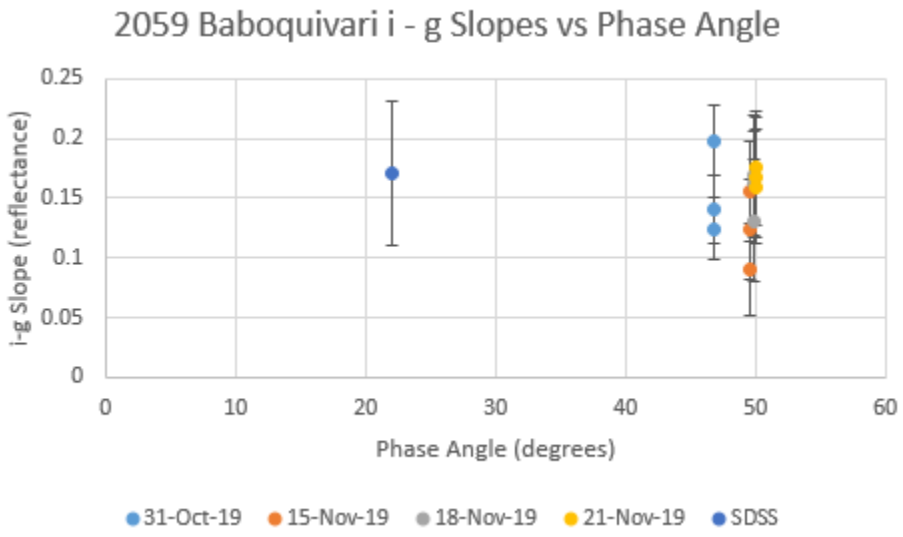

48a: 2059 Baboquivari i –g slope vs phase angle.

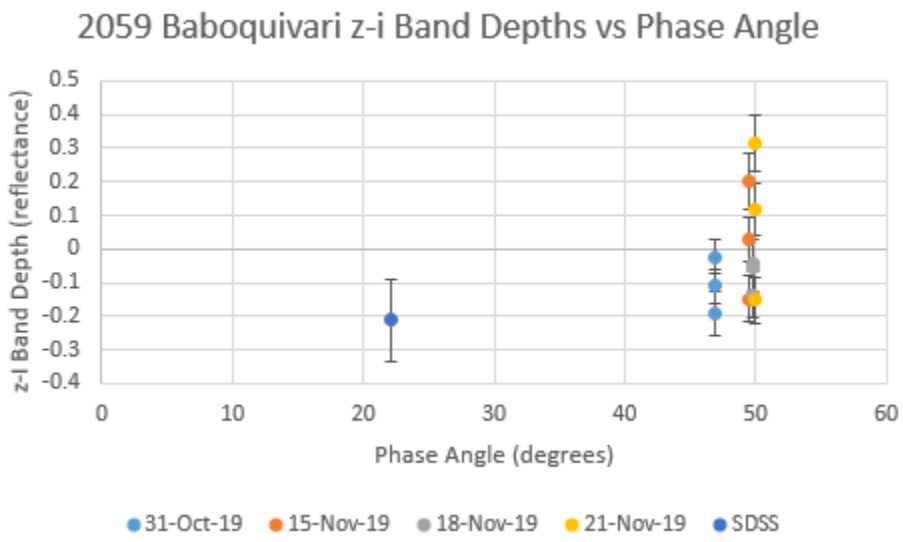

48b: 2059 Baboquivari z – i band depth vs phase angle.

Although phase angle sampling is somewhat sparse, these figures show that there is not a significant dependence of i – g slope on phase angle. In fact, i – g slope may slightly anti-correlate with phase angle. In addition, z – i band depth vs phase angle shows a slight anti-correlation; as phase angle increases, z – i band depth decreases generally. This z – i vs phase angle correlation is true even when high z filter reflectances are discarded.

This is an interesting result, as a minority of asteroids have neutral or negative relationships between visible spectral slope and phase angle (Sanchez et al., 2012; Carvano & Davalos, 2015). Table 18 shows Table 1 from Carvano and Davalos (2015) shows the distribution of correlations between slope and band depth and phase angle.

Sample	Parameter	Total	Correlation (%)	No correlation (%)	Anticorrelation (%)
All	*slope*	2077	1150 (55.4)	508 (24.4)	419 (20.2)
C, X, D	*slope*	626	295 (47.1)	164 (38.2)	167 (26.7)
V, S, Q	*slope*	1164	692 (59.5)	274 (23.5)	198 (17.0)
V, S, Q	*bd*	1164	480 (41.2)	310 (26.6)	374 (32.2)

Table 18: Table 1 from Carvano and Davalos (2015) showing phase angle and band depth relationships for asteroids found in the MOC4.

From this table, it shows 59.5% of asteroids classified as V-/S-/Q-type have a positive correlation between slope and phase angle, but only 47.1% of C-/X-/D-types show the same positive correlation. In terms of anti-correlations, this is exhibited for 17% of V-/S-/Q-types and 26.7% of C-/X-/D-types. Worthy to note is that 38.2% of C-/X-/D-types show no correlation between slope and phase angle. In order to investigate phase angle relationships further, i – g slope vs phase angle is shown in Figures 49a – b separated for spectra of 2059 Baboquivari that appear more S-/Q-type against those that appear more C-/X-/P-/D-type.

Figures 49a – b:

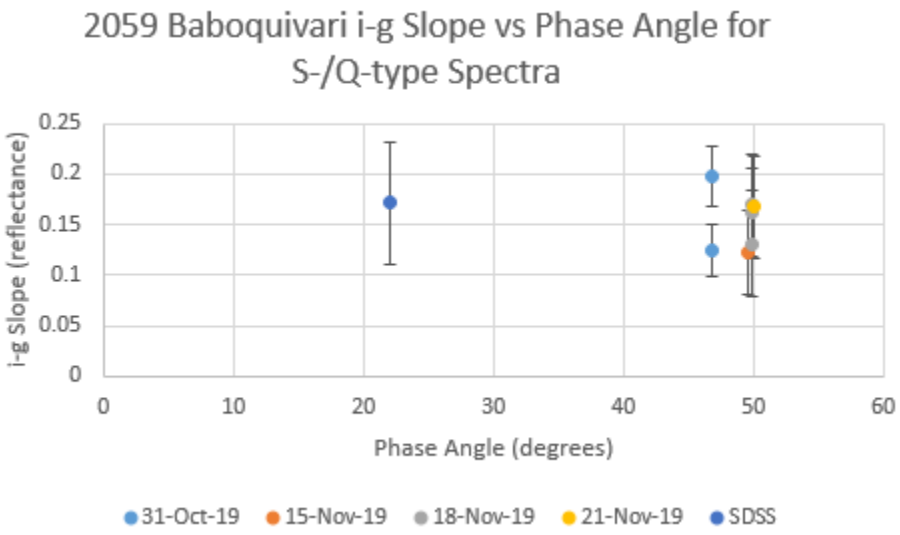

49a: 2059 Baboquivari i – g slope vs phase angle for photometric spectra classified as S-/Q-type.

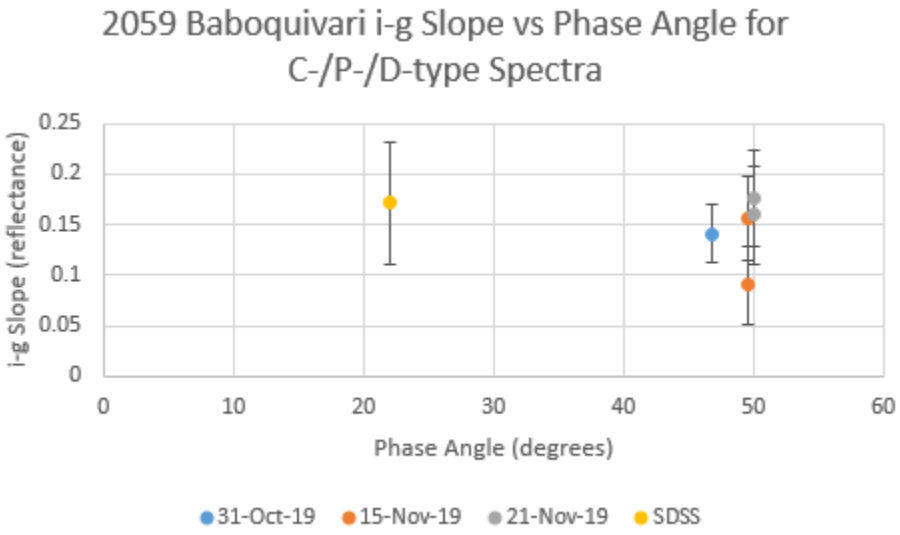

49b: 2059 Baboquivari i – g slope vs phase angle for photometric spectra classified as C-/P-/D-type.

It is clear from these graphs that neither slope distributions appear significantly different from one another. This is not a surprising result, as 2059 Baboquivari's i – g reflectance values do not vary nearly as much as its z filter reflectances.

Next, the z – i band depth was explored for only spectra of 2059 Baboquivari that appeared S-/Q-type. They are shown in Figure 50.

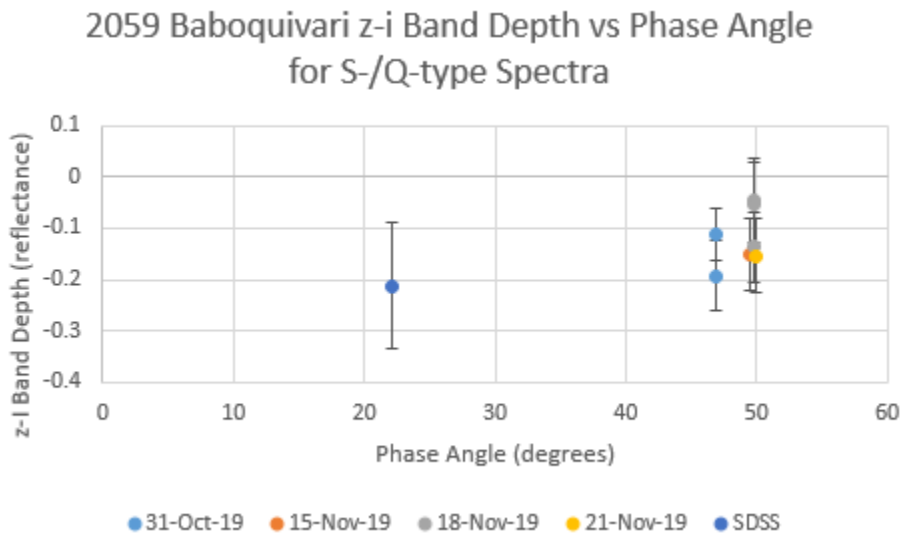

Figure 50: 2059 Baboquivari z – i band depth vs phase angle for photometric spectra classified as S-/Q-type.

The z – i band depth vs phase angle again shows a small anti-correlation with respect to phase angle. Are there any constraints that can be made about the surface of 2059 Baboquivari from these data? First, it is not entirely surprising that 2059 Baboquivari's spectra show weak correlations between slope/band depth and phase angle, as sizable minorities of asteroids in the MOC4 fall into the same category (Carvano & Davalos, 2015). As for constraints of its surface,

one would have look at what would cause zero or an anti-correlation between slope/band depth vs phase angle. Some possible reasons are the following:

1. Less-opaque surface particles, resulting in higher normal reflectance and smaller phase coefficient β (Gradie & Veverka, 1986).
2. Surface particles that exhibit more back-scattering than forward-scattering, which could result in a negative correlation between spectral slope and phase angle (Carvano & Davalos, 2015).
3. Since macroscopic roughness contributes to increases in phase reddening, 2059 Baboquivari may generally lack macroscopic roughness on its surface (Carvano & Davalos, 2015).
4. A less-ellipsoidal shape for 2059 Baboquivari, as more ellipsoidal shapes produce a stronger spectral slope vs phase angle relationship (Carvano & Davalos, 2015).

Any of these reasons could be true for 2059 Baboquivari, or multiple of them. Future studies will have to be conducted in order to constrain 2059 Baboquivari's surface properties further.

96744 (1999 OW3) Discussion

Next, 96744 (1999 OW3) will be discussed. Recall, all analyses must point back to the Statement of the Problem:

- Is the photometry found in the SDSS MOC4 database for 2059 Baboquivari and 96744 (1999 OW3) consistently repeatable?
- If not consistently repeatable, what are the reason(s) for their photometric variability?

Normalized photometric spectra for 96744 (1999 OW3) could not be created because the object was observed at such a low declination (~-65 degrees). No photometric survey has reliably obtained magnitudes of stars that far south, so only instrumental magnitudes could be used for the analysis. Thus, only differential photometry was performed. However, strides can be made to address these questions.

Contrary to observations of 2059 Baboquivari, observation runs of 96744 (1999 OW3) ran for much longer, from ~55 minutes all the way up to ~160 minutes. This allowed for a thorough examination of instrumental magnitude variations and construction of light curves. Light curves in g, r, i, and z filters are shown above in Figures 38a – c.

96744 (1999 OW3) Rotational Analysis Discussion

As mentioned in the Analysis section, the C filter light curve shows instrumental magnitude variations of ~0.50 to 0.60 magnitudes throughout the observation runs. By combining observations on 10 Jan 2020, there appears to be a ~0.65 – 0.70 instrumental magnitude variation through the night of observations. The Analysis section also mentioned max-to-max and min-to-min time differences of ~2 hours, and it was concluded that 96744 (1999 OW3) could have a rotation period of a multiple of ~2 hours. Below in Table 19 shows the times between maxima and minima in the C filter light curve from 10 Jan 2020.

Time of Minumum (fraction of day)	Delta Time (hours)
0.069	
0.150	1.944
0.224	1.788
0.310	2.058
Time of Maximum (fraction of day)	Delta Time (hours)
0.112	
0.194	1.980
0.272	1.867

Table 19: This table displays the times between maxima and minima in the C filter light curve of 96744 (1999 OW3) from observations taken on 10 Jan 2020. The left column is the time of maxima and minima in the C filter light curve in fractions of a day. The right column shows the time in hours from the last maximum or minimum.

In a way similar to 2059 Baboquivari, in order to determine more properties of 96744 (1999 OW3), i – g and z – i magnitude differences were analyzed. Unfortunately, these observations cannot be directly compared to photometry of 96744 (1999 OW3) in the MOC4, but they can be compared from observation-to-observation and night-to-night. In addition, these i – g and z – i magnitude differences can be compared as a function of time and also with respect to the C filter light curve in order to examine if any patterns repeat themselves. Below in Figures 51 and 52 are i – g and z – i graphs with respect to time from 10 Jan 2020 and 11 Jan 2020, shown in comparison to 96744 (1999 OW3)'s C filter light curve.

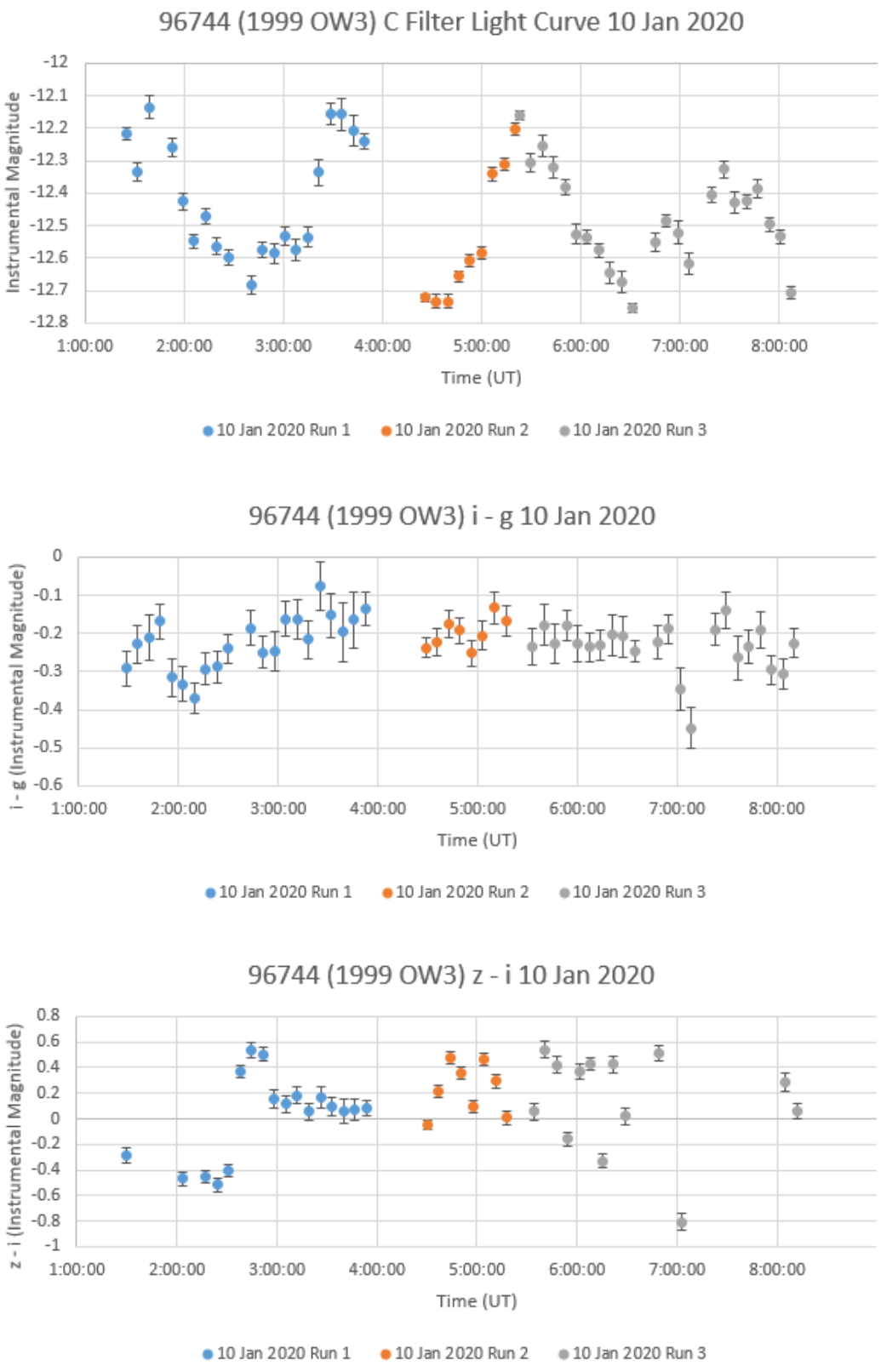

Figure 51: 96744 (1999 OW3) C filter light curve, i – g, and z – i vs time graphs for 10 Jan 2020.

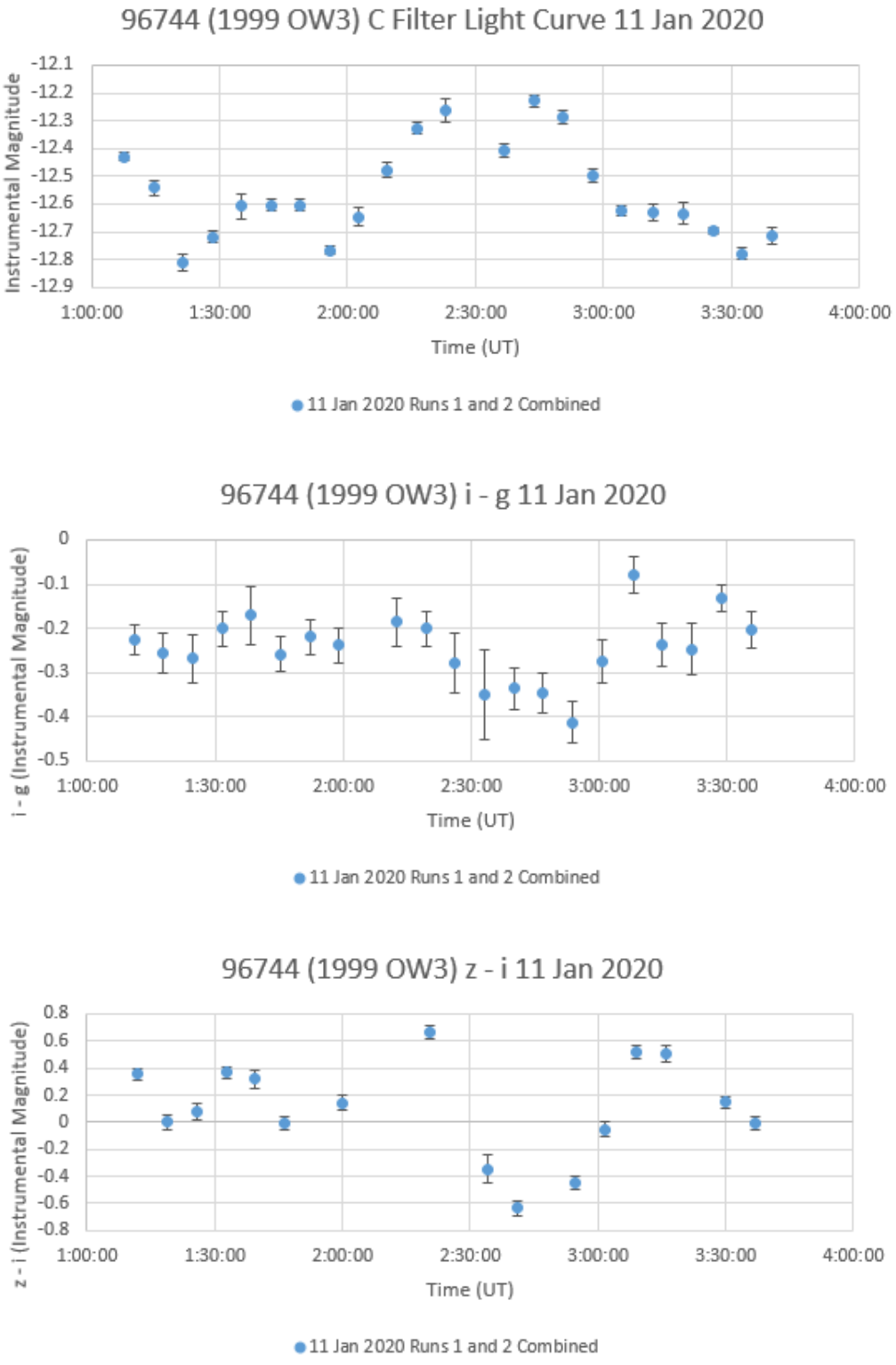

Figure 52: 96744 (1999 OW3) C filter light curve, i – g, and z – i vs time graphs for 11 Jan 2020.

The first property apparent from these graphs is that i – g and z – i are not consistent throughout observation runs. In addition, there appears to be a correlation between i – g and z – i and 96744 (1999 OW3)'s C filter light curve. At least in one of the legs of the C filter light curve, as 96744 (1999 OW3)'s instrumental magnitude decreases (96744 (1999 OW3) gets brighter), i – g becomes more negative than average and z – i flips from positive to negative. Then, the i – g and z – i values rapidly switch back to what they are for the majority of the rest of the light curves. This is significant because not only is there a correlation between i – g and C filter instrumental magnitude variation, and z – i and C filter instrumental magnitude variation, but also a correlation between i – g *and* z – i *and* C filter instrumental magnitude variation. Below in Figures 53 and 54 are graphs of C filter light curves, i – g, and z – i graphs from 10 Jan 2020, with those from 11 Jan 2020 superimposed upon them.

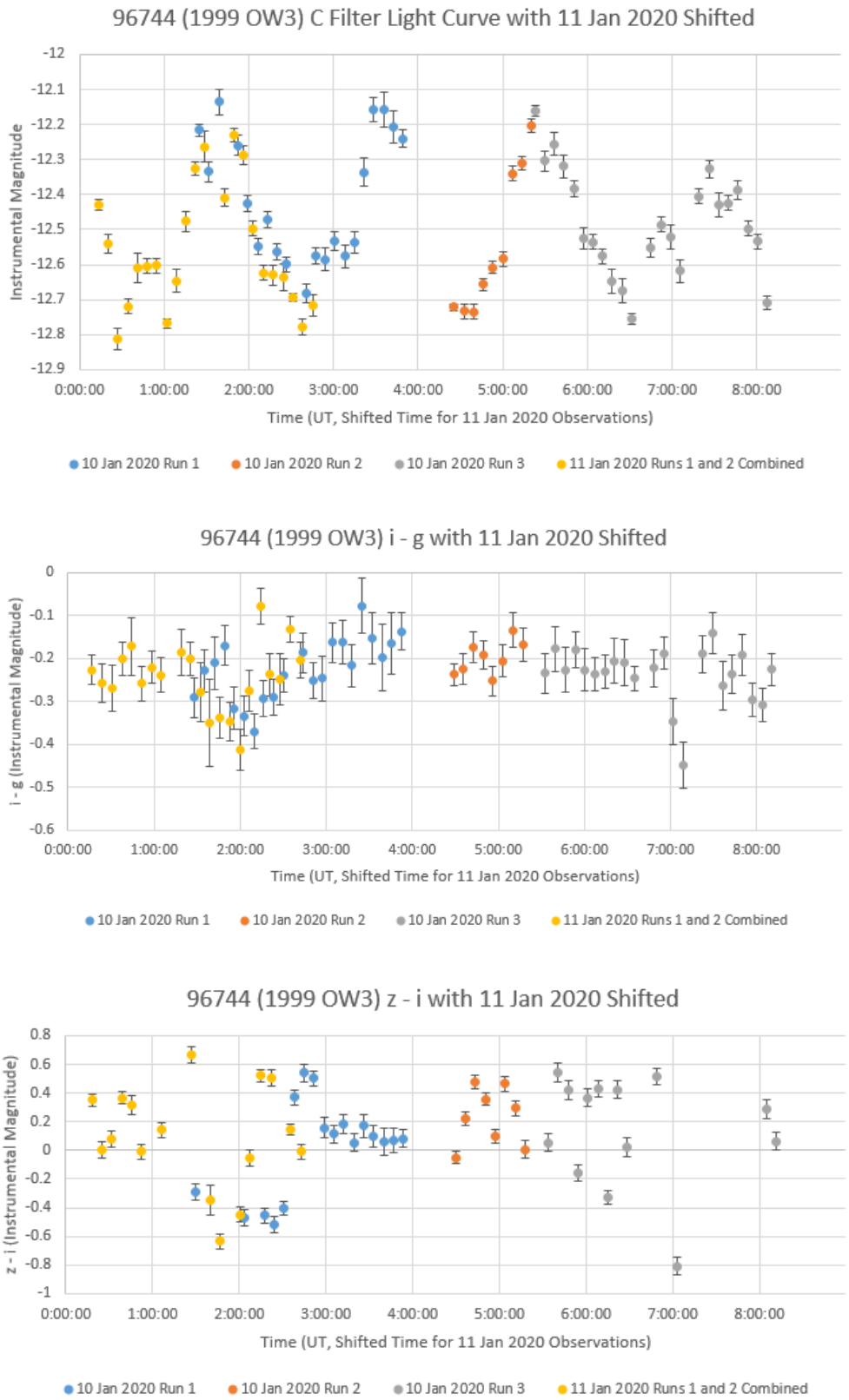

Figure 53: 96744 (1999 OW3) C filter light curve, i – g, and z – i, with 11 Jan 2020 data shifted.

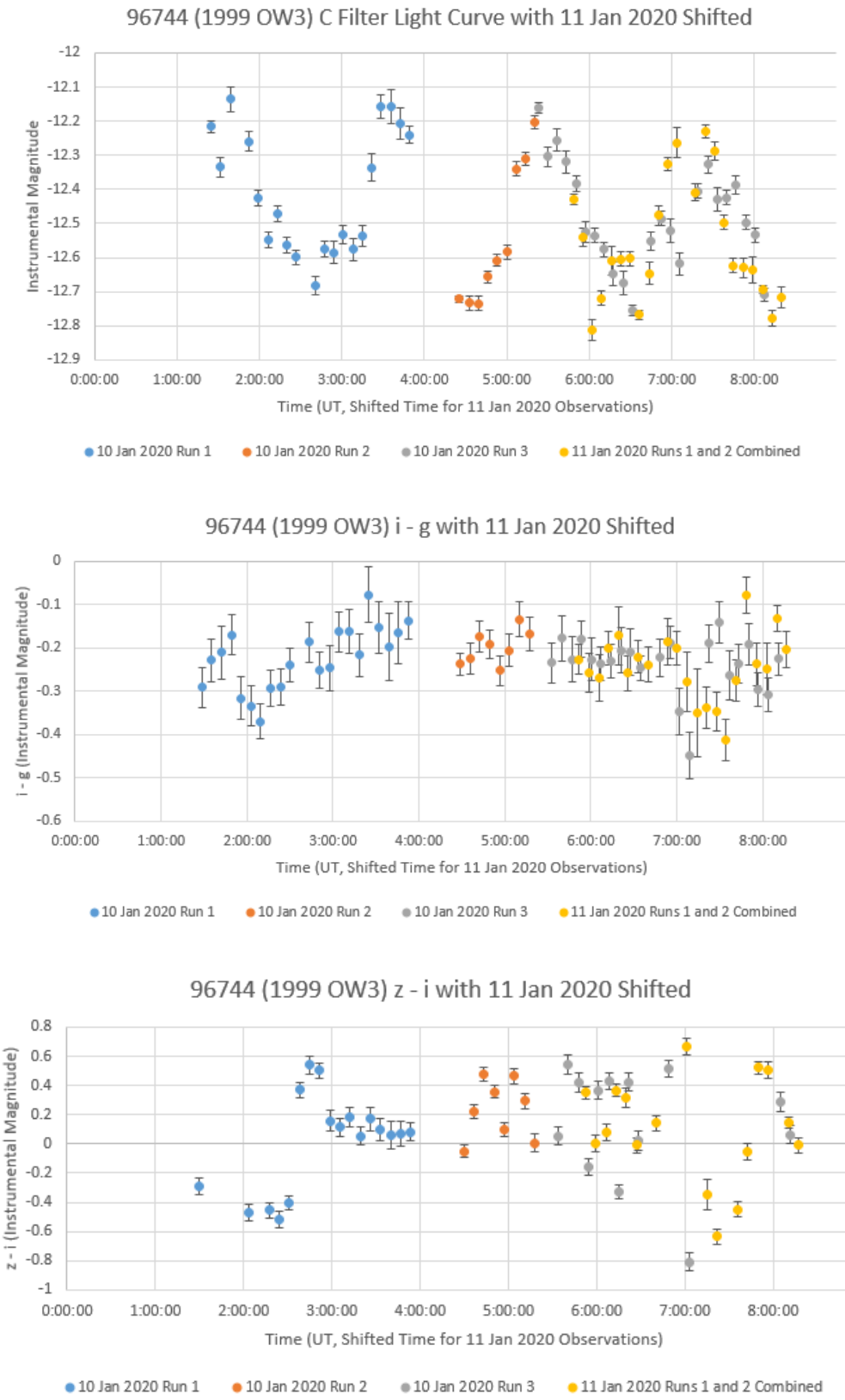

Figure 54: 96744 (1999 OW3) C filter light curve, i – g, and z – i, with 11 Jan 2020 data shifted.

From these graphs it is clear that a pattern is repeated: as 96744 (1999 OW3)'s instrumental magnitude decreases (96744 (1999 OW3) gets brighter), i – g becomes more negative than average and z – i flips from positive to negative. Then, the i – g and z – i values rapidly switch back to what they are for the majority of the rest of the light curves. It is worthy to note that this is not a perfect correlation; these i – g and z – i transitions appear to occur earlier with respect to 96744 (1999 OW3)'s C filter light curve on 11 Jan 2020 than on 10 Jan 2020. However, this pattern is still worthy to note.

So, what do these color changes *mean*? If C filter magnitude changes indicate rotation and i – g color changes indicate visible wavelength slope changes, then there is a correlation of visible wavelength slope and rotation phase. Similarly, if z – i color changes indicate 1 μm band depth changes, then there is a correlation of band depth changes and rotation phase. If 1 μm band depth changes indicate different compositions in part, then there is a correlation of compositional changes and rotation phase.

If the above two relationships are combined, the following statements can be made:

1. A steeper i – g slope correlates with a shallower 1 μm band depth,
2. A shallower i – g slope correlates with a deeper 1 μm band depth,
3. Both of these correlate roughly both with each other and also C filter magnitude variations, and
4. These correlations occur as C filter light curve for 96744 (1999 OW3) decreases in magnitude (gets brighter) at times.

It is worthwhile to note two things: 1) for the vast majority of the light curve 96744 (1999 OW3)'s i – g and z – i colors resemble statement 2 above (a shallower i – g slope and a deeper 1

μm band depth), and 2) the z filter magnitude variations from observation-to-observation are still greater than the g, r, and i filter variations. The reasons for this variability are unknown, but the reader should refer to the discussion of z filter magnitude variability of 2059 Baboquivari for possible reasons as well as potential reasons that have been ruled out.

However, for the sake of being thorough, z filter instrumental magnitudes of 96744 (1999 OW3) determined using the Kron algorithm were compared to z filter instrumental magnitudes determined using aperture photometry with a 2.5" aperture. The graph is shown below in Figure 55 for observation run 3 on 10 Jan 2020.

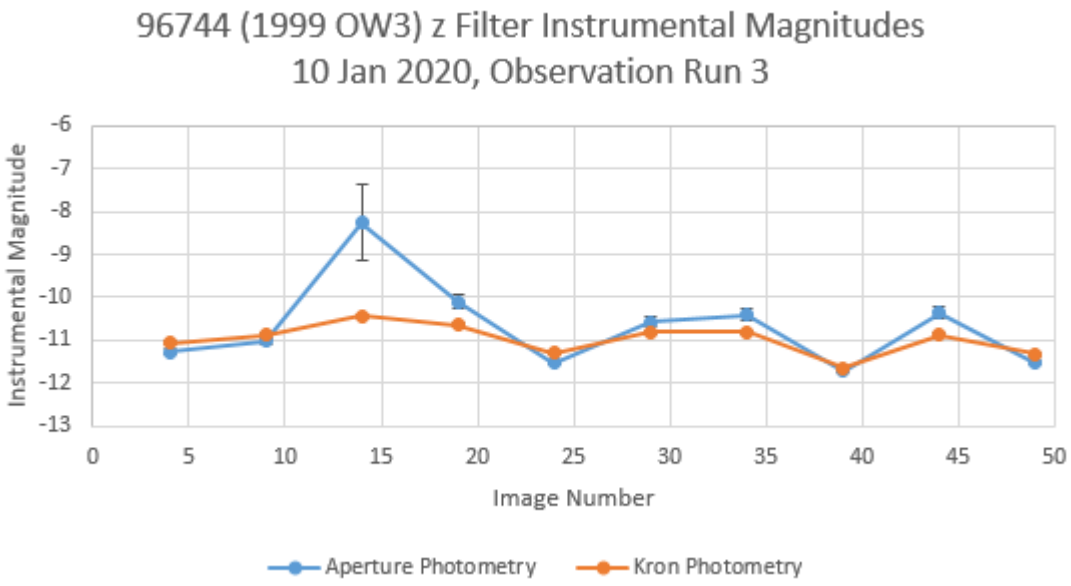

Figure 55: Aperture photometry vs Kron photometry z filter magnitudes for 96744 (1999 OW3) on 10 Jan 2020.

From this graph, it is apparent that although Kron-derived instrumental magnitudes display significant variability, the aperture photometry-derived instrumental magnitudes display even higher variability. This result is consistent with the same analysis performed on 2059

Baboquivari photometric data, and the same results can be concluded: that the Kron algorithm may *contribute* to photometric variability, but it is arguably more reliable than aperture photometry methods. With that said, even though z filter variability is greater than g, r, or i filters, the z – i colors fit a pattern that approximately repeats itself, so it is not suggested that 96744 (1999 OW3) exhibits a dust cloud or debris belt.

Similarly to 2059 Baboquivari, it is important to examine the sky conditions during with observations of 96744 (1999 OW3) were performed. Again, this is because 1) the z filter displays the greatest photometric variability, and 2) the z filter lies on the boundary between optical and infrared wavelengths. Patchy, light cirrus clouds can cause changes in sky conditions over short time intervals. The following figures show the instrumental magnitudes of several bright stars in the z filter as a function of image number (corresponding to time).

Figures 56a – e:

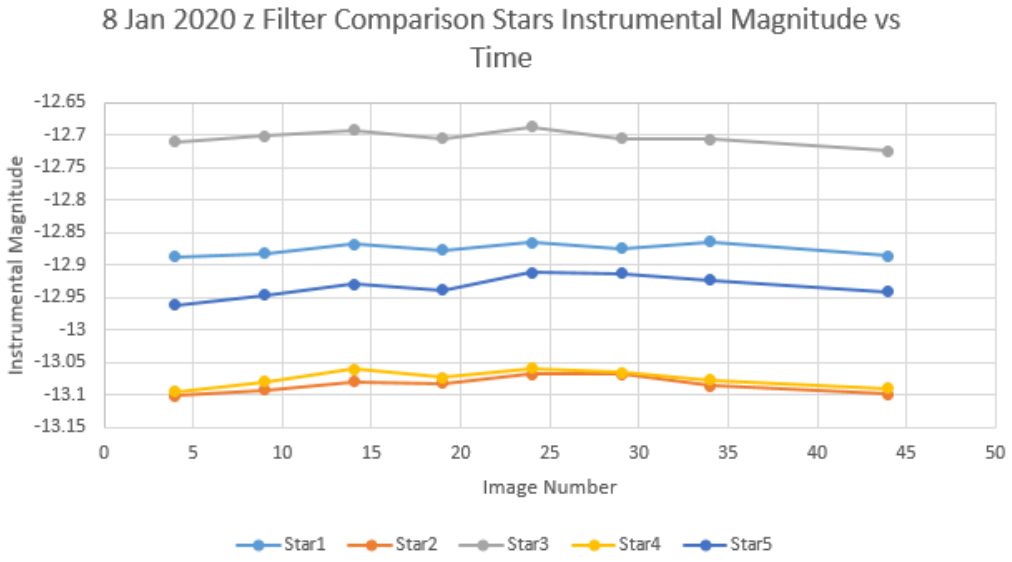

56a: Graph of instrumental magnitude vs. image number for bright stars in the z filter during observation run of 96744 (1999 OW3) on 8 Jan 2020.

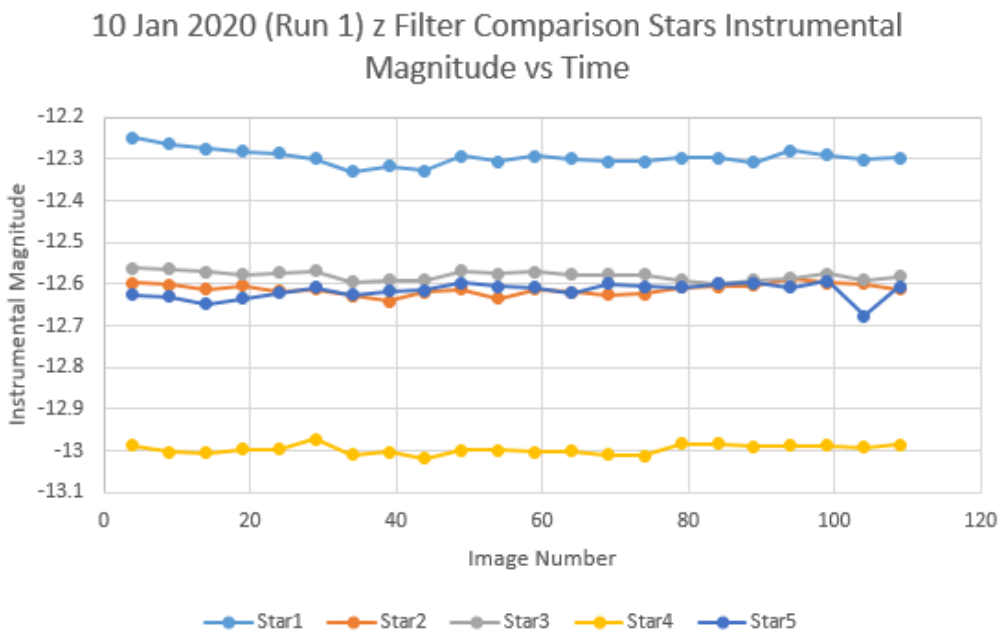

56b: Graph of instrumental magnitude vs. image number for bright stars in the z filter during observation run of 96744 (1999 OW3) on 10 Jan 2020.

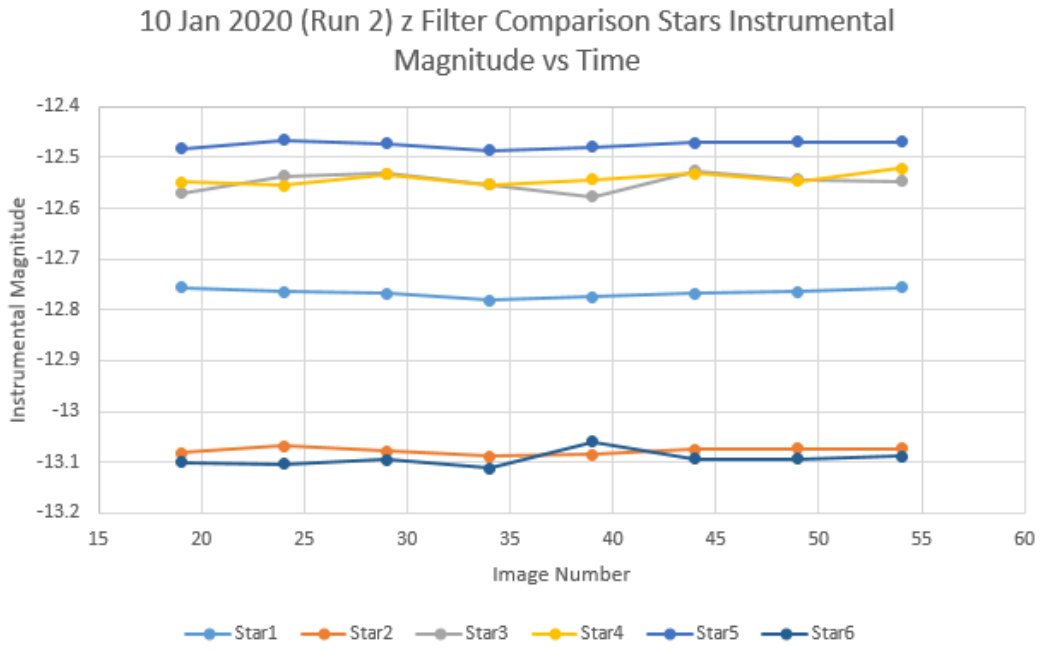

56c: Graph of instrumental magnitude vs. image number for bright stars in the z filter during observation run of 96744 (1999 OW3) on 10 Jan 2020.

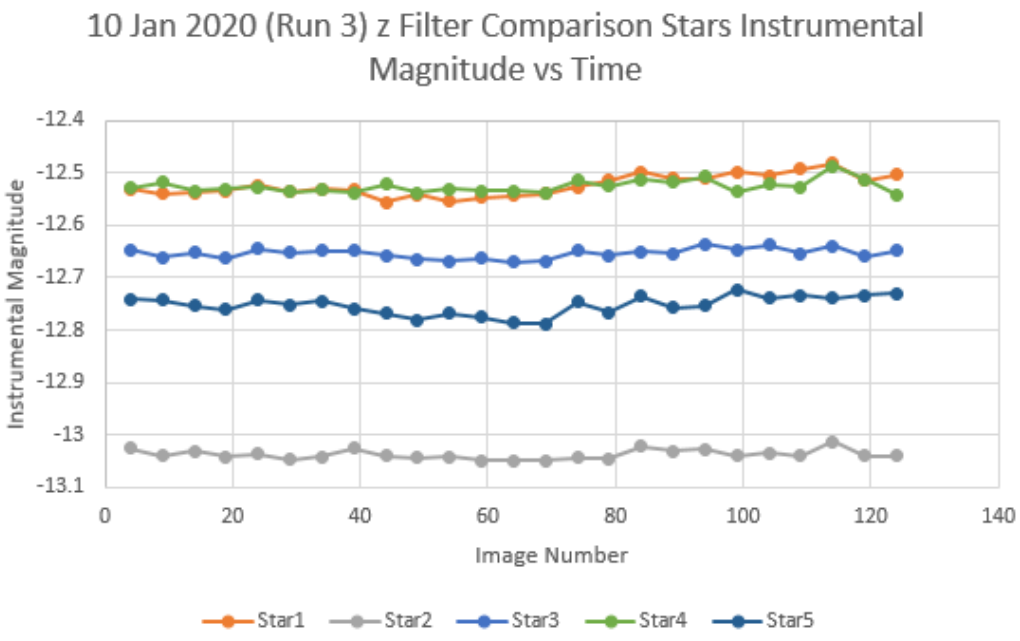

56d: Graph of instrumental magnitude vs. image number for bright stars in the z filter during observation run of 96744 (1999 OW3) on 10 Jan 2020.

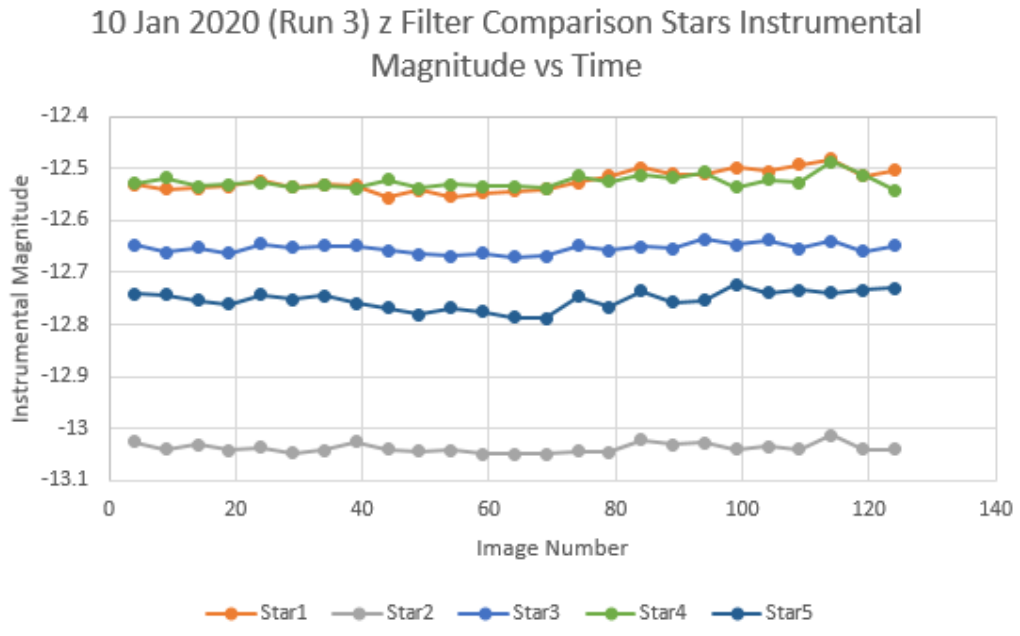

56e: Graph of instrumental magnitude vs. image number for bright stars in the z filter during observation run of 96744 (1999 OW3) on 11 Jan 2020.

It is clear from these figures that although there are some variations in instrumental magnitudes of these stars during observation runs of 96744 (1999 OW3), these variations are small (most fall within ~0.05 magnitudes) and when they are changing, they generally trend in the same direction. Thus, changes in sky conditions during these observations is not a major source of z filter variability for 96744 (1999 OW3).

No further statements can definitely be made about the colors or color relationships of 96744 (1999 OW3), as only instrumental magnitudes were used in the analysis. However, from both the photometric spectrum this thesis built of 96744 (1999 OW3) from MOC4 photometry (see Figure 33), and the V-type taxonomy assigned to 96744 (1999 OW3) by Carry et al. (2016), it is not unreasonable to suggest that for the vast majority of 96744 (1999 OW3)'s light curve its photometry does indeed resemble that of a V-type asteroid. For the minority of times when its colors resemble statement 1 (a steeper i – g slope correlating with a shallower 1 μm band depth) its taxonomy *may* appear to be more similar to that of an S- or Q-type asteroid.

96744 (1999 OW3) Phase Angle Relationships

Since the photometry obtained of 96744 (1999 OW3) could not be compared to its SDSS MOC4 observations, phase angle relationships between i – g slope and z – i band depth could not be compared. However, observations obtained in this research can be compared to one another. The i – g and z – i vs phase angle graphs are shown below in Figures 57a – b.

Figures 57a – b:

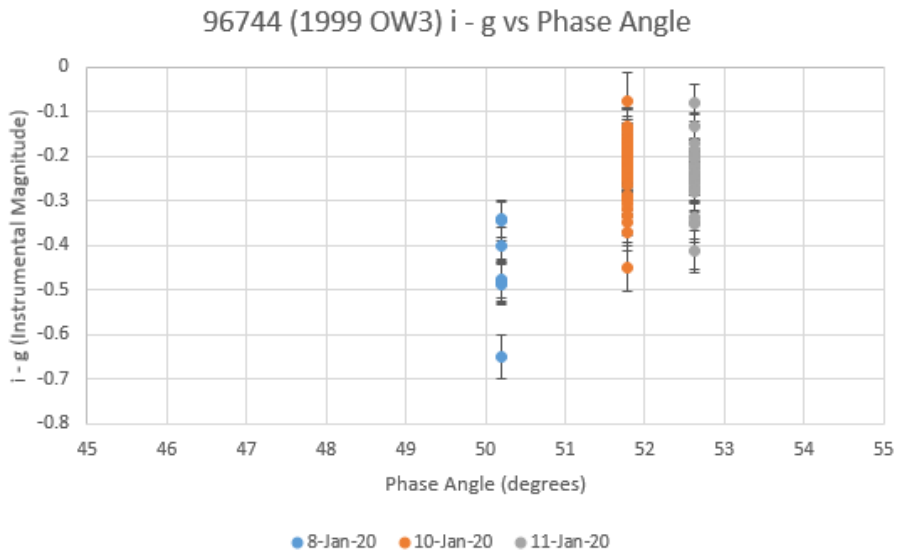

57a: i – g visible slope vs phase angle. The i – g values for 8 Jan 2020 are more negative than those for 10 and 11 Jan 2020. This implies a steeper visible spectral slope for 8 Jan 2020 observations than for 10 and 11 Jan 2020 observations.

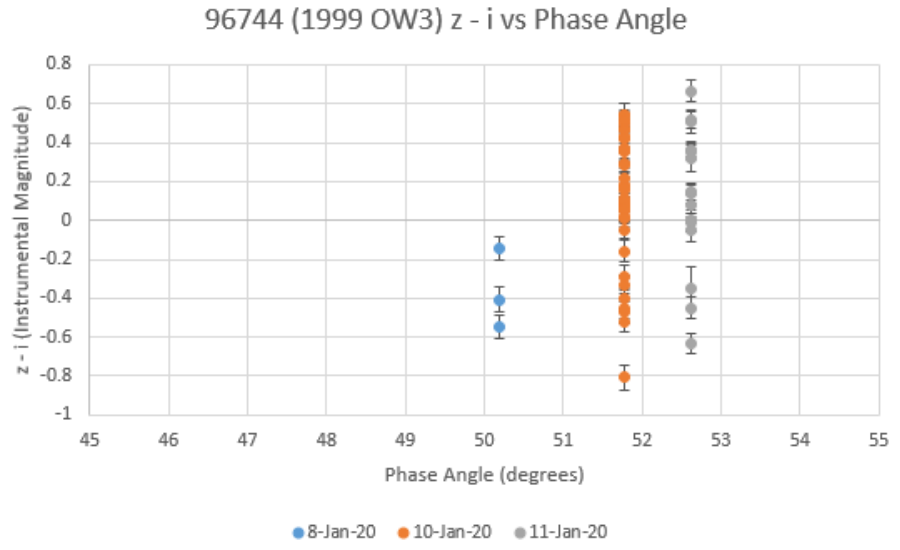

57b: z – i band depth vs phase angle. The z – i values for 8 Jan 2020 are more negative than those for 10 and 11 Jan 2020. This implies a shallower 1 μm band depth for 8 Jan 2020 observations compared to 10 and 11 Jan 2020 observations.

From these graphs, no clear trends can be recognized due to the small range of phase angles covered (only ~2.5 degrees). However, the i – g values for 8 Jan 2020 are more negative than those for 10 and 11 Jan 2020, which implies a steeper visible spectral slope for 8 Jan 2020 observations than for 10 and 11 Jan 2020 observations. Also, the z – i values for 8 Jan 2020 are more negative than those for 10 and 11 Jan 2020. This implies a shallower 1 μm band depth for 8 Jan 2020 observations compared to 10 and 11 Jan 2020 observations. However, this effect could be explained by a shorter observation run on 8 Jan 2020 which sampled less of the asteroid's surface compared to observation runs on 10 and 11 Jan 2020.

All in all, 96744 (1999 OW3) does display repeatable i – g and z – i variability with respect to rotation phase. The correlations are not perfect, but they do show rough agreement from light curve to light curve. These results *could* indicate compositional variability across the surface of 96744 (1999 OW3).

CHAPTER VII

CONCLUSIONS

2059 Baboquivari

From the analyses performed, spectrophotometric observations from SDSS have not been *consistently* repeated for 2059 Baboquivari as it clearly displays spectrophotometric variations. 2059 Baboquivari's spectrum only qualitatively resembles the S-/Q-type produced from SDSS observations in 7 of 12 photometric spectra. It appears to resemble more C-complex spectra in 2 of 12 photometric spectra, and surprisingly appears like a X-/P-/D-type asteroid in 3 of 12 photometric spectra.

The rapid z filter magnitude changes through ~25 minute observing runs, plus a drastic overall ~0.5 magnitude increase in brightness from 18 Nov to 21 Nov needed to be explained. Of the causes considered, the following are the most likely for variability:

1. Dust/debris cloud/ring. This is the most likely cause, with the rotational instability hypothesis being the most appealing.
2. Issues with the Kron algorithm, which is much less likely.

2059 Baboquivari's root mean square z filter and z – i reflectance values did not show a statistically significant difference compared to those values from its SDSS observation. However, individual measurements of z filter and z – i reflectance values compared to those values from its SDSS observation varied up to the 3.8σ level, demonstrating a large dispersion in these z filter and z – i reflectance values.

Rotational heterogeneities and a binary system have effectively been ruled out due to the small ~0.05 maximum magnitude changes in brightness through the relatively short ~25 minute

observing runs, and the unlikelihood of observing a moon with the right orbital plane. A filter wheel error has also been ruled out through an analysis of raw counts from 2059 Baboquivari.

Phase angle relationships were also explored for 2059 Baboquivari. SDSS observations were made at a phase angle of 22.1 degrees, while this study's observations were made at ~45 – 50 degrees. Data are somewhat sparse, and although there is no significant dependence of i – g slope vs phase angle, there may be a slight i – g slope anti-correlation with phase angle. There is no significant difference in i – g slope vs phase angle depending on if 2059 Baboquivari's spectrum appears S-/Q-type or C-/X-/P-/D-type. These phase angle relationships are somewhat unusual for an asteroid, as only a minority of asteroids have anti-correlations of i – g slope vs phase angle. However, given available statistics 2059 Baboquivari's slope vs phase angle relationship is not entirely surprising, as Carvano & Davalos (2015) found that 24.4% and 20.2% of asteroids in the SDSS MOC4 showed no correlation and an anti-correlation of i – g slope vs phase angle, respectively. Also, z – i band depth vs phase angle shows a slight anti-correlation; as phase angle increases, z – i band depth slightly decreases. 2059 Baboquivari's z – i relationship with phase angle is also somewhat unusual but not entirely surprising either, as Carvano & Davalos (2015) found that 26.6% and 32.2% of asteroids in the SDSS MOC4 showed no correlation and an anti-correlation of z – i band depth vs phase angle, respectively. Possible reasons for this relationship are: less-opaque surface particles, surface particles that exhibit more back-scattering than forward-scattering properties, a lack of macroscopic surface roughness, and/or a less-ellipsoidal shape for 2059 Baboquivari.

96744 (1999 OW3)

Since 96744 (1999 OW3) was observed at ~-65 degrees declination and no large scale stellar survey has reached that far south, calibrated magnitudes for the 96744 (1999 OW3) could not be calculated. Thus, only instrumental magnitudes were used for data analysis. As a result, it is not clear whether photometry from the SDSS MOC4 was replicated in this study. But, by studying i – g and z – i instrumental magnitudes it is apparent that for the majority of the photometry 96744 (1999 OW3) has a moderately positive visible spectral slope and a clear 1 μm absorption band which varies in depth.

C filter light curves were constructed from observation runs on 8 Jan, 10 Jan, and 11 Jan 2020. By calculating the difference in time from max-to-max and min-to-min features in the light curve, a rotation period of ~2 hours or a multiple of ~2 hours was determined. For the majority of observations, z filter instrumental magnitudes were dimmer than i filter instrumental magnitudes, suggesting a strong 1 μm absorption feature. These instances correlated with a moderately positive i – g spectral slope. A minority of observations indicated a shallower 1 μm band depth which correlated with a steeper i – g spectral slope. The steeper spectral slope and shallower 1 μm band depth correlated with a decrease in instrumental magnitude in 96744 (1999 OW3)'s C filter light curve, that is, as 96744 (1999 OW3) brightened. Thus, it was found that changes in i – g slope *correlate* with changes in z – i band depth, which both correlate with the same C filter instrumental magnitude changes. As a result, 96744 (1999 OW3) *may* vary in composition across its surface.

Variability in z filter magnitudes were higher than g, r, and i filter magnitude variability, but by comparing 2.5" aperture photometry values with Kron algorithm-derived magnitudes, it was determined that the Kron algorithm produced more reliable results. This is the same conclusion arrived at concerning 2059 Baboquivari's z filter magnitude variability.

No conclusive spectral slope or band depth vs phase angle relationships could be determined for 96744 (1999 OW3). There were no clear relationships between spectral slope, band depth, and phase angle due to the small ~2.5 degree phase angle range sampled. However, i – g values display a steeper visible spectral slope for 8 Jan 2020 observations than for 10 and 11 Jan 2020 observations, and z – i values display a shallower 1 μm band depth for 8 Jan 2020 observations compared to 10 and 11 Jan 2020 observations.

Future Work

Although this study has shed light upon two sparsely-explored near-Earth asteroids, more study is required to further characterize these objects. 2059 Baboquivari's mysterious spectral variability and especially-variable z filter reflectance remains poorly explained, and future observations should aim to obtain photometric observations over the course of several hours to several days. A complete light curve and rotational period will allow the correlation of this variability with rotation phase. In addition, rapid z – i and/or z – r photometry will allow more focused explorations of 2059 Baboquivari's z filter variability. Obtaining vis/NIR spectra will give more detail of 2059 Baboquivari's spectral features and should be obtained as well. Due to 2059 Baboquivari's eccentric orbit that takes it out to ~4 AU at aphelion, it will not be observable again until mid-2023 at the earliest. In October 2032 it passes relatively close to Earth (0.35 AU) so extensive observations should be obtained then.

Asteroid 96744 (1999 OW3) also requires further study. More photometry should be obtained in order to refine 96744 (1999 OW3)'s light curve and to constrain a rotational period. Repeated observations in g, r, i, and z filters will aid in constraining or discounting the observed repeating color variations with respect to rotation. In addition, vis/NIR spectral observations would give higher resolution of any spectral features. 96744 (1999 OW3) has an inclined orbit,

so future opportunities for observation will also be at a highly negative declination. But opportunities for future observation recur more often as 96744 (1999 OW3) fortunately has an orbital period of ~3 years: in late 2022 – early 2023 and late 2025 – early 2026, and late 2028 – early 2029.

All in all, the advances and gaps in knowledge of these near-Earth asteroids highlight the need to further study our smallest cosmic neighbors.

Bibliography

Alvarez-Candal, A. (2013). SDSS Photometry of asteroids in cometary orbits. *Astronomy and Astrophysics, 549*/34A, 5 pp.

Appenzeller, I. (2013). *Introduction to Astronomical Spectroscopy*. Cambridge: Cambridge University Press.

Beatty, J.K., Petersen, C.C., & Chaikin, A. (1999). *The New Solar System*. Cambridge: Sky Publishing Corporation.

Beekman, G. (2005). The nearly forgotten scientist Ivan Osipovich Yarkovsky. *Journal of the British Astronomical Association*, *115*(4), p. 207.

Bell, J.F., Owensby, P.D., Hawke, B.R., & Gaffey, M.J. (1988). The 52-color asteroid survey: Final results and interpretation. *Lunar Planet. Sci XIX*, pp. 57-58.

Bendjoya, Ph., & Zappalà, V., (2002). Asteroid Family Identification. In *Asteroids III* (W.F. Bottke et al., eds.), pp. 613-618. Univ. of Arizona, Tucson.

Benner, L.A., Busch, M.W., Giorgini, J.D., Taylor, P.A., & Margot, J.-L. (2015). Radar observations of near-Earth and main-belt asteroids. In *Asteroids IV* (P. Michel et al., eds.), pp. 165-182. Univ. of Arizona, Tucson.

Binzel, R.P., Harris, A.W., Bus, S.J., & Burbine, T.H. (2001). Spectral Properties of Near-Earth Objects: Palomar and IRTF Results for 48 Objects Including Spacecraft Targets (9969) Braille and (10303) 1989 ML. *Icarus, 151*, pp. 139-149.

Binzel, R.P., Rivkin, A.S., Stuart, J.S., Harris, A.W., Bus, S.J., & Burbine, T.H. (2004). Observed spectral properties of near-Earth objects: results for population distribution, source regions, and space weathering processes. *Icarus, 170*(2), pp. 259-294.

Bottke, W.F., Jedicke, R., Morbidelli, A., Petit, J.-M., & Gladman, B. (2000a). Understanding the distribution of near-Earth asteroids. *Science*, *288*, pp. 2190–2194.

Bottke, W.F., Morbidelli, A., Jedicke, R., Petit, J.-M., Levison, H.F., Michel, P., & Metcalfe, T.S. (2002). Debiased Orbital and Absolute Magnitude Distribution of the Near-Earth Objects. *Icarus, 156*(2), pp. 399-433.

Bottke, W.F., Vokrouhlicky, D., Rubincam, D.P., & Nesvorny, D. (2006). The Yarkovsky and YORP Effects: Implications for Asteroid Dynamics. *Annual Review of Earth and Planetary Sciences*, *34*, pp. 157-191.

Bottke, W.F., Brovž, M., O' Brien, D.P., Campo Bagatin, A., Morbidelli, A., & Marchi, S. (2015). The collisional evolution of the main asteroid belt. In *Asteroids IV* (P. Michel et al., eds.), pp. 701-724. Univ. of Arizona, Tucson.

Brown, M.E., Trujillo, C.A., & Rabinowitz, D.L. (2005). Discovery of a Planetary-sized Object in the Scattered Kuiper Belt. *The Astrophysical Journal, 635*(1), pp. 97-100.

Burbine, T.H & Binzel, R.P. (2002). Small Main Belt Spectroscopic Survey in the Near-Infrared. *Icarus, 159*, pp. 468-499.

Bus S.J. & Binzel, R.P. (2002A). Phase II of the small main-belt asteroid spectroscopic survey: The observations. *Icarus, 158*, pp. 106-145.

Bus S. J. & Binzel, R.P. (2002B). Phase II of the small main-belt asteroid spectroscopic survey: A feature based taxonomy. *Icarus, 158*, pp. 146-177.

Carry, B., Solano, E., Eggl, S., & DeMeo, F.E. (2016). Spectral properties of near-Earth and Mars-crossing asteroids using Sloan photometry. *Icarus*, *268*, pp. 340-354.

Carvano, J.M., Hasselmann, P.H., Lazzaro, D., & Mothé-Diniz, T. (2010). SDSS-based taxonomic classification and orbital distribution of main belt asteroids. *Astronomy and Astrophysics*, *510*/A43.

Carvano, J.M., & Davalos, J.A.G. (2015). Shape and solar phase angle effects on the taxonomic classifications of asteroids. *Astronomy and Astrophysics*, *580*/A98.

Discovery Statistics: WISE/NEOWISE. (2020). Discovery Statics: WISE/NEOWISE. URL https://cneos.jpl.nasa.gov/stats/wise.html

Chapman, C.R., McCord, T.B., & Johnson, T.V. (1973). Asteroid Spectral Reflectivities. *The Astronomical Journal, 78*, pp. 126-40.

Chapman, C.R., Morrison, D., & Zellner, B. (1975). Surface properties of asteroids: A synthesis of polarimetry, radiometry, and spectrophotometry. *Icarus*, *25*, pp. 104-130.

Chapman, C.R. & Gaffey, M.J. (1979). Reflectance spectra for 277 asteroids. In *Asteroids* (T. Gehrels and M.S. Matthews, eds.), pp. 655-687. University of Arizona Press, Tucson.

Dandy, C.L., Fitzsimmons, A., Collander-Brown, S.J. (2003). Optical colors of 56 near-Earth objects: trends with size and orbit. *Icarus, 163*(2), pp. 363-373.

DeMeo, F.E., & Binzel, R.P. (2008). Comets in the near-Earth object population. *Icarus, 194*(2), pp. 436-449.

DeMeo, F.E., Binzel, R.P., Slivan, S. M., & Bus, S. J. (2009). An extension of the Bus asteroid taxonomy into the near-infrared. *Icarus, 202*, pp. 160-180.

DeMeo, F.E., & Carry, B. (2013). The taxonomic distribution of asteroids from multi-filter all-sky photometric surveys. *Icarus*, *226*(1), pp. 723-741.

DeMeo, F.E., & Carry, B. (2014). Solar System evolution from compositional mapping of the asteroid belt. *Nature*, *505*, pp. 629-634.

Edgeworth, K.E. (1949). The origin and evolution of the Solar System. *Monthly Notices of the Royal Astronomical Society, 109*, pp. 600-609.

Encyclopedia Brittanica. (2020). Asteroid distribution between Mars and Jupiter. Encyclopedia Brittanica. URL www.brittannica.com/science/asteroid.

Farinella, P., Froeschle, C., Froeschle, C., Gonczi, R., Hahn, G., Morbidelli, A., & Valsecchi, G. B. (1994). Asteroids falling onto the sun. *Nature, 371*, pp. 315-317.

Farinella, P., Vokrouhlicky, D., & Hartmann, W.K. (1998). Meteorite Delivery via Yarkovsky Orbital Drift. *Icarus*, *132*, pp. 378-387.

Fernandez, J.A., & Ip, W.-H. (1991). Statistical and evolutionary aspects of cometary orbits. *Comets in the post-Halley era, 1,* pp. 487-535.

Gaffey M.J., Reed, K.L., & Kelley, M.S. (1992). Relationship of E-type Apollo Asteroid 3103 (1982 BB) to the Enstitate Achondrite Meteorites and the Hungaria Asteroids. *Icarus, 100*, pp. 95-109.

Gaffey M.J., Bell, J.F., Brown, R.H., Burbine, T.H., Piatek, J.L., Reed, K.L.,& Chaky, D.A. (1993) Mineralogical Variations within the S-Type Asteroid Class. *Icarus, 106*, pp. 573-602.

Gaffey, M.J. (2010). Space weathering and the interpretation of asteroid reflectance spectra. *Icarus*, *209*, pp. 564-574.

Gaffey, M.J., Reddy, V., Fieber-Beyer, S., & Cloutis, E. (2015). Asteroid (354) Eleonora: Plucking an odd duck. *Icarus, 250*, pp. 623-638.

Gehrels, T. (1970). Photometry of asteroids. In *Surfaces and Interiors of Planets and Satellites* (A. Dollfus, ed.), pp. 317-375. Academic Press, Orlando, Fla./London.

Gehrels, T., Roemer, E., Taylor, R.C., & Zellner, B.H. (1970). Minor planets and related objects. IV. Asteroid (1566) Icarus. *The Astronomical Journal*, *75*, pp. 186-195.

Gehrels, T., & Tedesco, E.F. (1979). Minor planets and related objects. IV. XXVIII. Asteroid magnitude and phase relations. *The Astronomical Journal*, *84*, pp. 1079-1087.

Gladman, B.J., Migliorini, F., Morbidelli, A., Zappala, V., Michel, P., Cellino, A., Froeschle, C., Levison, H.F., Bailey, M., & Duncan, M. (1997). Dynamical lifetimes of objects injected into asteroid belt resonances. *Science, 277*, pp. 197-201.

Gomes, R., Levison, H.F., Tsiganis, K., & Morbidelli, A. (2005). Origin of the cataclysmic Late Heavy Bombardment period of the terrestrial planets. *Reviews of Modern Physics, Institute for Advanced Study, Princeton, New Jersey, 51*(3), pp. 447-460.

Gunn, J.E., et al. (2006). The 2.5 m Telescope of the Sloan Digital Sky Survey. *The Astronomical Journal*, *131*(4), pp. 2332-2359.

Gunn, J.E., et al. (1998). The Sloan Digital Sky Survey Photometric Camera. *The Astronomical Journal, 116*, pp. 3040-3081.

Gradie, J., & Veverka, J. (1986). The wavelength dependence of phase coefficients. *Icarus*, *66*, pp. 455-467.

Greenstreet, S., Ngo, H., & Gladman, B. (2012). The orbital distribution of Near-Earth Objects inside Earth's orbit. *Icarus, 217*(1), pp. 355-366.

Hirayama, K. (1918). Groups of asteroids probably of common origin. *Proceedings of the Tokyo Mathematico-Physical Society*. 2nd Series, Vol 9 (1917-1918) No. 17, pp. 354-361.

Hsieh, H.H., & Jewitt, D.C. (2006). A Population of Comets in the Main Asteroid Belt. *Science, 312*(5773), pp. 561-563.

IAU-A Minor Planet Center. (2018). Distribution of Minor Planets Semimajor axis. IAU Minor Planet Center. URL http://www.minorplanetcenter.net/iau/plot/OrbEls01.gif

IAU-B Minor Planet Center. (2018). Distribution of Minor PlanetsL Eccentricity. IAU Minor Planet Center. URL http://www.minorplanetcenter.net/iau/plot/OrbEls02.gif

IAU-C Minor Planet Center, (2018). Distribution of Minor Planets: Inclination. IAU Minor Planet Center. URL http://www.minorplanetcenter.net/iau/plot/OrbEls03.gif

IAU-D Minor Planet Center. (2018). Distribution of Minor Planets: Absolute Magnitude. IAU Minor Planet Center. URL http://www.minorplanetcenter.net/iau/plot/OrbEls10.gif

IAU-E Minor Planet Center. (2018). Distribution of Minor Planets: a vs e. IAU Minor Planet Center. URL http://www.minorplanetcenter.net/iau/plot/OrbEls50.gif

IAU-F Minor Planet Center. (2018). Distribution of Minor Planets: a vs i. IAU Minor Planet Center. URL http://www.minorplanetcenter.net/iau/plot/OrbEls51.gif

IAU-G Minor Planet Center. (2018). Distribution of Minor Planets: e vs i. IAU Minor Planet Center. URL http://www.minorplanetcenter.net/iau/plot/OrbEls52.gif

IAU-H Minor Planet Center. (2018). Distribution of Minor Planets: H vs a. IAU Minor Planet Center. URL http://www.minorplanetcenter.net/iau/plot/OrbEls53.gif

IAU-I Minor Planet Center. (2018). Distribution of Minor Planets: H vs number. IAU Minor Planet Center. URL https://minorplanetcenter.net/iau/plot/OrbEls14.gif

Ivezić, Ž., Tabachnik, S., Rafikov, R., et al. (2001). Solar System Objects Observed in the Sloan Digital Sky Survey Commissioning Data. *The Astronomical Journal, 122*(5), pp. 2749-2784.

Ivezić, Ž., Jurić, M., Lupton, R., et al. (2010). Sloan Digital Sky Survey (SDSS) Moving Object Catalog 4th Release, EAR-A-I0035-3-SDSSMOC-V3.0.

J.C. (1867). Hermann Goldschmidt. *Monthly Notices of the Royal Astronomical Society*, *27*(4), pp. 15-17.

Jewitt, D.C. & Luu, J. (1993). Discovery of the candidate Kuiper Belt Object 1992QB1. *Nature, 362*(6422), pp. 730-732.

Jewitt, D.C. (2002). From Kuiper Belt Object to Cometary Nucleus: The Missing Ultrared Matter. *The Astronomical Journal, 123*(2), pp. 1039- 1049.

Jewitt, D.C. (2012). The Active Asteroids. *The Astronomical Journal, 143*(3), 14 pp.

Jewitt, D.C. (2013). Properties of Near-Sun Asteroids. *The Astronomical Journal, 145*(5), pp. 133-138.

Keil, K. (2000). Thermal alteration of asteroids: evidence from meteorites. *Planetary Space Science*, *48*, pp. 887-903.

Kozai, Y. (1962). Secular Perturbations of Asteroids with High Inclination and Eccentricity. *The Astronomical Journal, 67*(9), pp. 591-598.

Kron, R.G. (1980). Photometry of a Complete Sample of Faint Galaxies. *The Astrophysical Journal, Supplement Series, 43,* pp. 305-325.

Kuiper, G.P. (1951). On the Origin of the Solar System. *Proceedings of the National Academy of Sciences of the United States of America, 37*(1), pp. 1-14.

Lantz, C., Binzel, R.P., & DeMeo, F.E. (2018). Space weathering trends on carbonaceous asteroids: A possible explanation for Bennu's blue slope? *Icarus, 302*, pp. 10-17.

Lauretta, D.S., et al. (2019). Episodes of particle ejection from the surface of active asteroid (101955) Bennu. *Science*, *366*(6470), 12 pp.

Lazzaro D., Angeli, C.A., Carvano, J.M., Mothe-Diniz, T., Duffard, R., & Florczack, M. (2004). S3OS2: the visible spectroscopic survey of 820 asteroids. *Icarus, 172*, pp. 179-220.

Levison, H.F., & Duncan, M.J. (1994). The long-term dynamical behavior of short-period comets. *Icarus, 108*(1), pp. 18-36.

Li, J., & Jewitt, D.C. (2013). Recurrent Perihelion Activity in (3200) Phaethon. *The Astronomical Journal, 145*(6), pp. 1-9.

Linder, T. (2017). *Rotational Study Of Ambiguous Taxonomic Type Asteroids*. Masters thesis, University of North Dakota.

Luu, J.X., & Jewitt, D.C. (1990). Charge-coupled device spectra of asteroids: 1 – Near-Earth and 3:1 resonance asteroids. *The Astronomical Journal*, *99*, pp. 1985-2011.

Mainzer, A., Grav, T., Masiero, J., Bauer, J., Wright, E., Cutri, R.M., McMillan, R.S., Cohen, M., Ressler, M., & Eisenhard, P. (2011). Thermal model calibration for minor planets observed with Wide-field Infrared Survey Explorer/NEOWISE. *The Astrophysical Journal*, *736*(2), 100.

Margot, J.L., Nolan, M.C., Benner, L.A M., Ostro, S.J., Jurgens, R.F., Giorgini, J.D., Slade, M.A., & Campbell, D.B. (2002). Binary Asteroids in the Near-Earth Object Population. *Science, 296*(5572), pp. 1445-1448.

Margot, J.-L., Pravec, P., Taylor, P., Carry, B., & Jacobson, S. (2015). Asteroid Systems: Binaries, Triples, and pairs. In *Asteroids IV* (P. Michel et al., eds.), pp. 355-374. Univ. Of Arizona, Tucson.

Masiero, J. R., Grav, T., Mainzer, A. K., Nugent, C. R., Bauer, J. M., Stevenson, R., Sonnett, S. (2014). Main-Belt Asteroids with WISE/NEOWISE: Near-Infrared Albedos. *The Astrophysical. Journal*, *791*(2), 121.

McCord T.B., & Chapman, C.R. (1975). Asteroids: Spectral Reflectance and Color Characteristics. *The Astrophysical Journal, 195*, pp. 553-562.

McCord T.B., & Chapman, C.R. (1975). (1975). Asteroids: Spectral Reflectance and Color Characteristics. II. *The Astrophysical Journal, 197*, pp. 781-790.

McLean, I.S. (2008). *Electronic Imaging in Astronomy: Detectors and Instrumentation*. Germany: Praxis Publishing, Ltd., Chichester, U. K.

McSween, H. (1999) *Meteorites and their Parent Planets, 2nd Ed*. New York, NY: Cambridge University Press.

Montmerle, T., Augereau, J.C., Chaussidon, M., Marty, B., & Morbidelli, A. (2006). Solar System Formation and Evolution: the First 100 Million Years. *Earth, Moon, and Planets*, *98*, pp. 39-95.

Moore, P., & Rees, R. (2011). *Patrick Moore's Data Book of Astronomy (2nd ed.)*. Cambridge: Cambridge University Press.

Morbidelli, A., Gonczi, R., Froeschlè, Ch., & Farinella, P. (1993). Delivery of meteorites

through the υ_6 secular resonance. *Astronomy and Astrophysics*, *292*, pp. 955-979.

Morbidelli, A., Levison, H.F., Tsiganis, K., & Gomes, R. (2005). Chaotic capture of Jupiter's Trojan asteroids in the early Solar System. *Nature*, *435*(7041), pp. 462-465.

Mothé-Diniz, T., Roig, F., & Carvano, J.M., (2005). Reanalysis of asteroid families structure through visible spectroscopy. *Icarus*, *174*, pp. 54-80.

Nesvorný, D., Brož, M., & Curruba, V. (2015). Identification and dynamical properties of asteroid families. In *Asteroids IV* (P. Michel et al., eds.), pp. 297-321. Univ. of Arizona, Tucson.

Neugebauer, G., et al. (1984). The Infrared Astronomical Satellite (IRAS) Mission. *The Astrophysical Journal*, *278*, pp. L1-L6.

North, J. (2008). *Cosmos: An Illustrated History of Astronomy and Cosmology*. Chicago: The University of Chicago Press.

Oort, J. (1950). The structure of the cloud of comets surrounding the Solar System and a hypothesis concerning its origin. *Bulletin of the Astronomical Institutes of the Netherlands, 11*, pp. 91-110.

Pater, I.D., & Lissauser, J.J. (2010). *Planetary Sciences.* United Kingdom: University Press, Cambridge.

Pravec, P., & Harris, A.W. (2000). Fast and Slow Rotation of Asteroids. *Icarus*, *148*(1), pp. 12-20.

Quantum Design Europe. (2020). Astronomy/UBVRI Filters from Andover. URL https://qd-europe.com/at/en/product/astronomyuvbri-filters/.

Reddy, V., & Sanchez, J.A. (2016). Reddy Main Belt Asteroid Spectra V1.0. *NASA Planetary Data System.* EAR-A-I0046-3-REDDYMBSPEC-V1.0.

Richardson, D.C., Bottke, W.F., & Love, S.G. (1998). Tidal Distortion and Disruption of Earth-Crossing Asteroids. *Icarus*, *134*(1), pp. 47-76.

Rubincam, D.P. (2000). Radiative Spin-up and Spin-down of Small Asteroids. *Icarus*, *148*(1), pp. 2-11.

Rubincam, D.P., & Paddock, S.J. (2007). As Tiny Worlds Turn. *Science*, *316*(5822), pp. 211-212.

Sagan, C., & Druyen, A. (1997) *Comet*. London: Headline Book Publishing.

Sanchez, J.A. (2012). *Temperature-induced effects and phase reddening on near-Earth asteroids*. Doctoral thesis, Westfälische Wilhelms-Universität Münster.

Sanchez, J.A., Reddy, V., Nathues, A., Cloutis, E.A., Mann, P., & Hiesinger, H. (2012). Phase reddening on near-Earth asteroids: Implications for mineralogical analysis, space weathering and taxonomic classification. *Icarus*, *220*, pp. 36-50.

Serio, G.F., Manara, A., & Sicoli, P. (2002). Giuseppe Piazzi and the Discovery of Ceres. In *Asteroids III* (W.F. Bottke Jr. et al., eds.), pp. 17-24. Univ of Arizona, Tucson.

Shoemaker, E.M. (1983). Asteroid and comet bombardment of the earth. *Annual review of earth and planetary sciences, 11*, pp. 461-494.

Sloan Digital Sky Survey. (2006). SDSS Data Release 5: Imaging Camera Parameters and Description. URL http://classic.sdss.org/dr5/instruments/imager/index.html.

Sloan Digital Sky Survey. (2020). Estimates for the u, g, r, i, z Colors of Vega and the Sun. Sloan Digital Sky Survey. URL https://www.sdss.org/dr12/algorithms/ugrizvegasun/.

Szabó, Gy. M., Ivezić, Ž., Jurić, M., Lupton, R., & Kiss, L.L. (2004). Colour variability of asteroids in the Sloan Digital Sky Survey Moving Object Catalog. *Monthly Notices of the Royal Astronomical Society, 348*(3), pp. 987-998.

Tedesco, E.F., Tholen, D.J., & Zellner, B. (1982). The Eight Color Asteroid Survey: Standard Stars. *The Astronomical Journal*, *87*(11), pp. 1585-1592.

Tholen, D.J. (1984). *Asteroid Taxonomy from Cluster Analysis of Photometry.* Doctoral thesis, University of Arizona.

Tholen, D.J. (1989). Asteroid taxonomic classifications. *Asteroids II*. Tucson: University of Arizona Press, pp. 1139-1150.

Tsiganis, K., Gomes, R., Morbidelli, A., & Levison, H.F. (2005). Origin of the orbital architecture of the giant planets of the Solar System. *Nature Letters*, *435*, pp. 459-469.

Vernazza, P., & Beck, P. (2017). Composition of Solar System Small Bodies. In *Planetesimals: Early Differentiation and Consequences for Planets* (Elkins-Tanton, L.T., & Weiss, B.P. eds.), pp. 269-297. Cambridge University Press, Cambridge.

Walsh, K.J., Morbidelli, A., Raymond, S.N., O'Brien, D.P., & Mandell, A.M. (2011). A low mass for Mars from Jupiter's early gas-driven migration. *Nature, 475*(7355), pp. 206-209.

Warner, B. D., Harris, A. W., Pravec, P., (2009). The asteroid lightcurve database. *Icarus*, *202*, pp. 134-146.

Waszczak, A., Chang, C-K., Ofek, E. O., Laher, R., Masci, F., Levitan, D., Surace, J., Cheng, Y-C., Ip, W-H., Kinoshita, D., Helou, G., Prince, T. A., & Kulkarni, S. (2015). Asteroid Lightcurves from the Palomar Transient Factory Survey: Rotation Periods and Phase Functions from Sparse Photometry. *The Astronomical Journal, 150*(3), 75.

Wetherill, G.W. (1976). Where do meteorites come from – A re-evaluation of the earth-crossing Apollo objects as sources of chondritic meteorites. *Geochimica et Cosmochimica Acta, 40*, pp. 1297-1317.

Wetherill, G.W. (1979). Steady-state populations of Apollo-Amor objects. *Icarus, 37*, pp. 96-112.

Wetherill, G.W. (1985). Meteorites may follow a chaotic route to earth. *Nature, 315*, pp. 731-733.

Whipple, F. (1983). 1983TB and the Geminid Meteors. *International Astronomical Union Circular*, No. 3881, #1.

Woolfson, M.M. (1993). The Solar System - its Origin and Evolution. *Quarterly Journal of the Royal Astronomical Society*, *34*, pp. 1-20.

Xu, S., Binzel, R.P., Burbine, T.H., & Bus, S.J. (1995). Small Main Belt Asteroid Spectroscopic Survey: Initial Results. *Icarus, 115*(1), pp. 1-35.

Zappalà, V., Cellino, A., Farinella, P., & Knežević, Z., (1990). Asteroid Families. I. Identification by Hierarchical Clustering and Reliability Assessment. *The Astronomical Journal, 100*, pp. 2030-2046.

Zappalà, V., Bendjoya, Ph., Cellino, A., Farinella, P., & Froeschlé, C. (1995). Asteroid Families: Search of a 12,487-Asteroid sample Using Two Different Clustering Techniques. *Icarus, 116*, pp. 291-314.

Zappalà, V., & Paolicchi, P. (2002). Physical and Dynamical Properties of Asteroid Families. In *Asteroids III* (W.F. Bottke Jr et al., eds.), pp. 619-631. Univ of Arizona, Tucson.

Zellner, B., Tholen, D.J., & Tedesco, R.F. (1985). The eight-color asteroid survey: Results for 589 minor planets. *Icarus*, *61*(3), pp. 355-416.